Growth and characterization of semiconductor quantum dots for optoelectronic device applications

By

SUMAN MUKHERJEE

Enrolment No- PHYS05201404008

Saha Institute of Nuclear Physics, Kolkata

A thesis submitted to the

Board of Studies in Physical Sciences

In partial fulfilment of requirements

for the Degree of

DOCTOR OF PHILOSOPHY

of

HOMI BHABHA NATIONAL INSTITUTE

February, 2020

Homi Bhabha National Institute[1]
Recommendations of the Viva Voce Committee

As members of the Viva Voce Committee, we certify that we have read the dissertation prepared by Suman Mukherjee entitled "Growth and characterization of semiconductor quantum dots for optoelectronic device applications" and recommend that it may be accepted as fulfilling the thesis requirement for the award of Degree of Doctor of Philosophy.

Chairman -Name & Signature with date

(Ex-Head, SPMS Division, SINP)

Prof. Satyaranjan Bhattacharyya. Email: satyar.bhattacharyya@saha.ac.in

Guide / Convener - Name & Signature with date

Prof. Satyaban Bhunia. Email: Satyaban.bhunia@saha.ac.in 14.07.2020

Co-guide - Name & Signature with date (if any)

Examiner - Name & Signature with date

Prof. Subhabrata Dhar. Email: dhar@phy.iitb.ac.in

Member 1- Name & Signature with date

Prof. Krishnakumar S. R. Menon. Email: krishna:menon@saha.ac.in

Member 2- Name & Signature with date

Prof. Chandan Mazumdar. Email: chandan.mazumdar@saha.ac.in

Member 3- Name & Signature with date

Dr. Prasanta Karmakar. Email: prasantak@vecc.gov.in

Final approval and acceptance of this thesis is contingent upon the candidate's submission of the final copies of the thesis to HBNI.

I/We hereby certify that I/we have read this thesis prepared under my/our direction and recommend that it may be accepted as fulfilling the thesis requirement.

Date: 14.07.2020

Place: Kolkata

Signature

Co-guide (if any)

Signature

Guide

[1]This page is to be included only for final submission after successful completion of viva voce.

Subject: Report of PhD Defence seminar of Mr. Suman Mukherjee
From: satya.bhattacharyya@saha.ac.in
Date: 28-Jul-20, 12:32 AM
To: satyaban.bhunia@saha.ac.in

To
Prof. Satyaban Bhunia
Saha Institute of Nuclear Physics, Kolkata

Dear Prof. Bhunia,

I was present in the PhD seminar talk entitled "Growth and characterisation of semiconductor nanostructures for optoelectronic device applications" delivered by Mr. Suman Mukherjee, one of your PhD students, held on 14th July, 2020 in the google meet where a large number of experts and students were present.

Mr. Suman Mukherjee explained the basic matters of his findings in a very lucid manner and his deliberation was very much informative.
He carried out extensive works on the semiconductor nanostructures and the amount of work is quite sufficient for a PhD thesis.

He was asked a number of questions by various experts, faculties and students present in the talk and he answered them quite satisfactorily.
I was very happy with his presentation and answers to the questions.

As the Chairperson of his doctoral committee, I saw his progress of work during his PhD tenure and I am fully aware of his scientific understanding and research output.

Considering his high standard of research works, publications and presentation, I strongly recommend the acceptance of PhD thesis for the award of PhD degree in favour of Mr. Suman Mukherjee.

With best regards,
Satyaranjan Bhattacharyya.

Dr. Satyaranjan Bhattacharyya
Senior Professor H
Surface Physics & Materials Science Division
Saha Institute of Nuclear Physics
1/AF Bidhan Nagar, Kolkata 700064, India
Tel: +91-33-23375345 (to -49) (Ext. 4217, 4610)
FAX: +91-33-23374637
email: satya.bhattacharyya@gmail.com

Subject: Re: Thesis recommendation and report
From: Subhabrata Dhar <subho_dh@yahoo.co.in>
Date: 24-Jul-20, 3:58 PM
To: Satyaban Bhunia <satyaban.bhunia@saha.ac.in>

Dear Prof. Bhunia,
In his Ph.D, Mr. Mukherjee has systematically carried out growth, structural and electronic properties of Ge nanocrystalline thinfilms and InAs monolayer quantum dots. He has used a variety of different experimental techniques to establish the findings on a solid footing. It was a great pleasure for me to review the thesis. During the viva-voce examination, Mr. Mukherjee could answer with confidence all the questions/comments raised by me and other reviewers of the thesis. He has also incorporated the suggested changes/corrections in the revised thesis, which I approve. The quality and quantity of the research work surely suffice the requirement for a Ph. D degree. I strongly recommend in favour of awarding the degree to Mr. Mukherjee.

Best regards
Subhabrata

############################
Subhabrata Dhar, Ph. D
Professor
Department of Physics
IIT Bombay, Powai
Mumbai - 400076
INDIA
Ph: +91-22-25767578 (Office)
Email: dhar@phy.iitb.ac.in
subho_dh@yahoo.co.in
subhodhar@iitb.ac.in
###########################

[illegible]

[illegible]

Sur[illegible]and Ma[illegible]r[illegible]S[illegible]n [illegible]D[illegible]n
Sa[illegible]n[illegible]u[illegible]u[illegible]ar[illegible]
[illegible]d[illegible]anna[illegible]ar
[illegible]a[illegible]
[illegible]n[illegible]n[illegible]

Subject: Report of Mr. Suman Mukherjee
From: "Dr. Krishnakumar S. R. Menon" <krishna.menon@saha.ac.in>
Date: 07-Aug-20, 2:24 PM
To: satyaban.bhunia@saha.ac.in

Dear Prof. Bhunia,

This is to inform you that I was personally present in the PhD seminar talk entitled "Growth and characterisation of semiconductor nanostructures for optoelectronic device applications" delivered by Mr Suman Mukherjee, held on 14th July 2020 in the google meet. He explained the basic Physics of his findings in a very lucid way and his talk was quite impressive. I think the amount of work, both in quality and quantity is quite sufficient for a PhD thesis. He was asked a number of questions and queries by experts, faculties and students and he answered all of them satisfactorily. I was very happy with his presentation and answers to the questions.

I have also seen his progress of work in the capacity of a member of his doctoral committee for the last few years and am well acquainted with his scientific exploration, understanding and research output. Considering all these aspects and his journal publications, I strongly recommend the acceptance of his PhD thesis for the award of PhD degree in his favour.

With best regards,

Krishnakumar Menon

****
Dr. Krishnakumar S. R. Menon
Professor-G,
Surface Physics & Material Science Division,
Saha Institute of Nuclear Physics,
1/AF, Bidhannagar,
Kolkata 700 064, INDIA.

Phone : +91 33 2337 5345-49 Ext. 3326
Fax : +91 33 2337 4637

e-mail: krishna.menon@saha.ac.in
****

Subject: Report on the PhD Defence seminar of Mr. Suman Mukherjee
From: chandan.mazumdar@saha.ac.in
Date: 29-Jul-20, 12:45 AM
To: "Satyaban Bhunia" <satyaban.bhunia@saha.ac.in>

To
Prof. Satyaban Bhunia
Surface Physics and Material Science Division
Saha Institute of Nuclear Physics, Kolkata 700064

Dear Prof. Bhunia,
Below, please find my report on the PhD Defence seminar of Mr. Suman Mukherjee

---

Mr. Suman Mukherjee has presented his Ph.D thesis talk on the "Growth and characterisation of semiconductor nanostructures for optoelectronic device applications" on 14th July, 2020. During the talk, he has described the goal of his work, and proceeded further on the contribution he has made during his Ph.D period. His presentation was quite flawless and the volume as well as the quality of the work itself is worthy of a Ph.D thesis. After the talk, he was asked a wide range of questions by various members of the audience and he could answer all the questions at ease. As a member of the doctoral committee, who has witnessed his gradual progress over the last four or five years, I am aware the significance of his work and strongly recommend for the award of the Ph.D degree to Mr. Suman Mukherjee.

With best regards
Chandan Mazumdar

Professor, Condensed Matter Physics Division
Saha Institute of Nuclear Physics, Kolkata 700064

Subject: PhD viva-voce report of Mr. Suman Mukherjee
From: Prasanta Karmakar <prasantak@vecc.gov.in>
Date: 30-Jul-20, 9:11 AM
To: "Satyaban Bhunia" <satyaban.bhunia@saha.ac.in>

Dear Prof. Bhunia,

Please find below the PhD viva-voce report of Mr. Suman Mukherjee:

I was present as an examiner in the online viva -voce examination of Mr. Suman Mukherjee, held on 14th July, 2020. He presented his thesis "Growth and characterization of semiconductor nanostructures for optoelectronic device applications".

He has developed the nano-crystalline Ge thin film and InAs quantum dot structures by cluster ion and sub monolayer deposition, respectively. He has studied the structural and optical properties of the grown nano structures. His developmental and characterization works are extensive and informative. He also has shown the potential applications of the developed InAs nano dots for optoelectronic devices. The amount and quality of his work is sufficient for a PhD thesis.

He started his presentation from very basic understanding of quantum structures and nicely presented his own observations. He was asked a number of questions by experts and students. He successfully answered all the questions. As a viva voce examiner, I was satisfied by his presentation and the answers to my queries.

Considering the high quality research works, publications and very good presentation, I strongly recommend the acceptance of thesis for the award of PhD degree in favour of Mr. Suman Mukherjee.

Prasanta Karmakar

STATEMENT BY AUTHOR

This dissertation has been submitted in partial fulfilment of requirements for an advanced degree at Homi Bhabha National Institute (HBNI) and is deposited in the Library to be made available to borrowers under rules of the HBNI.

Brief quotations from this dissertation are allowable without special permission, provided that accurate acknowledgement of source is made. Requests for permission for extended quotation from or reproduction of this manuscript in whole or in part may be granted by the Competent Authority of HBNI when in his or her judgment the proposed use of the material is in the interests of scholarship. In all other instances, however, permission must be obtained from the author.

SUMAN MUKHERJEE

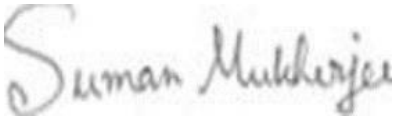

Name & Signature of the student

DECLARATION

I, hereby declare that the investigation presented in the thesis has been carried out by me. The work is original and has not been submitted earlier as a whole or in part for a degree / diploma at this or any other Institution / University.

SUMAN MUKHERJEE

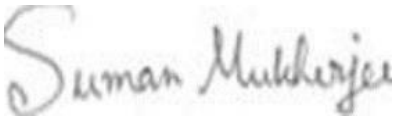

Name & Signature of the student

List of Publications arising from the thesis

Journal

1. “Phase selective growth of Ge nanocrystalline films by ionized cluster beam deposition technique and photo-oxidation study”, S. Mukherjee, A. Pradhan, T. Maitra, S. Mukherjee, A. Nayak, and S. Bhunia, *Advanced Materials Letters* **8** (2017) 891-896.

2. “Tuning of near Infrared Excitonic Emission from InAs Quantum Dots by Controlling the Sub-monolayer Coverage”, S. Mukherjee, A. Pradhan, S. Mukherjee, T. Maitra, S. Sengupta, B Satpati, S Chakrabarti, A. Nayak, and S. Bhunia, *Journal of Luminescence* **210** (2019) 311-321.

3. “Carrier escape mechanism in laterally correlated InAs sub-monolayer quantum dots using temperature dependent photoluminescence”, S. Mukherjee, A. Pradhan, T. Maitra, S. Mukherjee, S. Sengupta, S. Chakrabarti, A. Nayak, S. Bhunia, *Journal of Luminescence* **215** (2019) 116597.

4. “Carrier transport and recombination dynamics of InAs/GaAs sub-monolayer quantum dot based near infrared photodetector”, S. Mukherjee**,** S. Mukherjee, T. Maitra, A. Pradhan, S. Sengupta, S. Chakrabarti, A. Nayak, S. Bhunia, *J. Phys. D: Appl. Phys*. **52** (2019) 505107.

Chapters in books and lectures notes

1.

2.

Conferences

1. “Growth and characterization of cubic and non-cubic Ge nanocrystals”. S. Mukherjee, A. Pradhan, T. Maitra, S. Mukherjee, A. Nayak, and S. Bhunia, *AIP Conf. Proc.* **1728** (2016) 020111.
2. “Growth and characterization of InAs sub-monolayer quantum dots with varying fractional coverage”, S. Mukherjee, A. Pradhan, S. Mukherjee, T. Maitra, S. Sengupta, S. Chakrabarti, A. Nayak, and S. Bhunia, *AIP Conf. Proc.* **1942** (2018) 080039.

Others

SUMAN MUKHERJEE

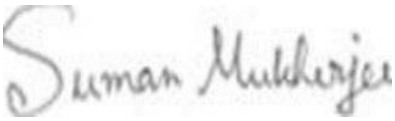

Name & Signature of the student

DEDICATIONS

To my family and friends

ACKNOWLEDGEMENTS

It’s an honor for me to express my gratitude to the persons, who have enriched me throughout the last five years with their priceless company and invaluable support.

Firstly, I would like to express my sincerest gratitude to my supervisor Prof. Satyaban Bhunia for his continuous support throughout my Ph.D. tenure and related research. I would also like to acknowledge Prof. Subhananda Chakrabarti and Prof. Arabinda Nayak for their active contributions in the collaborative research work and consistent support. I am especially thankful to Mr. Debiprasad Panda for sharing his expertise in MBE growth. I am thankful to all of the members of my doctoral committee Prof. Satyaranjan Bhattacharyya, Prof. K. S. R. Menon, Prof. Chandan Mazumdar, and Prof. Prasanta Karmakar for their support during this tenure. I would like to acknowledge Prof. M. K. Mukhopadhyay, Arkabikash De, Arnab Singh, and Dr. Arpan Bhattacharya regarding their contributions related to X-ray scattering, and Dr. Biswarup Satpati for TEM measurements.

I would like to acknowledge my wife Anindita and family members for their constant support and encouragement. I would also like to thank my lab-mates Anway, Sukhendu and Tamaghna, for their timeless company. I am heartily thankful to Arghya, Gourab, Bankim, and Mantu for their revered and amicable company at SINP. I am especially thankful to Mr. Mukul Chndra Das for his valuable support on official issues that I had to cope up with. To end with, I acknowledge the staffs of MSA-2, especially Bishu, Shaymal da, Haran dadu and Sanjib da.

Contents

List of figures

Fig.6.4 *PL spectra (dotted lines) of SML QDs for different InAs SML coverage (0.4-0.8 ML) and reference SK QD sample at different temperature (5-285 K). The solid lines are the respective fits by using standard LSF model carrier rate equation with reduced* χ^2 *~ (2x10*$^{-3}$*-6x10*$^{-3}$*). The reference SK-QD sample exhibits an additional broadened PL peak at ~1.38 eV related to QD wetting layer electronic transition which is absent in PL spectra of SML-QDs.*

Fig.6.5 *Temperature variation of TDPL extracted (a) inter-dot carrier tunnel time* τ_t *and (b) carrier radiative recombination time* τ_r *and for different SML coverage (0.4-0.8 ML) along with the reference SK QD sample. Both the characteristic lifetime has been found to be fairly constant with temperature with a standard deviation of 1.3-3.2 % and 1-3.9 % relative to their respective mean values.*

Fig.6.6 *Variation of temperature averaged* Γ_t, Γ_r *and* Γ_r / Γ_t *with InAs SML coverage (0.4-0.8 ML) along with reference SK QD grown with threshold coverage of 1.7 ML. Evidently,* Γ_r *and* Γ_t *have exhibited increasing and decreasing trend with increasing SML coverage whereas their ratio* Γ_r/Γ_t *undergoes gradual enhancement.*

Fig.6.7 *Variation of TDPL extracted carrier tunnel time* Γ_t *and theoretically calculated inter-dot carrier tunnel time* Γ_t^{WKB} *with average inter-dot lateral separation* $<L_B>$ *related to different InAs SML coverage. Close agreement of their respective values justifies the co-relation between PL extracted fitting parameter* Γ_t *and average inter-dot separation* L_B *extracted from GISAXS measurements.*

Fig.6.8 *A schematic representing the relative measure of different average inter-dot in-plane separation* L_B *and carrier tunneling time* Γ_t *as a function of InAs SML coverage. With increasing SML coverage, decreasing the degree of e-h wavefunction (green and black) overlap in QD ground state and a smaller value of* L_B *(*$L_{B2} < L_{B1}$*) is associated with a faster rate of inter-dot carrier tunneling (*$\Gamma_{t2} < \Gamma_{t1}$*).*

Fig.7.13 *Variation of measured detectivity at f=400 Hz with (a) applied reverse bias and (b) temperature for different coverage fraction including the reference SK QD sample.*

List of tables

Chapter 8

Conclusion and future aspects

8.1 Conclusion

The objective of this thesis is the study of the structural and optical properties of quasi zero-dimensional semiconductor structures and investigate the feasibility of their implementation in light-emitting and photodetector devices. The whole thesis work is shaped into two major parts, i.e., growth and characterization of elemental Gr IV Ge nanocrystal and self-assembled sub-monolayer quantum dot of III-V compound of InAs/GaAs. The study includes investigation of optoelectronic properties of the low-dimensional structures as a function of adatom kinetics and effective layer coverage of growth which has been systematically correlated with active lattice strain and structural information.

Ge exists in two phases, namely simple cubic, and tetragonal (ST-12) structure. But in nature, Ge is mainly found in a normal cubic phase which has a very small indirect bandgap. On the other hand, the rare metastable tetragonal Ge phase has a direct bandgap of much higher energy which is more demanding for high gain light-emitting applications. But this novel phase can only be realized if the Ge crystallites are grown in sufficiently small size. As part of this thesis work, we have worked towards developing an ionized cluster beam deposition technique to grow this tetragonal phase in a substantial amount while suppressing the growth of the normal cubic phase through the formation of Ge nanocrystals. We have categorically shown a selective yield of co-existing cubic and tetragonal phases by controlling the kinetic energy of the beam of cooled Ge clusters in the deposition chamber. Through adequate structural and optical analysis, it has been observed that the relative abundance of the tetragonal phase can be significantly enhanced by decreasing the kinetic energy of the bombarding cluster beam. The film grown by using neutral Ge clusters corresponding to the lowest kinetic energy shows the highest relative yield of the tetragonal phase for a nanocrystallite size of 7 nm. The nanocrystallite size was found to decrease monotonically from 15 nm to 7 nm with decreasing beam acceleration potential from 2.5 kV to 0 kV. While decreasing the beam energy, below a

certain threshold value of NC's size, the normal cubical phase transforms itself into a more compressed high energy metastable tetragonal (ST-12) phase. The appearance of a broadened redshifted TO-like phonon peak at 275 cm^{-1} in the Raman spectra confirms the growth of Ge nanocrystallites. The monotonic redshift in phonon energy corresponding to the broadened Raman peak with decreasing cluster beam energy (2.5 KV-0 KV) suggests progressively stronger confinement-induced phonon interaction with grain boundaries inside Ge nano-crystallites. This is an indication of the emergence of another Ge phase coexisting with a normal diamond-like structure with a comparatively smaller crystallite size.

The results show the feasibility of tuning the emission energy and efficiency of visible photoluminescence (1.55-1.75 eV) at room temperature (RT) to high values by selectively increasing the relative proportion of tetragonal Ge phase by controlling the beam energy. This offers potentiality of Ge-NCs enriched in the tetragonal phase for RT visible light-emitting applications. We have further studied the provision for controlled photo-oxidation of the tetragonal rich Ge thin films. In this way, it has been possible to further tune the luminescence to green color (~550 nm) while decreasing the effective size of the NC cores under oxide (GeO_x) cover.

The next part of this work is molecular beam epitaxial growth of self-assembled InAs sub-monolayer quantum dots in GaAs matrix and their strain, structural and optical characterization. Photodetector application of these SML QDs has also been studied in detail. We have demonstrated the feasibility of spectral tuning of their excitonic photoemission in the near-IR region (1.4-1.5 eV) by controlling the InAs sub-monolayer coverage from 0.8 to 0.4 ML. Through systematic high-resolution x-ray diffraction, Raman scattering and low-temperature photoluminescence measurements, we have explicitly investigated the effect on spectral properties with varying InAs coverage, as a consequence of the different degree of strain and quantum size effect. The average QD heights for different InAs coverage are

extracted from the fitting of the associated Raman spectra by the Phonon confinement model (PCM). The average QD height reduces from 2.3 nm to 1.4 nm as the coverage is decreased from 0.8 ML to 0.4 ML. The x-ray diffraction measurement shows enhancement of in-plane compressive strain from 1.9 x 10^{-2} to 3.1 x 10^{-2} as a result of the reduction in SML coverage (0.8-0.4 ML). It also has been observed that the built-in compressive surface stress due to lattice misfit between InAs and GaAs, increasing from 54.5x10^{8} Pascal to 178x10^{8} Pascal with decreasing InAs sub-monolayer coverage (0.8 ML-0.4 ML) has controlled the quantum dot growth and played a leading role to determine their density and homogeneity in size distribution. The reduction of layer coverage from 0.8 ML to 0.4 ML causes a reduction in the dot density by almost one order of magnitude from 9x10^{10} cm^{-2} to 2x10^{10} cm^{-2}. The variation of InAs coverage fraction also significantly affects the in-plane spatial arrangement of the embedded SML-QDs. The grazing incidence SAXS measurement along different azimuthal directions shows that with decreasing InAs coverage, the average separation between the embedded QDs as well as the correlation length of the laterally coupled QDs seems to increase. The spectral blueshift from 1.4 eV to 1.5 eV with decreasing InAs coverage from 0.8 ML to 0.4 ML is attributed to the increasing degree of carrier confinement due to a stronger quantum size effect. The reduction of sub-monolayer coverage from 0.8 ML to 0.4 ML has also led to enhancement in exciton binding energy from 4.4 meV to 11.4 meV, which has caused stronger localization to the dissociated photo-carriers at lower InAs coverage. With increasing InAs coverage, the decreasing value of excitonic binding energy and average inter-dot separation (in-plane) initiate enhanced carrier wave function overlap and opens up easy pathways for escape in the form of inter-dot carrier tunneling.

We have further studied the dynamics of photo-generated carriers in correlated self-assembly of embedded InAs/GaAs sub-monolayer quantum dots from the temperature-dependent PL (TDPL) measurements as a function of InAs fractional coverage. It was found that the mutual

competition of excitonic recombination and quantum mechanical photo-carrier tunneling through the carrier states of the electronically coupled system seems to determine the shape and intensity of the TDPL spectra. The lifetimes related to different carrier relaxation channels have been deduced through fitting the respective TDPL spectra by dynamical carrier rate equation following the Localized state functional model. The excitonic recombination lifetimes are found to be 172 ps, 242 ps, 453 ps, and 1125 ps whereas the tunnel times are measured to be 1008 ps, 828 ps, 437 ps and 350 ps for 0.4, 0.6, 0.7 and, 0.8 ML coverage respectively. Evidently, the recombination lifetime increases whereas the tunneling lifetime decreases with increasing SML coverage. More importantly, with increasing SML coverage (0.4-0.8 ML) the ratio of characteristic lifetimes (Γ_r/Γ_t) of recombination and inter-dot tunneling has been found to progressively increase from 0.17 to 3.3 which has been found to hold the key to determine the temperature-dependent spectral properties as a function of InAs sub-monolayer coverage. The extracted Γ_r/Γ_t ratio (~0.17 and 0.3) of less than unity at lower SML coverage (0.4-0.6 ML) suggests that the confined carriers tend to recombine faster in respective QD ground states before transferring into the well-separated neighboring QDs. This gives rise to faster quenching of PL signal with increasing temperature at lower SML coverage (0.4-0.6 ML). On the other hand, at higher SML coverage (0.7-0.8 ML), the value of Γ_r/Γ_t (~1.1 and 3.3) greater than unity suggests that the probability of exciton recombination before carrier escape via inter-dot tunneling decreases monotonically which effectively consequences to extended carrier lifetime. This is attributed to the simultaneous reduction in the probability of recombination of less confined exciton system and provision of faster tunneling of comparatively loosely bound dissociated carriers through narrower intermediate GaAs barrier. This has offered substantial luminescence efficiency up to elevated temperature, greater temperature stability to the peak emission energy and more interestingly a decreasing trend of spectral linewidth with temperature (5-150 K) for higher SML coverage. Activation of non-dissipative photocarrier

escape with effectively enhanced carrier lifetime for higher SML coverage consequently gives rise to subsequently enhanced PL efficiency which sustains up to nearly room temperature (~285 K). This is manifested by progressively increasing the value of extracted thermal activation energy with increasing SML coverage. At higher coverage (0.7-0.8 ML), the anomalous reduction in PL linewidth with increasing temperature in the range of 5 K to 150 K is attributed to energy selective tunnel-assisted carrier transfer and preferential carrier population in some locally minimum QD ground states. On the other hand, at lower SML coverage (0.4-0.6 ML) more localized photocarriers in QD states undergo regular spectral broadening due to predominant temperature-induced carrier-phonon scattering. Moreover, the absence of any photocarrier loss into the wetting layer in SML-QD and observed tunnel-assisted fast photo-carrier transport with tunnel time as low as 350 ps has the potential to expedite the response speed of optoelectronic switching devices. In comparison to tunnel time of 1328 ps for conventional InAs/GaAs SK QDs, a four times faster inter-dot tunneling is observed in InAs/GaAs SML-QD system. Temperature independent carrier recombination and inter-dot transfer of photogenerated electrons in SML QDs offer more thermal stability than conventional SK QD which makes it more demanding for high-temperature optoelectronic applications.

The different degrees of photocarrier escape and energy relaxation in the coupled array of InAs/GaAs sub-monolayer quantum dots as a function of QD spatial correlation offers a further provision of engineering charge transport properties by controlling InAs coverage fraction. With this motivation, the feasibility of simultaneously tuning the dark current, external quantum efficiency and speed of photo-response of QDIP by controlling InAs sub-monolayer coverage has been investigated. A quantitative investigation of radiative recombination and carrier escape from QD confined states has been performed to get a physical insight of tuning of physical response parameters of InAs/GaAs SML-QDIP. The observations have led to the

conclusion that variation of the SML coverage provides a means for controlling the relative time scales of the inter-band recombination and carrier tunneling that can essentially govern the overall detector performance also. The quantum efficiency of photo-response of the SML-QD based photodetector has been found to be governed by the ratio of characteristic lifetimes of excitonic recombination and inter-dot tunneling escape. The ratio of lifetimes, as extracted from the steady-state charge transport simulation has exhibited an increasing trend with increasing SML coverage. This is in good agreement with the results deduced from the dynamical carrier relaxation simulation of temperature-dependent PL.

The photo-response related to inter-band absorption has undergone consistent spectral redshift with increasing SML coverage in the NIR region due to a reduction in inter-band transition energy. The measured photoresponsivity has exhibited a progressive rise with increasing SML coverage at a low temperature (≤100 K) limit. The peak responsivity measured at 80 K under -2 V applied bias has been found to increase by almost ten times as the sub-monolayer coverage is increased from 0.4 ML to 0.8 ML. This can be characteristically described on the basis of the combined effect of increasing photocarrier dissociation efficiency and the probability of its subsequent extraction through the QD confinement states into active conduction channels. With increasing coverage, increasing photo-dissociation efficiency and activation of inter-dot tunneling faster than excitonic recombination ($\Gamma_r > \Gamma_t$) has led to higher photoconductive gain and consequently promotes extraction of more free charge carriers into the electrodes through high conductivity channel. The external quantum efficiency (EQE) for 0.4, 0.6, 0.7 and, 0.8 ML coverage are measured to be 4.1%, 9.7%, 17.3% and 23.8% respectively. The enhanced EQE is attributed to increasing photoconductive gain and carrier dissociation efficiency with increasing SML coverage. The progressively increasing charge carrier collection efficiency with increasing InAs SML coverage leads to enhancement in peak responsivity. The recorded peak responsivities are 1.9 mA/W, 5 mA/W, 7.8 mA/W and 9.5 mA/W for 0.4 ML, 0.6 ML,

0.7 ML and 0.8 ML coverage. The measurements show that in comparison to reference InAs/GaAs SK QD photodetector, the responsivity of 0.8 ML QD photodetector measured under similar conditions has increased by twenty times. The inter-dot carrier tunneling with lower characteristic lifetime also offers efficient transport of dissociated free photocarriers through the detector's active medium which consequences to shorter response time. From transient photo-response of the QD photodetector, the response time has been measured to be 366 μs, 253 μs, 182 μs, 100 μs for 0.4 ML, 0.6 ML, 0.7 ML, and 0.8 ML coverage. The relatively shorter detector response time at higher sub-monolayer coverage pushes up the operational switching frequency from ~ 600 Hz to 1.3 kHz. This offers a more robust temporal response up to higher operational frequency (few kHz) in response to an external switching photo-signal. At the same time, with increasing coverage, the increasing degree of trapping of injected carriers in the confined states of the quantum dot has led to a greater reduction of dark current. Higher thermal activation energy representing the potential offset between QD and barrier layer reduces the thermionic emission of the trapped injected carriers from the QD bound state. This essentially attributes to the reduction of dark current. The dark current at near room temperature (~250K) under -2V applied bias is recorded to decrease by ten times from $5x10^{-4}$ A to $6x10^{-5}$ A as the coverage is increased from 0.4 ML for 0.8 ML. This has helped to significantly improve the detector's high-temperature performance and pushed up the operating temperature for potential photodetection up to 250K with measured detectivity as high as ~$8x10^{11}$ $cmHz^{1/2}W^{-1}$. The peak specific detectivity increases by twenty-eight times from 1.5 $x10^{11}$ to 42 $x10^{11}$ as the coverage is increased from 0.4 ML to 0.8 ML. Notably, two orders of magnitude lower dark current have been recorded for SML-QDs, as compared to the measured dark current of ~10^{-4} A for reference SK-QD sample under the condition of V_B = -2 V and T=250 K. This is a consequence of stronger confinement induced dark carrier trapping with a greater number of QD trap centres as compared to SK-QD based photodetector.

From a device performance standpoint, in spite of inherent tradeoff, we have shown the feasibility of tuning both the detector response speed and detectivity to significantly higher values by controlling InAs sub-monolayer coverage. This is attributed to the two-fold effect of laterally coupled SML QDs offering enhanced quantum dot carrier trapping leading to reduced dark current and increased photocurrent promoted by tunnel assisted faster free carrier transport.

8.2 Possible extension of this work and future outlook

Some possible extension and future aspects of the thesis work are as follows

8.2.1 Study photo-carrier dynamics in coupled QD system under transverse E-field

We have studied photocarrier dynamics and the consequences on TDPL and electro-transport properties of InAs/GaAs SML-QDs as a function of InAs sub-monolayer coverage without the presence of any transverse electric field. This work can be generalized to theoretical modelling of investigating photo-carrier relaxation dynamics in SML-QDs and other assemblies of strongly coupled nanostructures in the presence of a transverse electric field. Presently, I am working on developing a theoretical model to explicitly study field-dependent optoelectronic properties under strong carrier localization.

8.2.2 Enhanced carrier lifetime by introducing SML-QD superlattice minibands in IBSC

In my thesis, we have worked towards controlling the relative rate of tunneling to carrier recombination to tune light emission and photodetector response properties by varying SML coverage. The same methodology can be exploited to tune the product of open-circuit voltage (V_{oc}) and short circuit current (I_{sc}) in SML-QD based intermediate bandgap solar cell (IBSC). Strongly coupled SML QD superlattice can serve the role of a highly efficient intermediate

miniband in intermediate bandgap solar cell (IBSC). The spatial separation of electron-hole pair due to the internal electric field in solar cells enhances the carrier lifetime which is the key to improve the inter-subband transition strength and consequently to increase the two-step photocurrent (I_{sc}). But this has an inherent trade-off with V_{oc} which decreases with enhanced carrier lifetime. SML-QD can come handy in this situation which provides extended carrier recombination lifetime due to stronger quantum confinement, as well as promotes tunnel induced photo-carrier transport that can compensate V_{oc} and thus maintains high power efficiency.

8.2.3 Mid-infrared photonics in SML-QD quantum cascade and (DWELL) structure

InAs/GaAs SML-QDs can be integrated into the quantum cascade and a dot-in-well (DWELL) structure which can serve as a novel active material for mid-infrared photodetector. These devices enjoy the advantage of zero-bias operation, lower dark current, high operating temperature and small power dissipation which has attracted immense interest for possible applications in “lab on a chip” technologies for chemical sensing and free-space communication. Now, for better performance of such devices, the strength of inter-subband transition needs to be high which may be feasible by trapping the carriers for long by inducing some trap states. In that sense, the recombination dynamics and carrier lifetime measurements can be a good probe where my expertise on theoretical modelling of photo-carrier dynamics may be suitable.

8.2.4 Controlling photo-carrier relaxation dynamics in 2-D material

The idea of tuning relative lifetime of carrier recombination to tunneling in electronically coupled self-assembly of QDs can be employed to describe the photocarrier dynamics in advanced two-dimensional optoelectronic materials, like graphene and newly introduced

transition metal dichalcogenides (TMDs), like MoS_2 and WSe_2. By systematically following the relative strength of excitonic recombination and carrier escape, it may possible to tune the EQE, the stability and quality of the corresponding photo conversion devices through variation of feasible physical parameters.

8.2.5 Type-II SML-QD structure for photovoltaic application

There is an increasing interest in type-II structures like colloidal ZnTe/ZnSe QDs, due to their unique tuneable optoelectronic properties with band alignment with large band offset and improved quantum confinement effects. Recently, a slightly modified system made out of type-II ZnCdTe/ZnCdSe sub-monolayer QDs has emerged as one of the best candidates for efficient intermediate band solar cells due to its high carrier lifetime. I have a future interest in solar cell design by employing the strain compensated SML-QDs and analyze the combined photo-transport and gain dynamics which is still very much open to being explored. From theoretical interest, the investigation of the Aharanov–Bohm effect can be feasible by controlling the degree of carrier localization inside the QDs.

Summary

The objective of this thesis is to study the structural and optical properties of phase-selectively grown Ge nanocrystal (NC) and InAs/GaAs sub-monolayer quantum (SML-QD) dot 0-D semiconductor structures and to investigate the feasibility of spectrally tuning their light-emission and electro-optic properties.

Through formation of Ge-NC, we have categorically shown a selective yield of cubic and metastable tetragonal ST-12 phases of Ge which could be tuned by controlling the kinetic energy of the beam of ionized clusters in an ion cluster beam deposition chamber. It has been observed that with decreasing the beam accelerating potential (2.5-0 kV), a greater number of normal cubic crystallites transform into the compressed ST-12 phase along with a reduction in Ge nanocrystallite size (15-7 nm). The consequent variation in the quantum-size effect and relative abundance of the Ge phases have offered the feasibility of tuning the luminescence in the visible region (1.55-1.75 eV) at room temperature (RT). In the next part, we have demonstrated the feasibility of spectrally tuning the excitonic luminescence from MBE-grown GaAs-hosted self-assembled InAs SML-QD in the near-IR region (1.4-1.5 eV) by controlling the InAs SML coverage from 0.8 to 0.4 monolayer (ML). The blueshift in PL-peak energy is due to the increasing degree of the quantum size effect with progressively reduced average QD height (2.3-1.4 nm) as measured from the Phonon confinement model simulation. The enhancement of in-plane compressive strain ($1.9x10^{-2}$ -$3.1x10^{-2}$) as a result of the reduction in SML coverage (0.8-0.4 ML) which leads to a reduction in QD density ($9x10^{10}$-$2x10^{10}$ cm^{-2}) and enhanced size homogeneity. The reduction in SML coverage also significantly increases both the average in-plane inter-dot separation and the correlation length the spatial distribution. Confinement induced enhancement in exciton binding energy (4.4 meV-11.4 meV) with the reduction in coverage leads to stronger localization to the photo-carriers. The variation of SML

coverage significantly controls the photo-carrier relaxation dynamics which essentially determine the temperature dependence of light emission and photodetector performance. It was found that the relative strength of the mutually competing excitonic recombination (Γ_r) and inter-dot tunnel (Γ_t) assisted carrier transport process, represented by the ratio of their characteristic lifetimes (Γ_r/Γ_t) basically hold the key to determine the temperature-dependent spectral properties as a function of InAs SML coverage. The related lifetimes have been deduced through fitting the respective TDPL spectra by a carrier rate equation following the Localized state functional model. The progressively increasing value of Γ_r/Γ_t from 0.17 to 3.3 with increasing coverage indicates that the photocarriers are becoming more probable to escape QD potential by tunnelling before they could recombine. This is attributed to simultaneous enhancement in excitonic recombination lifetime (172-1125 ps) and reduction in the tunnel time from 1008 ps to 350 ps with increasing the SML coverage (0.4-0.8 ML). This leads to extended photocarrier lifetime and enhanced population density of free carriers at higher SML coverage which offers substantial luminescence efficiency sustainable up to more elevated temperature (~285 K). On the other hand, at lower coverage (0.4-0.6 ML) the confinement-induced faster rate of excitonic recombination than carrier tunnelling (Γ_r/Γ_t <1) rapidly quenches the PL signal. At higher coverage (0.7-0.8 ML), we have observed an anomalous reduction in PL linewidth with increasing temperature (5-150 K) which can be described as a consequence of energy selective tunnel-assisted carrier transfer to some locally minimum QD ground states. We further have investigated the feasibility of simultaneously tuning the dark current, PC and response speed of QDIP by controlling InAs SML coverage. The increment in relative time scales Γ_r/Γ_t with increasing SML coverage seems to govern the rise in EQE from 4.1% to 23.8% and reduction in detector response time from 366 μs to 100 μs. With increasing coverage, the increasing degree of trapping of injected carriers in the QD confined states has led to a ten times reduction in dark current from $5x10^{-4}$ A to $6x10^{-5}$ A at near-RT (~250K).

Chapter 1

General introduction

1.1 Introduction

1.1.1 Introduction to quantum dot

The introduction of quantum dot semiconductor nanostructures has fuelled up the optoelectronic and photovoltaic industry with novel optical and electrical properties, distinctively different from the bulk material [1]. Relaxation of momentum selection rules of three-dimensionally constrained carriers inside the nanostructures, like semiconductor nanocrystal and self-assembled quantum dots, gives rise to intense and sharp radiative transitions [2]. In this sense, quantum dot can be physically described as a quasi-zero-dimensional (0-D) nanostructure. Its unique property of size-dependent carrier confinement effect makes it a source of pure excitonic emission with tuneable energy [3]. With a structural dimension smaller than the Bohr exciton radius, the excitonic (electron-hole pair) wave function becomes spatially localized within the length scale of Coulomb attraction. This gives rise to size-dependent fluorescence and sharp absorption spectral properties due to the delta function-like density of states (DOS). The exact energy of the discrete states depends on the strength of confinement, size, and shape of QDs, which can be controlled by varying the material growth parameters. Sometimes it is also called as “artificial atoms” because of atom-like tunable discrete states. These have enabled a wide range of QD based device applications such as light-emitting devices, photodetectors and efficient photovoltaics [4].

1.1.2 Phonon bottleneck and effective carrier lifetime in QDs

In the bulk material, the momentum space consists of continuously distributed k-points which offers many available states to the excited carriers for thermal relaxation to near-by states through phonon emission, as shown in Fig.1.1 (a). The carriers excited to higher energy states,

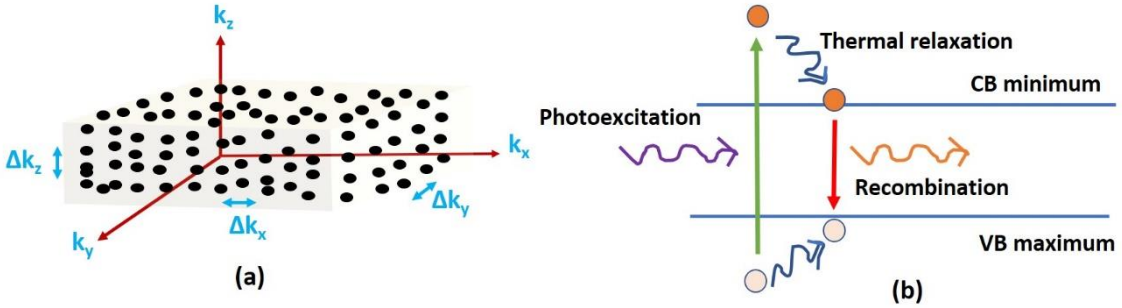

Fig.1.1 *(a) Continuous k-points in bulk material leads to faster thermal 'hot carrier' relaxation. (b) Phonon assisted carrier relaxation through the continuum of energy states in bulk material.*

called 'hot carriers' find easy pathways to thermally relax into the ground state through a continuum of energy states, as depicted in Fig.1.1 (b). Generally, this is a fast process with hot electron relaxation or cooling time of a few ps which decreases further with depletion in the carrier density in an excited state. The thermal relaxation of photoexcited hot carriers into the ground state decreases the carrier population in excited states which consequently leads to degradation of optical quantum efficiency of optoelectronic devices. In a zero-dimensional structure like QD, the motion of carriers is completely constrained in all three dimensions which discretize the k-points in momentum space, as shown in Fig.1.2 (a). The separation between k-points increases with decreasing the physical dimension of the nanostructure which reduces the density of k-points. This essentially suppresses most of the electronic transitions except some selective ones between the discrete energy states following certain selection rules, as depicted in Fig.1.2 (b).

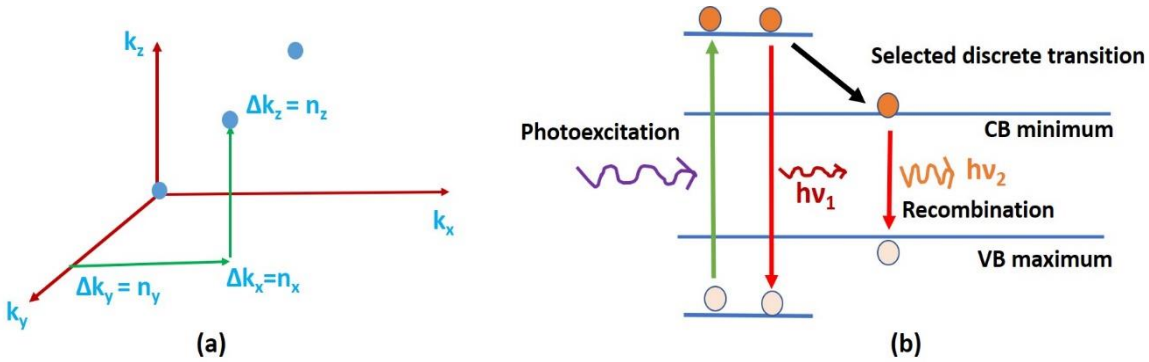

Fig.1.2 *(a) Discrete k-points, separated by some fixed distance in momentum space for QD structure slows down the thermal cooling. (b) Only the electronic transition between discrete states following certain selection rules.*

This significantly reduces the possibility of temperature-induced electron-phonon scattering and helps to preserve large carrier density in excited states. This results in enhancement of carrier lifetime in an excited state by the process, technically known as the Phonon-bottleneck effect. The emission of longitudinal optical (LO) phonon also becomes energetically forbidden in QDs, owing to the fact that the phonon energy (< 40 meV) at room temperature falls well within the intra-band energy spacing (> 50 meV) for practical QD sizes [5]. This promotes quantum dot structure as an active medium for high gain photodetector and efficient light-emitting devices operating at higher temperatures. The effective carrier lifetime is very critical for optoelectronic applications like photodetector or energy harvesting devices. If the carrier lifetime is short, the photogenerated carrier will relax to its ground state before being collected as photocurrent. This leads to a serious degradation of device efficiency. On the other hand, if the carrier lifetime is long enough the photocarriers are more likely to contribute to photocurrent before being recombined which helps to improve the device efficiency.

In addition to the long carrier lifetime in the QD excited states due to active phonon bottleneck effect, the decoupling of carriers from optical phonons also offers temperature-independent performance. This promotes quantum dots for efficient light-emitting device applications operating at higher temperatures. The suppression of temperature-induced phonon scattering in QDs offers a carrier relaxation time significantly longer than that of quantum wells (~1-10 ps) which are dominated by the emission of phonons.

1.1.3 Zero-dimensional semiconductor nanostructure

For three-dimensional carrier confinement, the structural dimension needs to be smaller than the electron de Broglie wavelength, so that the excitonic wave function could be completely localized inside the volume. This can only be attained in nanometer-size objects like nanocrystal or self-assembled quantum dots. Nanocrystals are grown by non-epitaxial

deposition of semiconductor materials whereas the self-assembled QDs are formed by heteroepitaxial deposition of semiconductor epilayers.

1.1.3.1 Semiconductor nanocrystal

Semiconductor nanocrystals (NC) are tiny crystalline nanometer size (1-100 nm) particle, dimensionally intermediate between large crystal and single small molecule. This simultaneously offers isolated atom-like confinement induced discrete radiative transitions and attractive structural and optical properties of crystalline materials [6-8]. Nanocrystals, with a size smaller than the excitonic radius, start to exhibit size-dependent sharp photoluminescence mediated by discrete electronic transitions that provide attractive optoelectronic features of tuning the emission energy over a large frequency range.

There has been a significant interest to grow nanocrystal of Gr-IV semiconductor materials like Si and Ge which are less toxic and environment-friendly. Still, now, Si is the most widely used semiconductor material for electronic device applications due to its abundance in nature. But in spite of that, the characteristic indirect gap of Si degrades the light emission and energy conversion performance. On the other hand, Ge with a larger excitonic radius than Si has the potential to offer quantum confinement effect at larger particle sizes. Ge exists in two phases, namely the cubic structure and metastable tetragonal ST-12 structure. Ge is mainly found in a normal cubic phase which has a diamond-like crystal structure with a lattice constant of 5.66 Å. The tetragonal ST-12 Ge structure is substantially elongated along the z-axis with lattice constant 9.346 Å as compared to the horizontal lattice constant of 5.292 Å [80]. The crystal structures of both the Ge phases are schematically shown in Fig.1.3 (a)-(b). Out of the two phases, only the tetragonal phase (ST-12) is demanding for high gain optoelectronic applications due to high direct bandgap. But this phase is very rare in nature. This novel tetragonal structure can only be realized if the grown Ge crystallites are sufficiently small in size. Ge enriched in tetragonal ST-12 phase, with a large direct bandgap of 1.47 eV [9-10]

makes it a better candidate for room temperature efficient light-emitting device applications in the visible-infrared range. The tetragonal Ge phase, as first reported by Saito et al in Ge nanoparticle of size less than 20 nm is relatively high in ground state energy than the normal cubic Ge phase [11]. Sato et al have reported that absorption band edge could be blue-shifted up to 2 eV by employing 4.3 nm size Ge-nanocrystal (NC) rich in the tetragonal phase. But above certain compressive stress, the excess strain energy is released while permanently transforming the cubical Ge phase to smaller crystallite size tetragonal phase which subsequently crystallizes in that form [12, 13]. Unfortunately, high yield growth of the tetragonal Ge phase is also limited by a certain degree of size dispersion of synthesized NCs. Therefore, it is still quite challenging to achieve a high proportion of tetragonal Ge phase over the cubic phase under three-dimensional spatial carrier confinement, both from optoelectronic device fabrication and physics point of view.

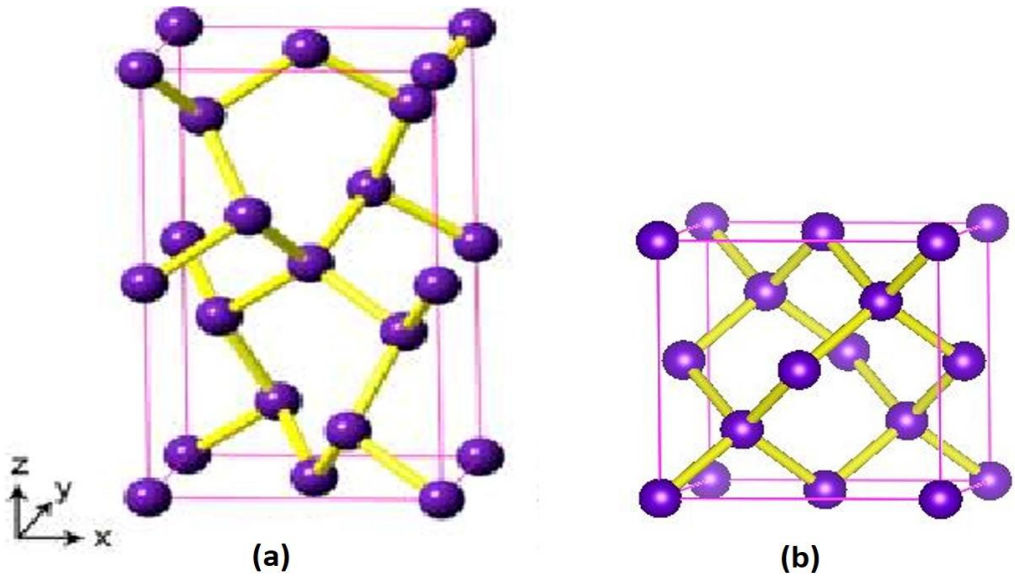

Fig.1.3 *Schematic representation of crystal structure of (a) tetragonal ST-12 and (b) diamond-like cubic Ge phase [80].*

1.1.3.2 Introduction to self-assembled sub-monolayer quantum dot

III-V semiconductor-based self-assembled quantum dots also started to flourish parallelly from late 1990 which has opened up new windows of the photonic industry thanks to the introduction of sophisticated epitaxial growth deposition techniques, like Molecular Beam Epitaxy (MBE)

or Metal Organic Vapor Phase Epitaxy (MOVPE) [14-16]. The buried quantum dots in a semiconductor environment potentially offers the provision of utilizing the novel optoelectronic properties for fabricating multi-stack heterostructure designed for particular device applications. The relaxation of excess lattice strain lattice mismatch between the consecutive heteroepitaxial layers gives rise to the formation of isolated self-assembled Stranski-Krasatanov (SK) quantum dots. InAs/GaAs quantum dot (QD) is one of such model systems of self-assembled formation with high lattice mismatch (~7%) between the grown InAs and GaAs epilayers. Through layer-by-layer heteroepitaxial deposition in MBE or MOVPE with atomic order precession (few Å) offers great control over the size uniformity of the grown embedded self-assembled quantum dots [17]. This semiconductor novel nanostructure acts as a source of pure excitonic emission spectrally tuned in the range from UV to IR with superior sensitivity to external parameters [18]. Heterostructure with vertically coupled stacks of buried self-assembled SK QDs, typically of 5-15 nm in diameter are usually employed in optoelectronic and intermediate bandgap solar cells to increase the optical gain and quantum yield [19].

Throughout the last two decades, many research groups have reported numerous techniques of growing self-assembled QDs, such as molecular beam epitaxy (MBE), metalorganic vapor phase epitaxy (MOVPE), chemical beam epitaxy (CBE) and liquid phase deposition (LPD) [20-24]. MBE technique serves better control of growth through a physical route with atomically pristine substrate kept in ultra-high vacuum (UHV) as compared to the MOVPE technique with a characteristically unavoidable residue of reactant gas over the substrate.

Most of the studies of self-organized QDs is relied on heteroepitaxial growth of lattice-mismatched material systems, like InAs/GaAs, In(Ga)As/GaAs and InAs/InP [25]. During the epitaxial growth of a multi-layered structure, each layer follows the lattice arrangement of the layer just below it. Therefore, in a heterostructure, while growing an epilayer of higher lattice

constant over a layer of comparatively lower lattice constant, the lattice structure of the above layer adjusts so as to follow the in-plane lattice constant of the layer below. As a consequence, a compressive strain is induced on the above layer. At first, a complete 2-D layer of QD material is formed over the substrate which is called the wetting layer. With further increase in the thickness of the above layer, strain starts to build up and above a certain critical thickness, the excess strain energy is partially relaxed by reducing the surface area through the formation of some embedded isolated 3-D islands, as represented by a schematic in Fig. 1.4. As an example, when the QD layer of InAs is grown above its critical thickness (~1.7 ML) over the crystalline GaAs substrate layer, the partial strain relaxation results in the formation of self-assembled InAs quantum dots. These islands are very small in all three dimensions and thus the motion of the carriers is constrained in all the directions inside the structures which essentially constitutes a zero-dimensional structure. But the formation of a 2-D wetting layer associated with the growth of self-assembled 3-D quantum dot leads to a significant reduction in carrier confinement and quantum efficiency. The consequent uncontrollable relaxation of strain can also lead to extended defect formation which greatly limits the provision of faithful device applications.

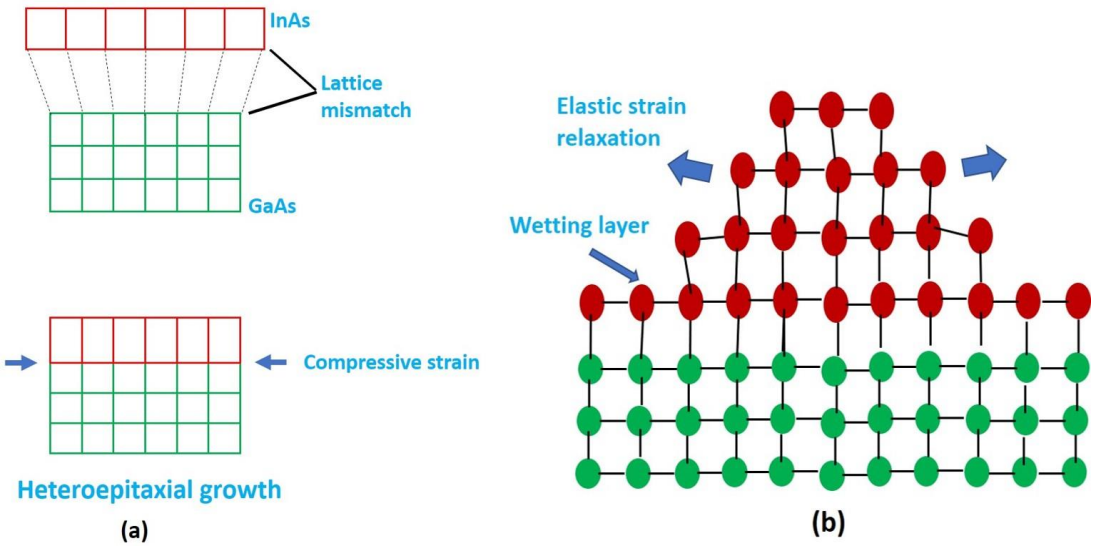

Fig. 1.4 *(a) Heteroepitaxial growth under compressive strain when $a_{layer}>a_{sub}$ (b) Formation of self-assembled quantum dot (example: InAs/GaAs QD) by relaxation of excess strain when the thickness of quantum dot layer exceeds the critical thickness.*

These limitations can be overcome with the introduction of sub-monolayer quantum dot (SML-QD), characteristically having higher dot density (~10^{10}-10^{11} cm^{-2}) and practically no wetting layer. SML-QD has emerged as a better alternative to conventional SK-QD with higher quantum gain and higher photoemission efficiency [26]. Sub-monolayer quantum dots are isolated flat islands, typically grown by depositing the QD material (InAs) in some lattice-mismatched barrier material (GaAs) in a very small amount with an effective coverage below one monolayer (ML). This is associated with stronger quantum confinement effect with enhanced exciton binding energy which offers better optoelectronic tunability than the conventional SK quantum dot for practical light emission and photodetector applications [26]. In the sub-monolayer growth mode of self-assembled QDs, the QD material is deliberately deposited in a lower amount than that required to form a complete 2D layer over the substrate. When substrate (like GaAs) layer and QD epitaxial layer (like InAs) with coverage below a monolayer are alternately stacked along the growth direction, patch-like QD islands (InAs) with a diameter of 6-8 nm are formed due to the effect of lattice strain between epitaxial layer and substrate. Followed by subsequent deposition of alternative layers, these islands become embedded in the multi-stacks and start to vertically correlate due to surface strain. The electronic wave functions of vertically spaced aligned 3D islands in the multi-stack have a strong degree of overlap which makes it characteristically equivalent to a quantum dot array. The correlation along the growth direction is one of the effective routes to produce an ordered array of QDs which possesses novel properties like low emission linewidth and better crystalline quality [27]. Under suitable choice of an epitaxy method, substrate materials, and growth condition, the vertical correlation among stacked QD layers can be greatly enhanced which leads to the growth of dislocation free crystalline heterostructure. This gives rise to stronger absorption of normal incidence of IR radiation which is quite handy for potential optoelectronic applications. The growth of SML-QD is practically devoid of any 2-D wetting

layer. This results in suppression of carrier relaxation into the wetting layer states and improved carrier confinement than that of SK-QD. The absence of the wetting layer in SML QD is also manifested by the absence of any wetting layer transition in PL spectra, as reported in InAs/GaAs sub-monolayer QD at low temperature. This is shown in Fig.1.5 [28]. In addition to this, less size inhomogeneity, and a higher number density promotes SML-QD for high gain optoelectronic applications with better spectral tunability than conventional SK-QD structure.

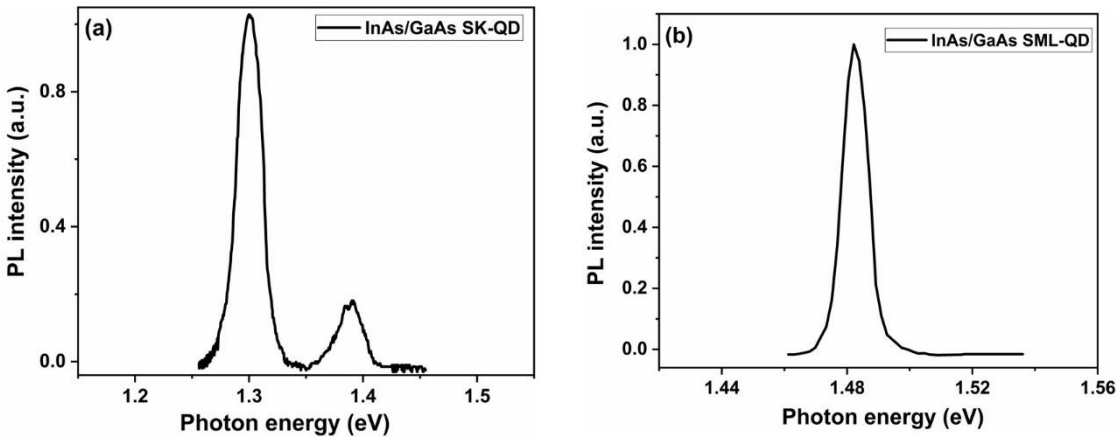

Fig.1.5 *Photoluminescence spectra of InAs/GaAs SK and SML quantum dot measured at 4 K [28].*

1.2 Motivation: State of the art

This section contains the fundamental aspects and state of the art applications of tetragonal Ge nanocrystal and sub-monolayer quantum dot along with their important macroscopic material properties, the timescales of photocarrier dynamics and their effects on optoelectronic properties.

1.2.1 Growth of tetragonal Ge phase

Unlike bulk structure, zero-dimensional nanostructure, with discrete energy levels provides superior wavelength tunability which was first realized in quantum structure semiconductor lasers by Dingle and Henry [29]. Reduction in threshold emission wavelength was first theoretically modelled by Asada et al and Arakawa et al [30-31]. A new window of optoelectronic and photovoltaic industry opened up for the first time when heavy metallic core

quantum dots were replaced by nanocrystals of non-toxic Gr-IV semiconducting material, like Si and Ge [32]. Germanium nanocrystals were actually introduced as ‘‘microcrystals” by Hayashi et al in 1982 [33]. But their size-dependent luminescence and absorption characteristics analysed through a series of measurements have established the fact that they are indeed nanocrystals (NC). Germanium-NC, with a much larger excitonic Bohr radius (~24.3 nm) than that of Si (~4.5 nm) is more superior for light emission applications than other Gr-IV semiconducting material, like Si, in spite of its abundance in nature. This helps to achieve substantial quantum confinement effect in Ge-NC for a relatively larger size than in Si [34]. Saito et al first reported the existence of the tetragonal ST-12 phase in Ge particles of size less than 20 nm which is more suitable for efficient optoelectronic applications as compared to the normal cubic diamond-like structure [34]. In the presence of high energy tetragonal Ge phase, the absorption band edge can be blue shifted up to 2 eV, as reported by Sato et al in NC of size 4.3 nm [35]. Kanemitsu et. al. reported that, below a certain threshold nanoparticle size of 4 nm, the normal diamond-like Ge phase can directly transform into the tetragonal structure by relaxing its surface energy [36]. The tetragonal Ge phase, exhibiting a direct transition of energy of ~1.47 eV can give visible photoluminescence (PL) at room temperature [37-38]. There have been many independent techniques to grow Ge-NCs, such as solution-based synthesis [39-40], chemical vapor deposition [41], laser ablation [42], magnetron sputtering [43], ion implantation [44] and cluster beam deposition [45], etc. But most of these deposition techniques give Ge NCs mainly enriched in normal cubic phase and very little yield in the tetragonal phase. The techniques are also limited in terms of tuning the PL peak energy over a broader spectral region by directly controlling the Ge crystallite size [46]. However, it is possible to achieve a greater abundance of novel Ge-tetragonal phase and suppression of the normal cubic phase in Ge-nano-crystalline thin-film employing ionized cluster beam deposition (ICB) technique [47-48]. Although this technique was first introduced by Takagi et

al to grow smooth metallic film with atomic order precession, this has been extended to grow semiconducting thin films on various substrates [49].

1.2.2 Epitaxial growth of self-assembled sub-monolayer quantum dot

All of the above non-epitaxial processes of growing 0-D nanostructures are limited due to a lack of precise controlling of quantum dot size, morphology and strain homogeneity. This puts a serious barrier to the production of high yield of quantum dot density, necessary for efficient energy conversion device applications. The introduction of self-assembled quantum dots (QD), originated from strain relaxed (partial) hetero-epitaxial layers opened up new pathways for highly efficient new generation photonic device applications, like QD-intermediate bandgap solar cell, QD-IR photodetector [50], single-photon QD lasers [51] and QD-double well detectors [52]. The inter sub-band absorption in the QDs has been employed to design photodetectors tuned in mid-infrared to the long-wave infrared region of the spectrum [53-54]. The recent advancement in growth and device design flexibility of self-assembled QDs have rendered a widespread application in high performance QD-based optoelectronic devices. This area is still open for further fundamental research on improving material properties and device designing. Epitaxy refers to the ordered deposition of layers of crystalline materials with one atomic lattice grown precisely atop another [□□]. In a semiconductor heterostructure, the spontaneous formation of alternative buried QD layers separated by multi-layers of higher bandgap materials gives rise to a different degree of inter-dot carrier coupling. The strength of coupling essentially determines the overall optical properties of the heterostructure which can be tuned by controlling the barrier thickness and suitably choosing the material of multi-layers. This provides huge flexibility in designing semiconductor heterostructure optoelectronic devices for versatile photonic applications [56]. Self-assembly of QDs was reported by growing highly strained epitaxial layers, like InAs on GaAs with a lattice mismatch of 7%. But it is also accompanied by the possibility of crystal dislocation after the growth of InAs by few

monolayers. This can seriously degrade the structural and optoelectronic properties of crystals. Fortunately, at fractional InAs coverage below 1 ML, small size (1-4 nm) InAs-rich islands or QDs have been introduced which have shown remarkable size homogeneity and very small strain fluctuation.

In sub-monolayer deposition, incorporation of a very small amount of dot material minimizes the possibility of carrier loss through wetting layer formation which offers better carrier confinement and greater optical gain than conventional SK QDs [57]. Ledentsov et al reported that the formation of InAs-rich defect-free QD clusters with higher aerial density (~10^{10}-10^{11} cm^{-2}) partially compensates the mismatch between GaAs (host) and InAs (QD) which suppresses the possibility of any incoherent strain relaxation. This offers a higher range of defect-free multi-stacking of heteroepitaxial layers with improved crystal quality as compared to SK-QD structures [17]. This can effectively enhance the strength of absorption of incident radiation and quantum gain of the QD based photovoltaics and photodetectors [18]. Strong carrier confinement associated with few monolayer high vertical dimensions can serve the provision of tuning the photoluminescence energy to visible-near IR (NIR) region, as was reported by Ting et al in InAs/GaAs SML-QDs [19]. Confinement-induced spatial localization of carriers can significantly enhance the excitonic binding energy and increase carrier lifetime to ten's of nanoseconds, as has been observed by Patwari et al in InGaAs/GaAs SML-QD based IR photodetector [26]. This makes SML-QDs potentially applicable as high gain inter sub-band photo-detectors.

1.2.3 Tuning of quantum dot light emission properties

For a wide range of optoelectronic and photovoltaic applications which fundamentally follows from the nature of charge carrier dynamics under different degree of spatial confinement, it is useful to tune the device performance by controlling growth parameters [58]. There are many reports of tuning photoemission and carrier transport properties by controlling deposition rate,

the number of multi stacks or through the incorporation of confinement enhancing (CE) barrier layers. There have been previous reports of tuning the photoemission energy of buried SML-QD based heterostructure by other physical means such as the incorporation of strain inducing layers and varying thickness of the spacer layer [58]. Krestnikov et al reported blueshift of QD photoemission energy by incorporating some confinement enhancing (CE) barriers of higher bandgap material [59]. The photoluminescence (PL) energy can also be tuned by varying the number of stacks of QD layers that govern the overall confinement potential of the heterostructure. J. Kim et al previously reported a method of tuning the PL peak energy in the range of 750-840 nm from InAs SML-QDs by varying the number of stacks (2-6) inserted between confinement enhancing higher bandgap AlGaAs barrier layer [20]. But most of these techniques are limited by specific material selection [22]. However, there is also one possible way to directly tune the luminescence energy solely by controlling the active amount of the dot material at the time of growth. In my thesis work, I have worked on tuning the optoelectronic and structural properties by controlling the amount of InAs in each epitaxial layer of the periodic structure by varying the InAs layer coverage below 1 ML.

According to previous reports, the growth of SML-QD of InAs in the host matrix of highly mismatched GaAs is naturally subjected to a certain degree of indium interdiffusion [59]. This leads to inhomogeneous strain and compositional modulation that can initiate the formation of some kind of additional $In_xGa_{1-x}As$ quantum well (QW) structure along with InAs-rich islands. Energy relaxation into these QW states degrades the QD excitonic luminescence. Formation of QWs and QDs structures are distinguished by different degree of lattice strain relaxation. The average strain plays an important role to determine the luminescence property. Increasing compressive strain leads to redshift in PL peak energy. Therefore, at different volumes of the dot material (InAs) in each layer, systematic monitoring of lattice strain relaxation is also an important aspect of improved light emission applications [60]. Strain also plays an important

role in carrier relaxation and transport process, as any undesirable defect center mediated by uncontrollable strain relaxation can reduce the carrier lifetime and degrade the efficiency of the optoelectronic devices at higher temperatures [61].

1.2.4 Localization induced carrier lifetime

The varying extent of confinement and inter dot carrier coupling with different InAs layer coverage may have a significant impact on the carrier localization and relaxation processes, as observed by Switaiski et al [12] in InAs/GaAs sub-monolayer stacks coupled to SK-QD. It is quite important to judge the potentiality of the SML-QDs to be used as efficient optoelectronic devices operating at room temperature [12]. Through temperature-dependent photoluminescence (TDPL) study of in-plane GaN/AlGaN multi-quantum wells, Wu et al reported a provision of controlling exciton localization by varying the degree of quantum confinement [62]. Similarly, by controlling the exciton binding energy inside a highly dense array of closely spaced SML-QDs, it may be possible to tune the inter dot carrier coupling. De-localization of excitons can offer easy pathways for carrier transport, demanding for fast speed optoelectronic applications. However, ultra-small dimensions of the SML-QD can offer confinement to both the excitons and thermal phonons which can strongly couple with each other and significantly affect the optoelectronic properties. So, it is also worth studying the qualitative features of phonons and the carriers confined within the SML-QD potential with varying InAs coverage which is important for efficient semiconductor QD light-emitting devices operating at high temperatures.

For high-performance optoelectronic device applications, the characteristic time related to carrier escape process from the QDs need to be very small to ensure fast response and higher carrier collection efficiency [63]. Usually, the effective carrier transfer in the QD ensemble depends on how many greater numbers of photo-generated carriers can escape QD confinement potential by quantum mechanical tunnelling before getting recombined. Unfortunately, due to

the presence of wetting layers in the SK QDs, dissociated electrons tend to recombine with the ground state holes before they could escape the QD confinement potential and reach the next QD [64]. Low carrier mobility, fluctuation of strain and energy barrier associated with the wetting layer causes a substantial delay and carrier loss in the net carrier transfer [65]. Many research groups have estimated carrier tunnel time to be 0.9-1.3 ns for 5-12 nm-sized InAs/GaAs SK QDs which is too slow for ultrafast device operation such as in the fast switching applications [65]. So, it is very useful to look for a correlated structure that can offer a direct dot to dot transport with higher carrier mobility and higher collection efficiency of photo-generated carriers. If SK QDs are replaced by correlated InAs sub-monolayer (SML) QDs, the time delay and carrier loss due to relaxation to wetting layer states can be highly reduced, as reported by Lam et al and Qiao et al [66]. They observed the feasibility of improving the time response and also the efficiency of the system by allowing direct carrier transfer among ground states of the nearby dots. There are many reports of increasing the rate of inter-dot tunnelling by increasing the spatial density of QDs or narrowing the width of the intermediate barrier layer. Fry et al reported two orders of magnitude enhancement of the strength of tunnelling with increasing the in-plane number density of InAs QD buried in the GaAs matrix by five times [67]. Tackeuchi et al reported one order of magnitude enhancement of the rate of quantum tunnelling by decreasing the thickness of an intermediate GaAs barrier layer vertically separating a two-QD system ($In_{0.15}Ga_{0.85}As$ and InAs) [68]. This is attributed to a higher degree of the partially penetrated inter-dot carrier wave functions overlap among closely-spaced QDs separated by narrow barriers. Therefore, an ensemble of SML QDs having areal number density (~10^{10}-10^{11} cm^{-2}), larger at least by one order of magnitude than that of SK QDs (~10^{9} cm^{-2}) can be instrumental to give rise to faster inter-dot tunneling than that reported for SK QDs [53].

The temperature dependence of QD photoluminescence and optical quantum yield is also affected by the process of radiative recombination of confined electron-hole pairs in the QD ground state. Typically, the recombination lifetime is found to be 500-2000 ps whereas carrier tunnel time is 10-60 ns for InAs/GaAs quantum dot at low temperature (4K) [13-14]. This leads faster carrier recombination before they could attribute to the conduction of free charge carriers. This degrades the external efficiency of QD-based photodetector and luminescence efficiency at high temperatures. For the improvement of the light emission and photo-current response properties, the two characteristic lifetimes need to be comparable with each other. Through theoretical DFT based calculations, Gobel et al reported enhancement of radiative recombination probability with decreasing QD dimension along the direction of quantum confinement, owing to the stronger overlap of the e-h wave function [69]. Then, achievement of a comparable rate of inter-dot tunnelling is readily feasible by exploiting an array of characteristically high-density closely-spaced coupled SML QDs.

1.2.5 Carrier dynamics in quantum dot infrared photodetector

Infrared quantum dot photodetector (QDIP) is one of the major applications of InAs/GaAs, InGaAs/GaAs or InAs/InP QD systems. Due to the advantage of three-dimensional carrier confinement, they are expected to serve potential high temperature (RT) photo-detection by reducing dark current [70]. The confinement induced active carrier-phonon bottleneck effect gives rise to a long excited-state lifetime of hundreds of picoseconds that can potentially increase the intrinsic photo-response [71]. However, low dot density, large size inhomogeneity and photocarrier loss into the inherent wetting layer in conventional SK-QDs lead to higher dark current and low quantum efficiency [72]. All these factors degrade the overall photodetector's (PD) performance. Sub-monolayer (SML) QD is one of the attractive alternatives to SK-QDs with several advantages. Stronger quantum confinement in absence of

any dissipative QD wetting layer, higher dot density and size uniformity inherent to SML QD, offers dark current-reduced improved sharper photo-response up to higher temperature.

Now, normal QD photodetector operation is based on either inter-band transition between two bound states in QD or inter sub-band transition between one bound and the delocalized continuum states. But for a high responsivity photodetector, usually, a long carrier lifespan against recombination is suited. In that sense, QDIP based on inter-band absorption with longer carrier lifespan (τ~500 ps) serves the requirement better. The lifetime of inter-band recombination is about a hundred times higher than inter sub-band lifetime, as reported by Liu et al in InAs/GaAs QDIP at room temperature [73]. Through k.p model calculations, Lim et al have demonstrated that for smaller QDs with very few accommodated bound states (at most two), the oscillator strength for 'bound to bound' excitation can be highly enhanced due to larger overlapping between electron-hole wave function. This, in turn, can significantly enhance the inter-band transition probability and suppress long-wavelength inter-subband transitions. Therefore, few monolayers high SML QDs may be a good choice to be used as the active medium of high-performance QD photodetector based on short wavelength (NIR) inter-band absorption [73].

Carrier confinement in deep energy levels of QDs helps to suppress the detector's dark current up to high temperature. Due to three-dimensional carrier confinement and phonon-bottleneck, QDIP serves as a better element to control the dark current as compared to the quantum well photodetector (QWIP). The performance can be sustainable if a sufficient amount of such capture centres are present in the active medium which can be achieved by increasing the QD density. Jahromi et al have reported that the resulted photodetection performance for QD based PDs maximizes at some optimal values of QD size and density [74]. Small size (1-3 nm) SML QDs with strong carrier confinement and high areal density (10^{10}-10^{11} cm^{-2}) can be handy in providing such trap centres for dark carriers and giving rise to high detectivity. The QD size-

dependent inter-band absorption gives the further provision of tuning the photo-response over a wavelength range in the infrared (IR) region [71].

But the photodetector device architecture designed to achieve high detectivity usually suffers from having slow response speed. Detectivity can be enhanced by simultaneously increasing the responsivity, achieved by the large photocarrier lifetime in QD states and suppressing the dark current. But this large carrier lifetime severely limits the detector speed, as reported by Maulu et al in PbS QD-based IR photodetector [75]. Both of them need to be taken care of simultaneously for high-temperature sustainable photodetection in fast switching optoelectronic applications [76]. According to previous research, the detector's response speed is also limited by the transit time of the locally photoexcited carriers to the electrode through the quasi-neutral active region by the slow process of diffusion [77]. However, there is an alternative direct photocarrier escape pathway by the process of tunnelling through the states of nearby QDs which can non-dissipatedly convey the charge carriers to the edge of the depletion region followed by sweeping out by the depletion field. Chu et al have proposed a theoretical model of tunnel dependent photo-response in QDIP, that can effectively determine the detector operational speed [77]. With the provision of increasing the in-plane density of SML-QDs, the strength of interdot carrier tunnelling can be tailored which can help to control the speed of charge transport along the lateral conductive channel. Tunnel assisted carrier escape and subsequent transport can also lead to the greater quantum efficiency of the detector, as reported by Ryzhii et al [78]. The external quantum efficiency (EQE) of QD-PD is directly proportional to two fractional efficiencies related to the processes of excitonic dissociation into individual charge carriers and photocarrier extraction by transport through the QD active region. According to the previous report, both these processes are limited by the probability of charge recapturing down to QD ground state by recombination characterized by a timescale called the time of persistence under illumination [79]. Therefore, microscopically it all boils

down to the competition between the strength of photocarrier escape ($1/\tau_{esc}$) and recombination ($1/\tau_{rec}$) which determines the macroscopic PD parameters like photoresponsivity and response speed.

I have worked on controlling the relative yield of the co-existing phases in Ge nanocrystal by physically adjusting the kinetic energy of stream the Ge ionic clusters, bombarding on a crystalline substrate in ion cluster beam (ICB) deposition chamber. We have categorically shown the feasibility of achieving higher yield of the novel Ge tetragonal phase by controlling the cluster beam energy. We have investigated the consequent changes in structural and optical properties of the as-grown and photo-oxidized Ge-nanocrystalline thin film as a function of accelerating potential. Following that, we worked on investigating the feasibility of tuning of photoemission and photo-carrier transport properties of InAs/GaAs SML-QD by controlling the active sub-monolayer coverage of InAs per layer. We have analyzed the effect of varying InAs sub-monolayer coverage upon the combined charge carrier recombination dynamics and transport from the temperature dependence of PL and photocurrent response properties of InAs/GaAs SML-QD heterostructure and described in terms of relative lifetimes of the excitonic recombination and inter-dot carrier tunnelling.

1.3 Structure and outline of the thesis

The focus of this thesis is to investigate the structure and optical properties of quasi zero-dimensional confined Gr IV elemental Ge nanocrystal and Gr III/V elemental InAs/GaAs self-assembled semiconductor quantum dot structure and their implementation in both light emission and photodetector applications. With this goal, the research work can be divided into two major parts focussed on 0-D nanostructures belonging to IV and III/V group of semiconductors as follows:

(i) The first part of the thesis is devoted to the study of the phase-selective growth of Ge nanocrystalline films by ionized cluster beam deposition technique. The variation in structural and optical properties of these films is investigated as a function kinetic energy of Ge cluster beam. We worked on tuning the luminescence properties in the visible region by controlling the relative amount of novel tetragonal ST-12 and the normal cubic phase of Ge. In addition to that, investigation of light emission and oxidation states of the subsequent photo-oxidized Ge nanocrystalline thin films are performed.

(ii) In the second part of the thesis, the relative variation of the structural, morphological and optical properties of Molecular beam epitaxy grown InAs/GaAs sub-monolayer quantum dots heterostructure has been investigated as a function of sub-monolayer coverage. This includes the combined study of photocarrier transport and recombination with their related lifetimes through analysis of temperature-dependent light emission and electro-optic properties of the sub-monolayer quantum dots. We have investigated the relative effect of the excitonic recombination and inter-dot carrier tunnelling upon the quantum gain properties as a function of InAs sub-monolayer coverage. This technique has been extended to simultaneously tune near-infrared photodetector performance by varying InAs sub-monolayer coverage. In a nutshell, the work is all about studying the structural and optical properties of MBE grown self-assembled InAs/GaAs quantum dots and describe the temperature dependence of PL and IR-photodetector performance in terms of parameters of photocarrier dynamics as a function of

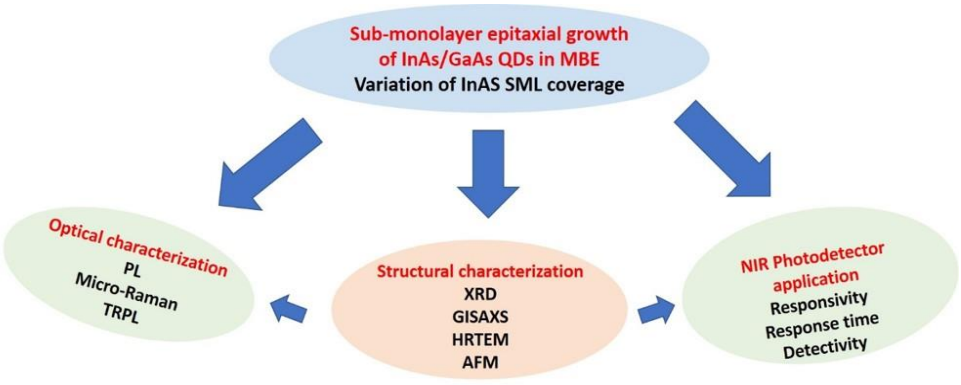

Fig.1.6 *Schematic representation of combined study of MBE grown InAs/GaAs SML QD heterostructure as a function of InAs sub-monolayer coverage.*

InAs sub-monolayer coverage. The associated experimental and simulation studies are mainly divided into three main areas, as schematically shown in Fig.1.6.

1.3.1 Outline of the thesis

The complete work has been described by arranging them into different chapters as follows

Chapter 2 represents basic principles of different experimental technics, like XRD, micro-Raman spectroscopy, AFM, GISAXS, HRTEM; PL spectroscopy for optical characterization; Spectral photocurrent measurement, dark current measurement, I-V characteristic and transient photo-response measurement for photodetector device characterization.

Chapter 3 represents the phase selective growth of Ge nanocrystalline thin film by ionized cluster beam deposition technique and characterization of their crystallographic, structural and optoelectronic properties followed by the light-emitting properties of the corresponding photo-oxidized films.

Chapter-4 represents the self-assembled growth of GaAs-hosted InAs sub-monolayer quantum dot multi-stack heterostructure by molecular beam epitaxy technics.

Chapter-5 represents a study of low-temperature photoluminescence spectra and carrier localization in correlation with strain, size and in-plane structural details of quantum dots as a function of InAs sub-monolayer coverage.

Chapter-6 represents photocarrier relaxation and lifetime study from TDPL measurement.

Chapter-7 represents near-IR photodetector application of InAs/GaAs SML-QDs with the tuning of spectral photo-response, operation speed and dark current characteristics as a function of temperature by varying sub-monolayer coverage.

1.4 Bibliography

[1] P. Lam, J. Wu, M. Tang, Q. Jiang, S. Hatch, R. Beanland, J. Wilson, R. Allison, and H. Liu, Sol. Energy Mater. Sol. Cells **126** (2014) 83.

[2] S. Takeoka, M. Fujii, S. Hayashi, and K. Yamamoto, Phys. Rev. B - Condens. Matter Mater. Phys. **58** (1998)7921.

[3] J. Lee, V. C. Sundar, J. R. Heine, M. G. Bawendi, and K. F. Jensen, Adv. Mater. **12** (2000)1102.

[4] H. Y. Liu, I. R. Sellers, M. Gutierrez, K. M. Groom, W. M. Soong, M. Hopkinson, J. P. R. David, R. Beanland, T. J. Badcock, D. J. Mowbray, M. S. Skolnick, J. Appl. Phys. **96** (2004) 1988–1992.

[5] P. Bhattacharya, K. Kamath, J. Singh, IEEE Transactions on Electron Devices, **46** (1999) 871-83.

[6] L. E. J Brus, Chem. Phys **80** (1984) 4403–4409.

[7] M. G. Bawendi, M. L. Steigerwald, L. E. Brus, Rev. Phys. Chem **41 (**1990) 477–496.

[8] P. Alivisatos, Perspectives on the physical chemistry of semiconductor nanocrystals. J. Phys. Chem **100** (1996) 13226–13239.

[9] J. D. Joannopoulos, M. L. Cohen and I. Materials, Solid State Commun. **11** (1972) 549.

[10] Y. Batra, D. Kabiraj and D. Kanjilal, Solid State Commun. **143** (2007) 213.

[11] Y. Saito, J. Cryst. Growth **47** (1979) 61.

[12] J. Diao, K. Gal and M. L. Dunn, Nat Mater **2** (2003) 656.

[13] S. J. Kim, O. K. Quy, L. Chang, Eric A. Stach, Carol Handwerker and Alexander Wei, J. Mater. Chem **20** (2010) 331.

[14] D. J. Eaglesham and M. Cerullo, Phys. Rev. Lett. **64 (**1990**)** 1943

[15] N. Koguchi, S. Takahashi, and T. Chikyow, J. Cryst. Growth. **111 (**1991**)** 688–92.

[16] D. Leonard, M. Krishnamurthy, C. Reaves, S. Denbaars and P. M. Petroff, Appl. Phys. Lett. **63 (**1993**)** 3203–5.

[17] Y. Batra, D. Kabiraj, and D. Kanjilal, Solid State Commun. **143** (2007).213.

[18] Z. Xu, K. Leosson, D. Birkedal, V. Lyssenko, J. M. Hvam, and J. Sadowski, Nanotechnology **14** (2003) 1259.

[19] D. Z. Y. Ting, S. V. Bandara, S. D. Gunapala, J. M. Mumolo, S. A. Keo, C. J. Hill, J. K. Liu, E. R. Blazejewski, B. Rafol, and Y. C. Chang, Appl. Phys. Letters **94** (2009) 111107.

[20] D. Bimberg, M. Grundmann, and N. N. Ledentsov, Quantum Dot Heterostructures, John Wiley & Sons, 1998.

[21] Lenz, H. Eisele, J. Becker, J.-H. Schulze, T. D. Germann, F. Luckert, K. Pötschke, E. Lenz, L. Ivanova, A. Strittmatter, D. Bimberg, U. W. Pohl, and M. Dähne, Atomic structure and optical properties of InAs sub-monolayer depositions in GaAs, J. Vac. Sci. Technol. B 29 (2011) 04D104,

[22] M. Sugarawa, Ed., Self-assembled InGaAs/GaAs quantum dots, Academic Press, 1999.

[23] V. A. Shchukin, N. N. Ledentsov, and D. Bimberg, Epitaxy of nanostructures, Springer Verlag, 2004.

[24] Stangl, V. Holy, and G. Bauer, Structural properties of self-organized semiconductor nanostructures, Rev. Mod. Phys. **76** (2004) 725.

[25] D. J. Eaglesham and M. Cerullo, Phys. Rev. Lett. **64 (**1990) 1943–6.

[26] Jayita Patwari, Hemant Ghadi, Samim Sardar, Jashan Singhal, Binita Tongbram, Sanjib Shyamal, Chinmoy Bhattacharya, Subhananda Chakrabarti, Samir Kumar Pal, Mater Res Express **4** (2017) 016301.

[27] Germann, T. D. Strittmatter, A. Pohl, J. Pohl, U. W. Bimberg, D. Rautiainen, J.

Guina, M. Okhotnikov, O. G. Appl. Phys. Lett. **92** (2008) 101123.

[28] S. Mukherjee, A. Pradhan, S. Mukherjee, T. Maitra, S. Sengupta, B. Satpati, S. Chakrabarti, A. Nayak, S. Bhunia, J of Luminescence **210** (2019) 311-321.

[29] R. Dingle and C. H. Henry C H, *Patent Number* US3982207 A. (1976).

[30] M. Asada, Y. Miyamoto and Y. Suematsu, IEEE J. Quantum Electron. **22** (1986) 1915–21.

[31] Y. Arakawa and H. Sakaki, Appl. Phys. Lett. **40** (1982) 939–41.

[32] P. Reiss, M Carriere, C Lincheneau, L Vaure, S Tamang, Chem Rev **116 (**2016**)** 10731-819.

[33] S. Kasper, S. M. Richards, Acta Crystallogr. **17** (1964) 752.

[34] X. L. Zhou, Y. H. Chen, C. H. Jia, X. L. Ye, B. Xu, and Z. G. Wang, J. Phys. D. Appl. Phys. **43** (2010).

[35] Y. Saito, J. Cryst. Growth **47** (1979) 61.

[36] S. Sato, S. Nozaki, H. Morisaki, and M. Iwase, Appl. Phys. Lett. **66** (1995) 3176.

[37] Y. Kanemitsu, H. Uto and Y. Masumoto, Y. Maeda, Appl. Phys. Lett.**61** (1992) 2187.

[38] D. Tomanek and M. A. Schluter, M. A., Phys. Rev. B. **36** (1987) 1208.

[39] J. D Joannopoulos and M. L. Cohen, Solid State Commun. **11** (1972) 549.

[40] J. P. Wilcoxon, P. P. Provencio, and G. A. Samara, Phys. Rev. B. **64** (2001) 035417.

[41] Yamada, G. H. Takaoka, Jpn. J. Appl. Phys. **32** (1993) 2121.

[42] Nogami, Y. Abe, Appl. Phys. Lett. **65** (1994) 2545.

[43] G Zhu, C.W. White, J. D. Budai, S. P. Withrow, and Y. Chen, J. Appl. Phys. **78** (1995) 4386.

[44] Y. Maeda, Y. Tsuamoto, Y. Yazawa, Y. Kanemitsu and Y. Masumoto, Appl. Phys. Lett. **59** (1991) 3168.

[45] S. T. Ngiam, Klavs F. Jensen, K. D. Kolenbrander, J. Appl. Phys. **76** (1994) 8201.

[46] Tersoff and F.K. Le Goues, Phys. Rev. Lett. **72** (1994) 3570.

[47] S. Nozaki, S. Sato, S. Rath, H. Ono, H. Morisaki, Bull. Mater. Sci. **22 (**1997**)** 377.

[48] E. B. Gorokhov, V. A. Volodin, D. V Marin, D. A. Orekhov, A. G. Cherkov, A. K. Gutakovskii, V. A. Shvets, A. G. Borisov & M. D. Efremov, Semiconductors **39** (2005) 1168.

[49] T. Z. Takagi, Phys. D. Atoms, Molecules and Clusters, **3** (1986) 271.

[50] S. F. Tang, C. D. Chiang, P. K. Weng, Y. T. Gau, J. J. Luo, S. T. Yang, C. C. Shih, S. Y. Lin, S. C. Lee, IEEE Photonics Technol. Lett. **18** (2006) 986.

[51] D. V. Regelman, U. Mizrahi, D. Gershoni, E. Erenfreund, W. Schoenfeld, P. M. Petroff, Phys. ReV. Lett. **87** (2001) 257401.

[52] J. H. Davies, 1998, *The Physics of Low-dimensional Semiconductors* (Cambridge University Press).

[53] Berryman, S. Lyon, and M. Segev, Appl. Phys. Lett. **70 (**1997) 1861–3.

[54] D. Pan, E. Towe, and S. Kennerly, Appl. Phys. Lett. **73 (**1998**)** 1937

[55] B. J. Riel, American Journal of Physics **76** (2008) 750.

[56] C. Kittel, 1995, *Introduction to Solid State Physics*, 7th edition (New York: Wiley).

[57] Phu Lam, Jiang Wu, Mingchu Tang, Qi Jiang, Sabina Hatch, Richard Beanland, James Wilson, Rebecca Allison, Huiyun Liu, Solar Energy Materials & Solar Cells **126** (2014) 83–87.

[58] Thomas Switaiski and Ulrike Woggon, Phys. Rev. B. **88** (2013) 035314.

[59] L. Krestnikov, N. N. Ledentsov, A. Hoffmann, and D. Bimberg, Phys Status Solidi A **183** (2001) 207.

[60] Seravalli, M. Minelli, P. Frigeri, P. Allegri, V. Avanzini and S. Franchi, Appl. Phys. Lett. **82** (2003) 2341.

[61] Feng Wu, Jun Zhang, Shuai Wang, Hanling Long, Jiangnan Dai, Zhe Chuan Feng,

Zheng Gong, and Changqing Chen, Opt Mater Express **5** (2015) 11

[62] L. Krestnikov, M. Straßburg, M. Caesar, A. Hoffmann, U. W. Pohl, D. Bimberg, N. N. Ledentsov, P. S. Kop'ev, Zh. I. Alferov, D. Litvinov, A. Rosenauer, D. Gerthsen, Phys. Rev. B **60** (1999) 8695.

[63] W. H. Chang, T. M. Hsu, C. C. Huang, S. L. Hsu, C. Y. Lai, N. T. Yeh, T. E. Nee, and J. I. Chyi, Phys. Rev. B **62** (2000) 11.

[64] Chu, A. Zrenner, M. Bichler and G. Abstreiter, Appl. Phys. Lett.**79** (2001) 2249.

[65] W. H. Chang, T. M. Hsu, C. C. Huang, S. L. Hsu, C. Y. Lai, N. T. Yeh, T. E. Nee, and J. I. Chyi, Phys. Rev. B **62** (2000) 11.

[66] P. Qiao, C. Y. Lu, D. Bimberg and S. L. Chuang, Opt Express **21** (2013) 25.

[67] P. W. Fry, J. J. Finley, L. R. Wilson, A. Lemaıˆtre, D. J. Mowbray, M. S. Skolnick, M. Hopkinson, G. Hill and J. C. Clark, Appl. Phys. Lett. **77** (2000) 4344.

[68] T. Tackeuchi, A. Kuroda, K. Mase, Y. Nakata and N. Yokoyama, Phys. Rev. B **62** (2000) 1568.

[69] E. O. Gobel, H. Jung, J. Kuhl, and K. Ploog, Phys. Rev. Lett. **51** (1983) 17.

[70] Barve, J. Shao, Y. D. Sharma, T. E. Vandervelde, K. Sankalp, S. J. Lee, S. K. Noh, and K. Krishna, IEEE J. Quantum Electron. **46** (2010) 7.

[71] Rogalski, J. Phys.: Conf. Ser. **146** (2009) 012030.

[72] P. Lam, J. Wu, M. Tang, Q. Jiang, S. Hatch, R. Beanland, J. Wilson, R. Allison, H. Liu Sol Energ Mat Sol C **126** (2014) 83–87.

[73] H. C. Liu, C. Y. Song, A. Shen, M. Gao, Z. R. Wasilewski and M. Buchanan, Appl. Phys. Lett. **77** (2000) 2437.

[74] H. D. Jahromi, M. H. Sheikhi, and M. H. Yousefi, Opt Laser Technol **43** (2011) 1020–1025.

[75] Maulu, J. N. Arenas, P. J. Rodríguez-Cantó, J. F. Sánchez-Royo, R. Abargues, I.

Suárez and J. P. Martínez-Pastor, Nanomaterials **8** (2018) 677.

[76] P. Clifford, G. Konstantatos, K. W. Johnston, S. Hoogland, L. Levina, and E. H. Sargent, Nat Nanotechnol **4** (2009) 40-44.

[77] Chu, A. Zrenner, M. Bichler and G. Abstreiter, Appl. Phys. Lett. **79** (2001) 2249.

[78] V. Ryzhii, Jpn. J. Appl. Phys. 40 (2001) 148–150.

[79] J. P. Clifford, G. Konstantatos, K. W. Johnston, S. Hoogland, L. Levina, and E. H. Sargent, Nat Nanotechnol **4** (2009) 40-44.

[80] Zhisheng Zhao, Fei Tian, Xiao Dong, Quan Li, Qianqian Wang, Hui Wang, Xin Zhong, Bo Xu, Dongli Yu, Julong He, Hui-Tian Wang, Yanming Ma, and Yongjun Tian, J. Am. Chem. Soc. **134** (2012) 12362-12365.

Chapter 2

Experimental characterization techniques

2.1 Introduction

The characterization of semiconductor nanostructure is a very important aspect of the investigation of the material properties. The material characterization techniques are mainly based on direct imaging by microscopy and indirect measurement by spectroscopy or x-ray scattering. Transmission electron microscopy, scanning electron microscopy and atomic force microscopy are the most commonly used microscopic techniques for material characterization. Photoluminescence spectroscopy, Raman spectroscopy, and Absorption spectroscopy are the most useful spectroscopic techniques. X-ray diffraction (XRD), x-ray reflectivity and Grazing incidence small-angle x-ray scattering (GISAXS) techniques are based on x-ray scattering from materials. These techniques were employed to investigate the structural, strain, morphological and optical properties of the grown nanostructures. The device performance of the fabricated quantum dot infrared photodetector has been studied by spectral photocurrent response and I-V measurements. The various employed experimental techniques are discussed in this chapter in detail.

2.2 Structural and morphological characterization

The structural and morphological properties of the grown nanostructures are studied by several microscopic, spectroscopic and x-ray scattering techniques. Strain and structural details have been characterized through direct imaging by the transmission electron microscope. Atomic force microscopy measurements are performed to characterize the morphology of the surface nanostructures. Raman spectroscopy is used for quantum dot size measurement and characterization of phonon modes. X-ray scattering experiments, like XRD and GISAXS are performed to characterize the strain, in-plane structural and crystallographic properties of the quantum dot structure.

2.2.1 Atomic Force Microscopy

Atomic force microscopy (AFM) provides information on surface topography by generating a 3D profile of the surface with characteristic resolution up to nanoscale. This is imaged by scanning a sharp tip (probe) over the sample surface measuring the force between the probe (<10 nm) and the surface at very small separation (0.1-8 nm). The experimental set up is equipped with a flexible cantilever that supports the AFM tip, a laser diode, a piezoelectric motor, and a position-sensitive photodetector, as shown in Fig.2.1. The repulsive Van der Waals force acting between the tip and the surface causes the cantilever to deflect which is further magnified by a laser beam reflection and finally recorded as the vertical displacement of the tip. Most available tips for commercial purposes are made of materials like Si_3N_4 or tungsten spikes designed to have very high aspect ratios.

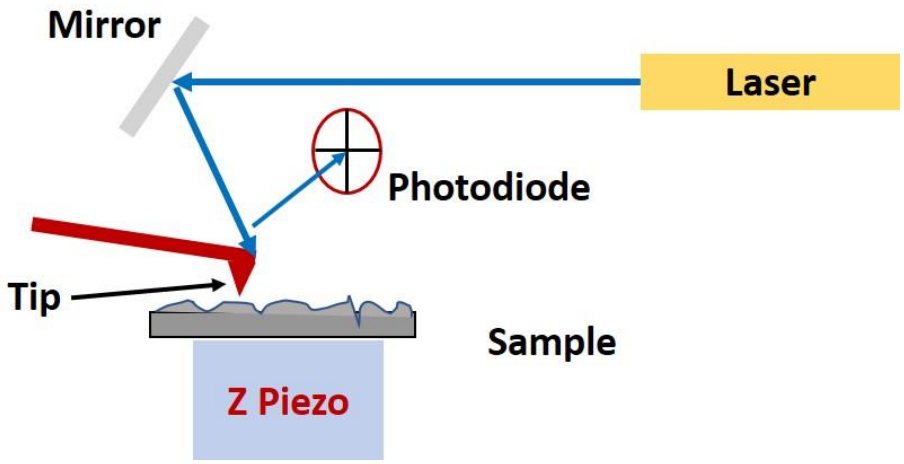

Fig.2.1 *AFM measurement set up consisting of a diode laser, flexible cantilever with a sharp tip, a position-sensitive photodetector and a piezoelectric motor.*

AFM is typically operated in three basic modes [1]: contact mode non-contact mode and tapping mode.

Contact mode

It is a fast and convenient way of imaging a relatively hard surface with a probe to surface separation of less than 0.5 nm. This mode is based on registering the variation in tip deflection

due to the force of repulsion between the tip and the surface while scanning. The main advantage of the contact mode is very high resolution for probing the surface topography. But this mode is also limited by the possibility of damaging or deforming soft sample surface due to the formation of large lateral frictional forces on the sample as the tip is "dragged" over the surface. AFM in contact mode is operated in two possible ways as following:

Constant height scanning: In this mode, the height of the tip from the sample surface remains fixed as it scans. Therefore, the spatial variation of the cantilever deflection is used directly to generate the topographic image. This mode is mainly used for taking images of atomically smooth surfaces where the variation in cantilever deflection is small. This mode is especially suited for high-speed scanning. The vertical tip position and associated cantilever deflection while scanning the sample surface are schematically shown in Fig.2.2 (a).

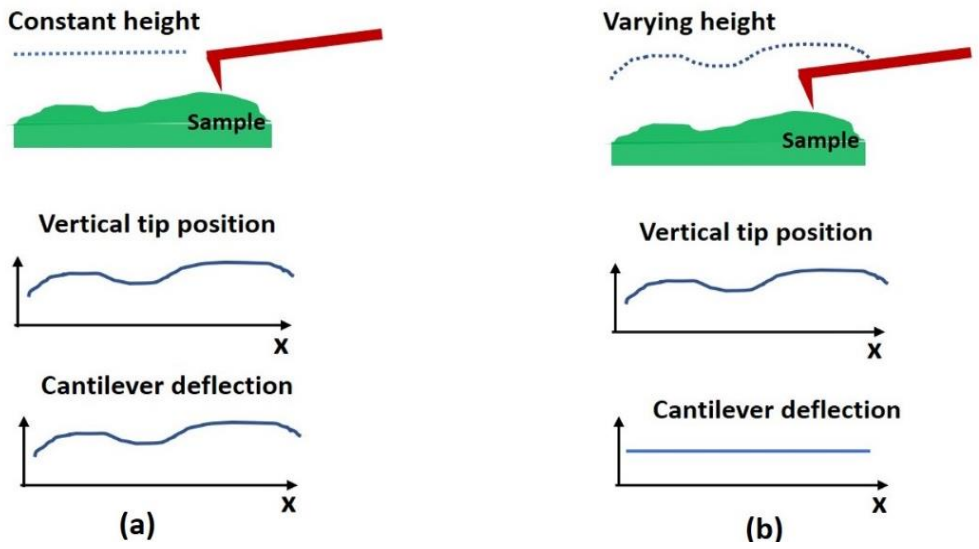

Fig.2.2 Schematic representation of (a) constant height and (b) constant force contact mode AFM scan, showing the variation of vertical tip position and cantilever deflection along the direction of scanning over the surface.

Constant force scanning: In this mode, the cantilever deflection is kept constant which suggests that the total force applied to the sample remains constant. The constant deflection of the scanner is served as the input to a feedback circuit that moves the scanner up and down in the vertical (z) direction, according to the topography of the surface. The AFM image is generated by counting the topographic data set registered from the scanner's z-motion. The

vertical tip position and associated cantilever deflection while scanning the sample surface are schematically shown in Fig.2.2 (b).

Non-contact mode

In this mode, the tip (0.1-10 nm probe-surface separation) does not contact the sample surface, but it oscillates above the surface while scanning by maintaining a spatial separation of 0.1 nm to 10 nm from the probed surface. The variation in surface topography is measured by monitoring cantilever deflection due to changes in amplitude of interacting attractive Van der Waals forces which is amplified by using a feedback loop. Comparatively lower exerted force on the sample (10^{-12} N), helps to probe soft surfaces in this mode without damaging the surface. But, the possibility of interference of the contaminant layer on the surface with the probe oscillation, extended probe lifetime for better imaging, limits the resolution below the atomic scale. The operation of this mode is also accompanied by the requirement of ultra-high vacuum (UHV) which heavily hampers the performance. The physical probe used in AFM imaging is not ideally sharp for imaging the true surface topography. Rather, the imaging reflects the interaction of the probe with the sample surface recorded through probe convolution.

Tapping mode

This is intermediate of the above two modes where the probe taps the surface for a sufficiently low contact time while oscillating at its resonant frequency (usually hundreds of kHz) keeping an average separation is 0.5 nm to 2 nm from the surface. This makes the tapping mode extremely useful for topographical imaging of soft surfaces at the cost of slower scan speed. Tapping mode enjoys the advantages of the above two modes. It eliminates interaction force with the sample by intermittently contacting the surface by oscillating with sufficient amplitude.

2.2.2 Transmission Electron Microscopy

Transmission electron microscopy (TEM) provides structural and chemical information through high-resolution imaging by passing high energetic electron beam through the sample [2]. The cross-sectional view in TEM imaging is usually employed for structural analysis of thin films with interfaces and embedded nanostructures. The indispensability of probing structures with an electron beam for the microscopic detailing at the atomic scale with a resolution of few Å makes TEM a powerful characterization technique. Normal optical microscopes with its spatial resolution limited to a few micrometers, imaging of materials at the nanoscale regime are not possible. A high resolution can be achieved by accelerating the electrons to sufficient energy to have the de Broglie wavelength well below that of light.

In TEM, the electrons are accelerated by applying high voltage, typically in the range of 200 to 300 kV which is good enough for the electrons to be able to pass through such a thin sample. By employing high energetic electrons associated with short de Broglie wavelength enables TEM to image structural features of length scale from atoms to few hundreds of nanometers which is characteristically smaller than that imaged by scanning electron microscopy (SEM). Nowadays, atomic resolution images are routinely achieved by using High-Resolution TEM (HRTEM). A modern TEM can provide a resolution (~0.1 nm) smaller than the interatomic distance in a crystalline sample, allowing direct imaging of atoms. Quantitative analysis of the chemical properties of a single nanocrystal is also possible by focusing the electron beam within a diameter of ~ 0.2 nm. TEM is also significantly efficient for precise characterization of size, shape and inter-particle correlation of embedded nanostructures and crystallinity of thin film [3]. However, TEM also has its limitations. Usually, sample preparation (thinning), especially for cross-sectional TEM is quite tedious and time-consuming. Moreover, the high penetration power of the electron beam is subjected to the possibility of damaging the soft

specimen. It is also difficult to image the surface as the beam penetrates deep through the sample, imaging the bulk only.

2.2.2.1 TEM specimen preparation

For TEM imaging, it demands special attention to specimen preparation before characterization. The liquid sample can be inserted by drying them on a carbon-coated Cu grid. But the solid sample needs to be made electron transparent following the steps described below.

Initial thinning

In general, the lateral dimension of the specimen used for TEM is 3 mm in diameter. Therefore, a nearly about 3 mm diameter disc is cut from the sample using a disc grinder (Gatan). Then, they are thinned by silicon carbide paper before dimpling.

Dimpling

After the initial thinning, the central portion of the sample is dimpled to reduce its thickness more. By this process of selective thinning, the chance for breaking of the sample is diminished. After that, the sample is placed on the turntable of the dimple grinder rotating at a constant speed. The speed of rotation can be varied according to the hardness of the sample. A diamond paste is applied to the sample. The grinding wheel is lowered on the sample by fixing a certain dimple thickness. After dimpling, the final polishing is done with a 0.25 μm grain size diamond paste.

Ion milling

The above discussed mechanical thinning techniques are not enough to make the sample electron transparent. For that purpose, a Precession Ion Milling System (PIPS) (Gatan, Pleasanton, CA model) is usually employed where Argon ions are impinged on the dimpled sample to knock out atoms from it to make it electron transparent. A CCD attachment in conjugation with an LCD is used to monitor the sample inside the chamber. In our present ion milling system, there is a provision of varying ion energy up to 6 Kev and the angle of incidence

can be varied in the range of ±10^{o}. The electron transparency of the sample is confirmed by observing the appearance of a tiny perforation in the dimpled region as viewed in the LCD.

Sample preparation for cross-sectional TEM

The cross-sectional view in TEM is necessary to extract the detailed structural parameters of epitaxial layers. At first, two pieces of the sample of less than 3 mm width are cut and bonded with epoxy, keeping the deposited or the treated side face to face. For this purpose, Gatan Epoxy is used which consists of two parts, a resin, and a hardener, mixed in an 8:1 ratio. Then the sample is heated at 120^{o}C to produce strong adhesion. Now the composite is inserted into a brass tube and the empty place is filled with thin dummy substrates and epoxy. The sample contained inside the brass tube is cut to make 0.5 mm discs, using a diamond wire saw. The disc is now mechanically thinned to 60-100 µm, with the disc grinder and silicon carbide paper of different grit sizes. The central portion of this thin sample is now dimpled down to 30 µm thickness and inserted inside the PIPS chamber for ion milling. The electron transparent sample for the cross-sectional TEM study is obtained only after the ion milling.

2.2.2.2 Experimental setup

Different components of a typical TEM is represented by a schematic as shown in Fig.2.3. Stream of monochromatic electrons is generated in an electron gun placed at the top of the instrument and subsequently focused in the form of a coherent beam by two condenser lenses (lens 1 and 2). Then, by employing a condenser aperture system, most of the off-axis (optic axis as indicated by the dotted line) electrons are cut off and the width of the beam is reduced. Now, when the stream of electrons strikes the specimen, the electrons subsequently undergo processes like back-scattering, emission of Auger electrons, secondary electrons, x-ray, cathodoluminescence (CL) and transmission which are schematically shown in Fig.2.4. Out of those electrons which pass through the thin specimen, some of them undergo scattering (both elastic and inelastic) due to their mutual interaction with the sample atoms and the rest of the

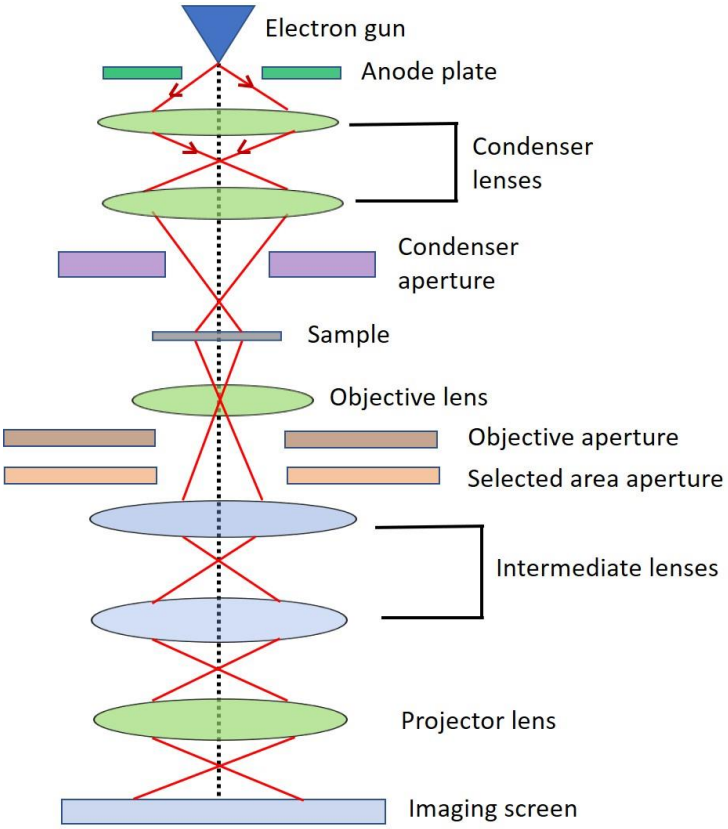

Fig.2.3 *Schematic representation of a TEM experimental set up showing different components.*

electrons transmit un-scattered right through the specimen in the forward direction without any interaction with the sample atoms. The elastic interaction (no loss of energy) of the incident electrons with the regular array of atoms in the specimen deflects the electron and produces a diffraction pattern. The inelastically scattered electrons lose energies after interaction with the sample atoms which are unique to each element associated with its unique bonding state. Therefore, the inelastic scattering in TEM can also be employed to extract the compositional and bonding information of the examined region of the specimen. The transmitted signal of electrons carries the information of the detected specimen which is subsequently focused by either an objective lens or selected area metal apertures depending upon the mode of imaging. The corresponding two TEM operations are image projection and diffraction pattern projection. In image projection mode, the objective aperture is employed which enables us to achieve high image contrast by guiding down the beam of the transmitted unscattered electrons and

constricting high-angle diffracted electrons. Now with decreasing specimen thickness, the transmission probability of such unscattered electrons increases immensely. As a result, the thinner or lighter parts of the specimen allow more unscattered electrons to pass through than the thicker or denser parts and give rise to a relatively brighter TEM image. On the other hand, in the diffraction pattern projection mode, the diffraction of electrons from periodically ordered

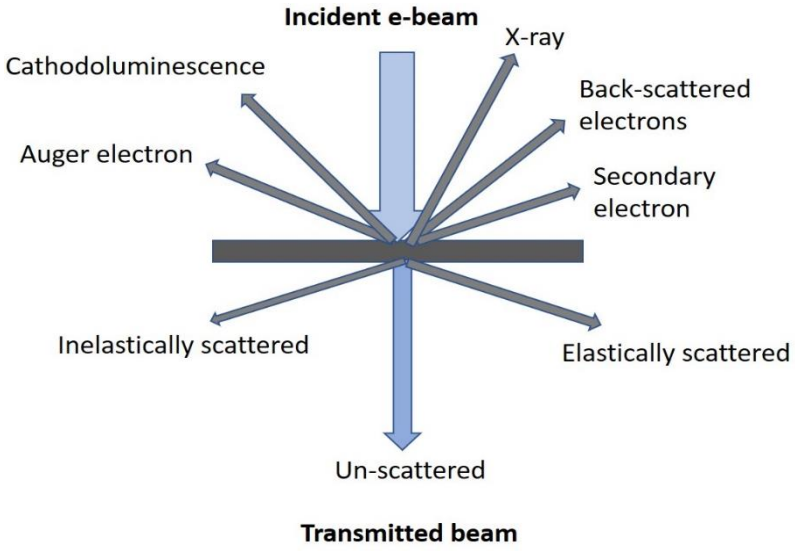

Fig.2.4 *Schematic representation of different physical processes when an electron beam encounters a material.*

atomic arrangements in the sample is investigated as facilitated by the selected area aperture.

This is mediated by elastic scattering of the incident electrons from the periodic crystal planes regularly arranged atoms in the specimen following Bragg's law of diffraction. The divergent beam of the scattered electrons is collected by using a system of magnetic lenses to which finally form patterns of diffraction spots. These diffraction patterns are the guidelines to identify the crystalline structure, lattice plane orientation, atomic arrangement and ordering in the physical area that has been probed. Therefore, this mode of TEM imaging is also known as Selected Area Electron Diffraction (SAED). Then the emergent electron beam is guided through the intermediate and projector lenses along the vertical axis of the TEM tube before it strikes the fluorescent screen where the final image is formed.

2.2.3 X-ray scattering measurement

2.2.3.1 Grazing incidence small-angle X-ray scattering

Grazing incidence small-angle (GISAXS) is an important characterization technique for in-plane structural measurement of thin films containing surface roughness and embedded objects. Usually, this is obtained by plotting the sample scattered x-ray intensity distribution in different in-plane azimuthal directions as a function of q_x. GISAXS measurement has been performed to study the spatial arrangement and correlation among surface and embedded InAs quantum dots in a vertical heterostructure, along with different lateral directions over a plane perpendicular to the growth direction.

To study average dot to dot lateral separation and spatial ordering along with different lateral directions over the X-Y plane perpendicular to the growth direction, we have performed grazing-incidence small-angle x-ray scattering (GISAXS) study of the embedded QDs.

GISAXS measurements were carried out with a beam energy of 14 keV at the KEK beamline BL-12, Photon Factory, Japan. The sample was mounted on a 4-circle goniometer. This is designed to freely rotate over a horizontal table to select different in-plane crystallographic directions to azimuthally scan the sample around the sample surface normal for a fixed angle of incidence (α_i) with respect to the sample surface. In order to avoid scattering of x-ray with air molecules, the entire beam path from the goniometer has been coupled through an evacuated metallic cylinder. The geometrical configuration of the GISAXS setup is schematically shown in Fig. 2.5. For the measurements related to my thesis work, angle of incidence (α_i) has been set at 0.14^o, very close to the critical angle (α_c) of 0.16° for total external reflection for achieving better surface sensitivity. With this configuration, the penetration depth of x-rays in pure InAs is about 10 nm which is quite less than the thickness of the multi-structure sample. Thus, the collected scattered x-ray is limited to the illuminating surface and the examined

embedded quantum dot structure. Both the highly intense specularly reflected beam and the scattered intensity profile along q_x direction is recorded by a linear position-sensitive detector (PSD) mounted parallel to the sample surface at a fixed small exit angle (α_f) with respect to the sample surface. To avoid the overflow of the detector, the intensity of the strong central specular beam is attenuated by placing a thin metallic wire stopper in front of the detector. The instrumental resolution of the PSD for q_x scans is 3.2 x 10^{-3} $Å^{-1}$.

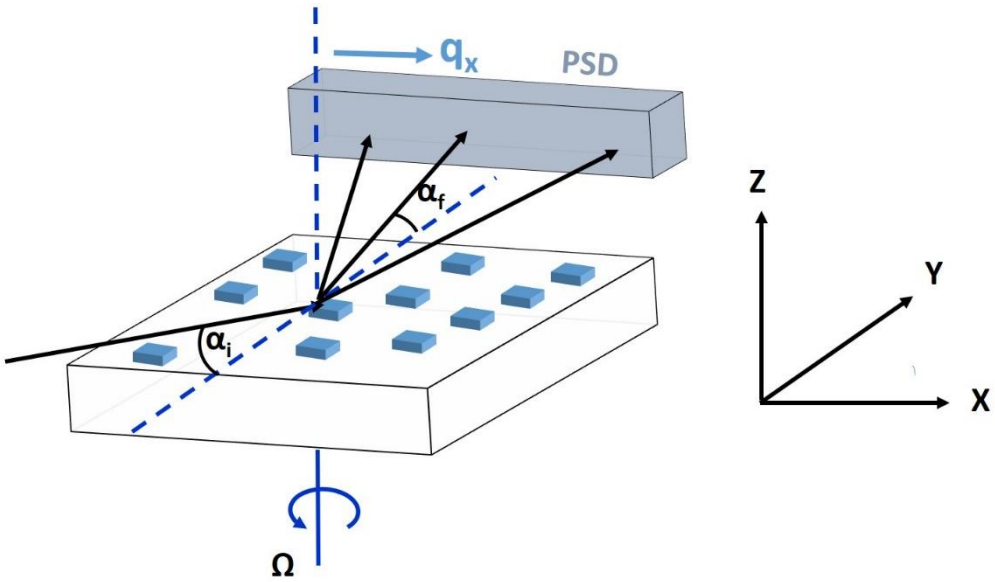

Fig.2.5 Schematic representation of geometrical configuration of scattering in GISAXS experimental arrangement.

2.2.3.2 X-ray diffraction

X-ray diffraction (XRD) is one of the powerful non-destructive techniques for structural characterization of crystalline thin film and epitaxial layers. X-rays with wavelength comparable to the atomic dimension along with high penetration power is best suited for probing structural arrangement of atoms and bringing out information, like strain and composition of bulk structure from deep into the material.

X-rays are scattered in various directions when it interacts with electrons in matter. Constructive interference of such scattered x-rays from the periodic atomic planes of the crystal is detected when Bragg's condition for diffraction is satisfied, as given by

$$2d_{hkl}sin\theta = \lambda \qquad (2.2.3.2.1)$$

where Θ is the Brag angle, λ is the wavelength of incident x-ray radiation and d_{hkl} is spacing between two diffracting (hkl) parallel lattice planes. X-ray Bragg diffraction from crystal planes is schematically depicted in Fig.2.6. For cubic crystals with lattice constant *a*, the perpendicular spacing is

$$d_{hkl} = a/(h^2 + k^2 + l^2)^{1/2} \qquad (2.2.3.2.2)$$

The lattice structures of Ge, GaAs, and InAs are basically cubic with two inter-penetrating fcc lattices separated by one-fourth of the lattice constant along the body diagonal.

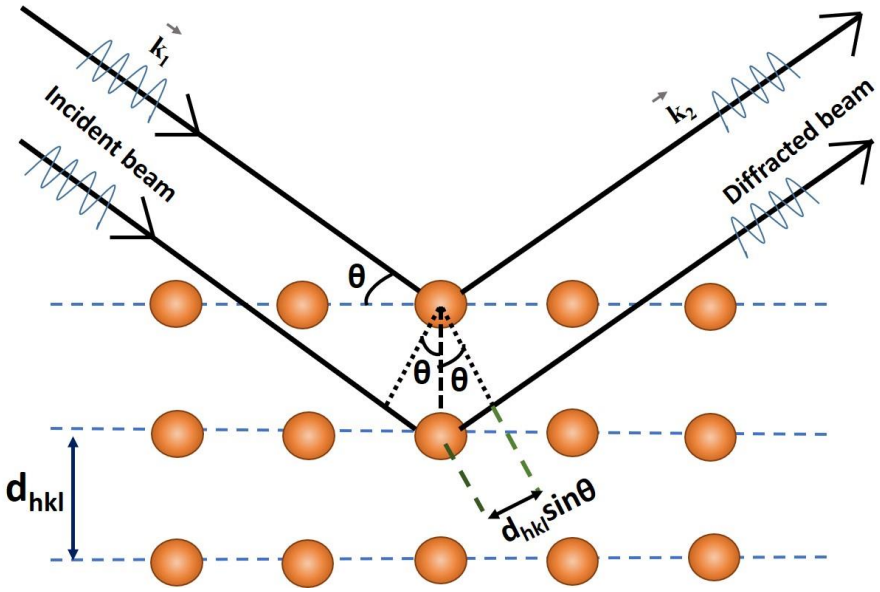

Fig.2.6 *Schematic representation of Bragg's diffraction of x-ray radiation from parallel set of crystal planes (hkl).*

Experimental setup

The XRD experiment is performed in a double crystal x-ray diffractometer by employing a monochromatic x-ray beam (Cu-K_α) with a continuously varying incident angle (θ) and recording a spectrum of diffraction intensity as a function of a diffraction angle (2θ). The wavelength of the employed x-ray radiation is 1.54 Å. The divergent x-ray radiation generated by an x-ray tube is collimated by the Soller slits in the diffractometer which is made to strike

the sample. The diffracted X-rays from the specimen are collected by receiving slits and made to converge through a monochromatic filter made of graphite crystal into the detector. This arrangement allows diffraction of only K_α radiation into the detector and can suppress the background radiation originating within the specimen and other wavelengths.

The elements of a diffractometer can have various types of geometric arrangements for the collection of x-ray data. For the usual θ-2θ scan, the x-ray incident beam is kept fixed, while both the sample stage (on which the sample is mounted) and the detector rotate around the axis perpendicular to the plane of incidence. The angle (θ) of incidence is continuously varied by rotating the sample stage. The detector is rotated at an angular speed twice that of the sample stage to ensure the collection of diffracted x-rays by maintaining angular θ-2θ correlation between the sample and detector rotation. The geometrical arrangement and corresponding relative movements of the x-ray source, specimen and detector are demonstrated in Fig.2.7. Only those crystallographic planes making angle θ with respect to the incident x-ray beam follow Bragg's law, contribute to the diffracted intensity collected by the detector. The diffractometer data acquisition and treatment are mainly processed by a computer interface.

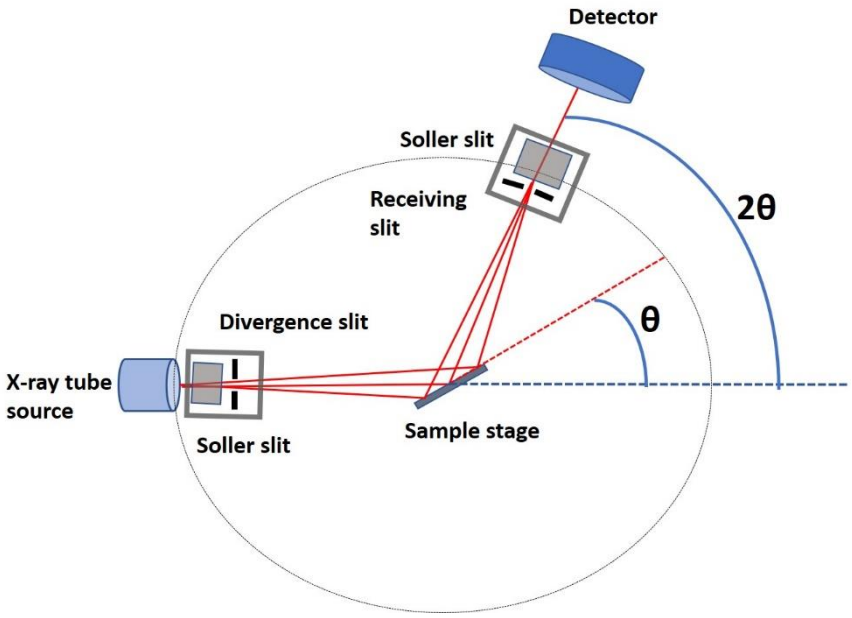

Fig.2.7 *A schematic demonstration of geometrical arrangement and corresponding relative movements of x-ray source, specimen and detector in θ-2θ scan.*

2.2.4 Raman spectroscopy

Working principle

When a beam of light is incident on a material, the incident photons are inelastically scattered through interactions with phonons, commonly known as Raman scattering. The interaction of the incident photon with various phonon modes in the material gives rise to a frequency shift of the scattered photons. Some of the outgoing photons are shifted to the lower energy values as a consequence of the absorption of the incident photon by atomic electrons, giving rise to the stokes line. Some of the outgoing photons gain energy, giving rise to the anti-stokes line, as some atomic electrons lose energy by emitting a photon.

Raman scattering is a second-order process and thus much weaker than other optical processes, like Photoluminescence. However, with the development of excitation sources and ultra-sensitive detectors, Raman Spectroscopy has become an extremely useful technique for characterizing semiconductor properties, like crystalline quality, crystallite size, phonon modes, the density of impurity states and lattice strain.

In this work, Raman scattering in back-scattering geometry has been employed to figure out crystalline phases, nano-crystallite size, and strain.

Experimental Setup

The measurement related to this thesis work has been performed by an 800 mm focal length Horiba Jobin Yvon HR-800 Raman spectrograph. A 20 mW He-Ne laser has been employed as the excitation source operating at a wavelength of 633 nm. The Raman scattered intensity is detected and analyzed by a charge-coupled device (CCD) detector maintained at liquid nitrogen temperature (77K) in conjugation with LabSpec software. The excitation and sample scattered radiation and different components of the set up are illustrated in Fig.2.8.

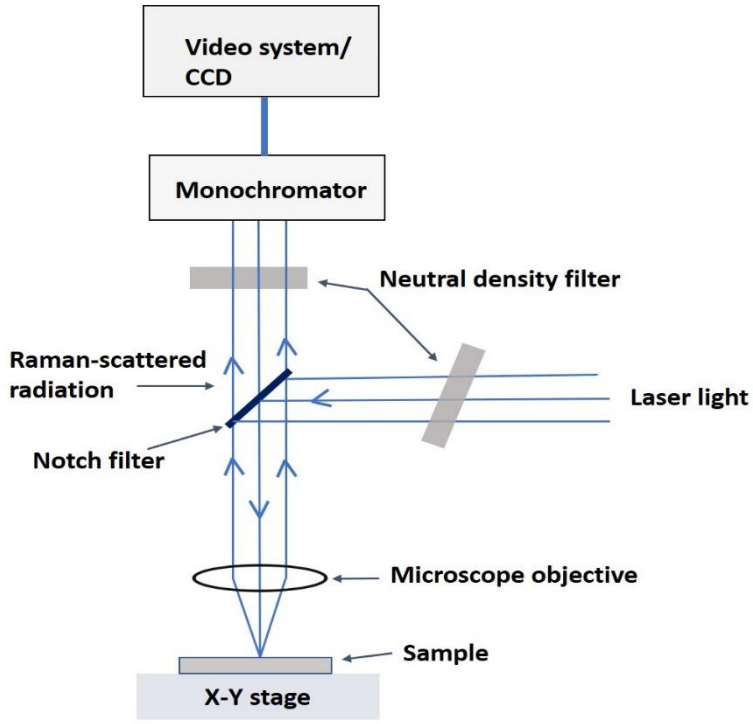

Fig.2.8 *Schematic representation of Raman spectroscopy set-up consisting of components like a laser, a monochromator, a set of neutral density filters, one Notch filter and a video system or CCD for monitoring.*

The incoming excitation laser radiation is incident on a notch filter which reflects and focuses the light on the examined sample through an objective lens. The backscattered Raman radiation from the sample and the reflected laser lights are transmitted back through collected by the microscope objective lens and are directed towards the notch filter which is finally collected by a monochromator. The notch filter rejects the laser transmission lines and only allows pure Raman scattered radiation to reach the spectrometer. The exciting laser light is taken through a laser filter to avoid the plasma lines. The HR-800 spectrometer scans over a selective spectral range by employing two gratings with a different operational spectral range of interest. A 600 g/mm and a 2400g/mm grating have been used for the scanning range of 0-2600 nm and 0-650 nm respectively. The CCD detector is calibrated by using the Raman shift of a standard Si reference sample. The exciting laser light travels through a laser filter to avoid plasma lines.

The microscope is equipped with four different objectives, one for UV light and the other three for visible light offering 10X, 50X and 100X magnification respectively. Six neutral density

filters are employed to reduce the intensity of the incident laser beam and the photoluminescence reaching the screen. according to the relation

$$I/I_0 = 10^{-D} \qquad (2.2.4.1)$$

Where D can vary in the range zero to four.

2.3 Optical characterization

Non-destructive experimental techniques, like optical absorption spectroscopy and photoluminescence spectroscopy, have been performed for optical characterization of semiconductor quantum dot structures.

2.3.1 Optical Absorption spectroscopy

UV-visible absorption spectroscopy is one of the most useful optical characterization techniques for studying the optoelectronic properties of nanostructures. This technique employs light absorption by the sample which is unique for each element.

A typical UV-visible spectrometer set-up contains the following components:

(i) Light source: The incident radiation covers a spectral range from ultra-violet (UV) to infrared (IR) by employing a deuterium lamp for UV range, tungsten lamp for visible (VIS) and IR ranges of the spectrum respectively.

(ii) Monochromator: The incident radiation is focused onto a monochromator to select a single wavelength from the polychromatic radiation and enables scanning over a desired range of frequencies.

(iii) A sample holder: The examined specimen is kept fixed on a sample holder.

(iv) Light detector: A light detector, usually in the form of a charge coupled device (CCD) or photomultiplier tube (PMT) is placed following the sample which measures the transmitted intensity of each monochromatic light after the absorption through the specimen.

v) A computer interface: Records and displays the absorption spectrum on a screen.

A typical UV-VIS spectrometer is schematically shown in Fig. 2.9.

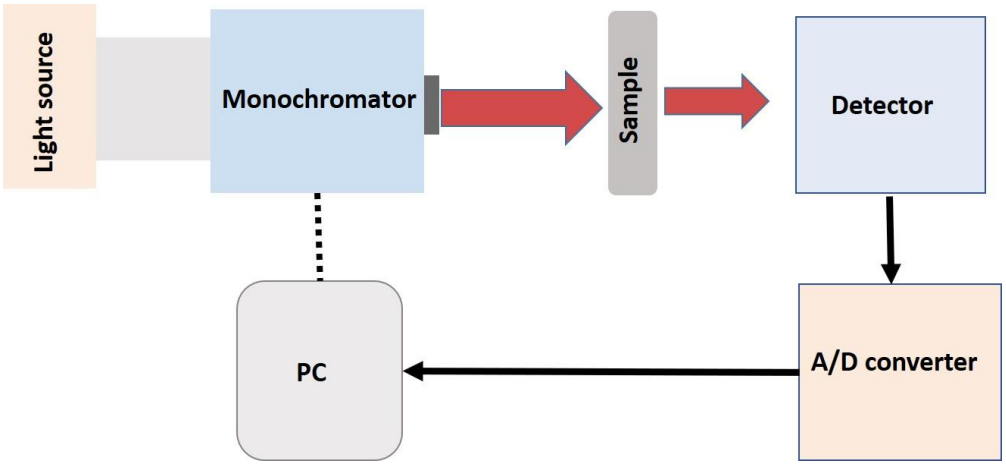

Fig.2.9 Schematic representation of experimental set up for optical absorption measurement with its essential components.

Working Principle

While traversing through the specimen, if the specimen absorbs light of certain wavelengths, the intensity of transmitted light reduces. The optical absorption spectrum of the sample is generated by plotting the transmitted intensity collected by the absorption spectrometer as a function of light wavelength. The relative intensity of the light beam after traversing the specimen of thickness 't' with respect to the intensity of radiation incident on the sample is related through the equation

$$I(\lambda)/I_0(\lambda) = \exp[-\alpha(\lambda)t] \qquad (2.3.1.1)$$

where, $I_0(\lambda)$ is the intensity of the incident radiation for a light of wavelength λ, $I(\lambda)$ is the intensity of the corresponding output beam, $\alpha(\lambda)$ is the wavelength-dependent material

absorption coefficient and t is the specimen thickness. The optical absorption coefficient of the material is more conveniently expressed in terms of optical density (OD), as given by

$$\alpha(\lambda) = 2.303 \times OD/t \qquad (2.3.1.2)$$

where, OD=log (I_0/I) by definition. The numerical value of OD=1 represents a 90% absorption and OD=2 corresponds to a 99% absorption. The absorption coefficient α(λ), which is independent of light intensity can be determined by measuring the sample thickness (t) and optical dentistry (OD) by the spectrophotometer. A typical absorption spectrophotometer, equipped with two separate chambers, one for the examined sample and the other for a reference specimen enables to filter out all other features of the sample (such as reflection from the sample surface) leading to reduction of the output intensity, other than the sample characteristic absorption. The optical bandgap of the sample material can be determined from the optical absorption spectral analysis which is related to the absorption coefficient α(λ) by the equation

$$\alpha h\nu = C(h\nu - E_g)^n \qquad (2.3.1.3)$$

where C is a frequency-independent proportionality constant, E_g is the optical band edge or bandgap of the sample material and n is a constant which determines the type of the optical transition. n=1/2 corresponds to direct allowed transitions and n=2 corresponds to indirect allowed transitions. The optical bandgap of tetragonal-phase-Ge nanocrystal related to direct allowed transition (n=1/2) has been determined from the $(\alpha h\nu)^2$ vs hν plots by using the extrapolation method.

2.3.2 Photoluminescence spectroscopy

Photoluminescence spectroscopy is an efficient nondestructive method to probe the electronic structure of materials as a macroscopic phenomenon. When an optically active material is excited by a photon with energy typically higher than the bandgap, it subsequently gives rise

to different luminescent transitions to the lower electronic levels in the form of a spectrum via radiative recombination. This is called photoluminescence. The electronic transitions can take place either through the inter-band fundamental gap or via different intermediate defect states as shown in Fig.2.10. The energy of the emitted light relates to the difference in energy levels between the two electronic states involved in the transition. The quantity of the emitted light is proportional to the population density of the carriers involved in the process. It is an important

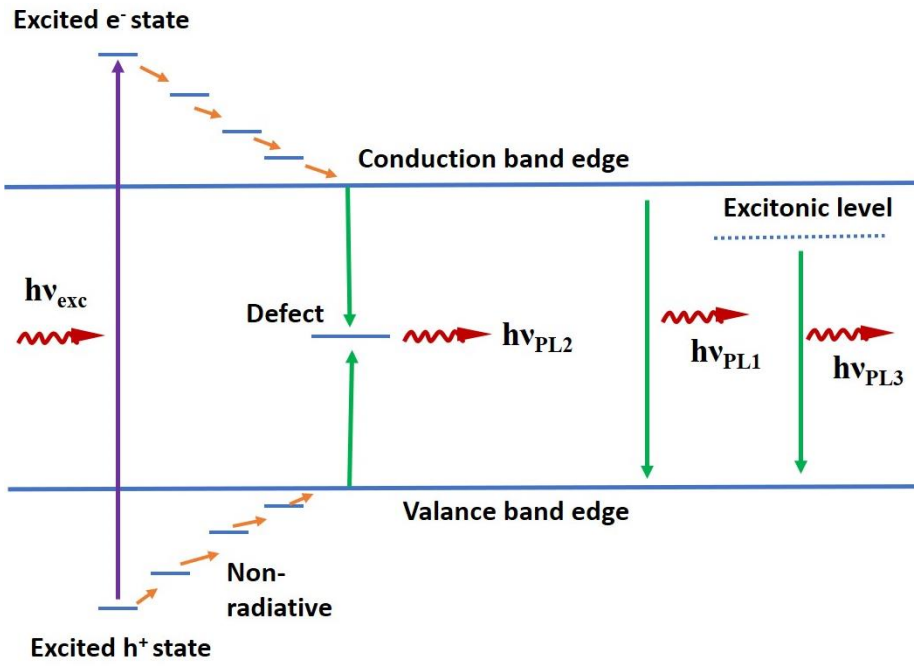

Fig.2.10 *Mechanism of Photoluminescence process mediated through different routes of radiative electronic transitions when excited by a photon of energy* $h\nu_{exc}$*. Photoluminescence is produced due to band-to-band electronic transition (*$h\nu_{PL1}$*), the electronic transition to some intermediated defect state (*$h\nu_{PL2}$*) or through the electronic transition between excitonic state and valance band edge (*$h\nu_{PL3}$*). The "hot' carriers are relaxed to the band edges through the continuum of states by the thermalization process in bulk material.*

optical characterization technique for the determination of bandgap, defect states, impurity concentration, recombination properties and crystalline quality of semiconductor materials, like GaAs, InAs, InP, and Ge. This is also a very useful technique to measure the exact chemical composition (x) of alloys like $In_xGa_{1-x}As$ and $Al_xGa_{1-x}As$ etc. The period between absorption and emission can be extremely short, it ranges from the femtosecond second-regime for the emission from free-carrier plasma in inorganic semiconductors up to milli-second for

phosphorescent processes in molecular systems. However, it can also be extended into minutes or hours under special circumstances. Photoluminescence is a three-step process

I. Generation of new electron-hole (e-h) pairs through absorption of the exciting radiation,
II. The electron-hole pairs recombine radiatively
III. Radiation escapes the sample in the form of photons

When a sample is illuminated by the excitation radiation, the generation of e-h pairs is limited within the diffusion length of excess carrier distribution which is so short that the PL signal coming out of the sample can be practically considered to be mostly contributed from the irradiated surfaces. Therefore, usual PL experiments are designed to collect the surface photoluminescence signal from the irradiated surfaces. Thin samples with reduced absorption cross-section for the recombination radiation also provides the provision of transmission photoluminescence [4]. Photoluminescence has direct applications in numerous light-emitting devices such as light diodes, semiconductor lasers, electroluminescent panels, and many others.

2.3.2.1 Radiative transitions

The emission of photoluminescence signal is mediated by the radiative transition between electronic levels. The PL intensity degrades due to the non-radiative recombination of carriers through the process of thermalization of ‘hot’ carriers. The different routes of radiative recombination leading to luminescence are as follows

(a) Process-1: Intraband transition.

(b) Process-2: Band-to-band transition.

(c) Process-3: Excitonic transition.

Different routes of radiative transitions among electronic states in bulk material are schematically depicted in Fig. Fig.2.10.

(a) Band to band transitions: The band–band recombination of an electron in the conduction band with a hole into the valence band leads to photoluminescence. The inter-band recombination is mediated by two different processes. In a direct bandgap semiconductor, electrons can make the direct optical transition between the bottom of the conduction band to the top of the valence band. Whereas, in an indirect bandgap semiconductor, this transition is only feasible with the assistance of a phonon [5]. Therefore, the probability of recombination is less in indirect bandgap semiconductor as compared to the direct bandgap semiconductors. The band–band recombination includes spontaneous emission, absorption and stimulated emission.

(b) Intra-band transitions: Relaxation of hot electrons by successive transitions through the energy states in a band can lead to photoluminescence.

In addition to that radiative transition is also mediated through shallow donor to valance band transition, conduction band to acceptor transition and shallow donor to shallow acceptor transition.

(c) Excitonic transitions

Exciton is a bound state of an electron and hole pair, bound by an electrostatic Coulomb force of attraction. It is an electrically neutral quasi-particle that exists in insulators, semiconductors and in some liquids [6]. An excitonic bound state is formed when the Coulombic attraction force between a photogenerated pair of electron and localized hole gives rise to an energetically stable configuration. Consequently, the exciton has slightly less energy than the unbound electron and hole. The decay of exciton by recombination of the electron and hole gives rise to PL signal which is limited by extended lifetime due to Resonance Stabilization [7].

There are mainly two types of excitons:

- Free excitons.
- Bound exciton

Free-exciton recombination: Radiative recombination of free exciton leads to PL signal. This is observed only at low temperatures in semiconductors having small exciton binding energies (such as in GaAs) whereas it is observed even at room temperature in semiconducting materials having large exciton binding energy.

Bound-Exciton Recombination: The recombination of excitons, localize at some potential fluctuations like QDs and QWs or impurities gives rise to PL signal. Excitons can be bound to neutral or ionized impurities (donors and acceptors).

2.3.2.2 Low-temperature PL set-up

The experimental low-temperature PL set-up is described by a schematic, as shown in Fig.2.11. Typically, the experimental arrangement contains the following components.

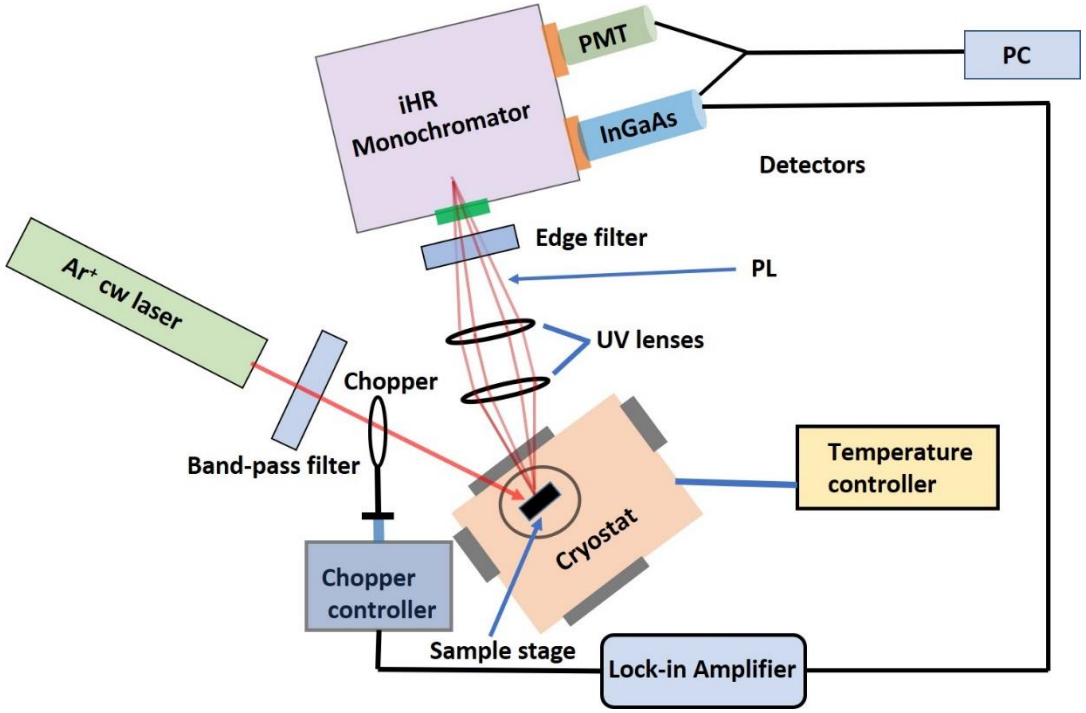

Fig.2.11 Schematic representation of photoluminescence laboratory set up with temperature control unit.

(a) Excitation source: An Ar^+ laser with variable excitation power and tuneable operating wavelength in the range 488 nm to 514 nm has been employed as the excitation source. The laser beam is linearly polarized with a measured beam diameter of 2 mm on the sample surface.

Band-pass filter: Band-pass filter of 488 nm and 514 nm were employed to cut off other laser lines illuminating the sample.

(b) Beam attenuator: A series of glass slides were mounted in the path of the incident beam to cut down the beam intensity.

(c) Sample stage: A sample holder equipped with an X-Y-Z translation stage is used to mount the sample.

(d) Collection optical system: Set of two convex lenses of the focal length of 40 nm and 60 nm are placed in front of the sample to collect the resulting PL emission from the sample and couple it to the spectrometer. The focused PL signal is taken through an edge filter of 488 nm and 514 nm respectively before the beam enters into the spectrometer chamber. The edge filters eliminate all the wavelengths from the collected PL signal below 488 nm and 514 nm respectively.

(e) Spectrometer: A Horiba Jobin Yvon iHR-550 series triple grating spectrometer has been used here with a focal length of 550 nm (f/6.4 aperture). The gratings are characterized by 1200 gr/mm with a spatial resolution of 0.025 nm. The collected PL signal is spectrally dispersed by the gratings which are subsequently fed into the detector system. The spectrometer is equipped with two detectors which can detect wavelengths in the spectral range from 150 nm to 1500 nm. A photomultiplier tube (PMT) detector is employed for the detection of wavelength in the range of 185-900 nm. For detection of wavelength in the infrared (IR) range from 800-1500 nm, a thermionically cooled InGaAs detector is used in conjugation with a lock-in amplifier and a chopper. The signals produced by the detectors are recorded and analyzed by a computer system.

For low temperature (up to 3.4 K) PL measurements, the examined specimen is mounted inside a closed cycle He cryostat (Janis Research Co. Inc., SHI- 4). There is a provision to control the

temperature of the sample from 3.4 K to room temperature by using a tiny heat pump. The resulting low-temperature luminescence is then coupled to the spectrometer through a system of converging lenses and analyzed by the detectors.

2.4 Device characterization of electro-optic properties

Different experimental techniques, like photocurrent and dark current measurement, I-V characteristic and temporal photo-response have been employed to characterize the quantum dot infrared photodetector (QDIP) device performance over a range of temperature and bias voltage. Before characterization, metallic contacts were grown over the sample by Thermal evaporation technique which is commonly used for thin-film deposition. The contacts are grown by suitably musking the sample surface. The detail of the deposition technique is also discussed in the following sub-section.

2.4.1 Growth by Thermal evaporation technique

Thermal evaporation (TE) is one kind of physical vapor deposition (PVD) technique where the material to be deposited is melted and evaporated by means of heating. This is basically a thin film deposition technique performed in the presence of a vacuum (residual pressure ~10^{-6} mbar). Typically, the air pressure of the chamber during evaporation is maintained around 10^{-6} mbar. For this process, the material to be deposited is placed in a crucible and heated to its characteristic temperature of vaporization through the Joule heating effect of a filament (mainly of tungsten). The evaporated stream of vapor from the material easily get transported through the vacuum and finally condense into a thin layer onto a substrate. We have employed TE for the growth of the top contacts of Au and alloyed Au-Ge metal on the InAs/GaAs quantum dot-based heterostructure by using proper masks. The following subsections contain a brief discussion on the experimental setup for the thermal evaporation technique.

2.4.1.1 Experimental setup for Thermal evaporation technique

The experimental setup for the TE technique is schematically depicted in Fig. 2.12. The essential components are the following:

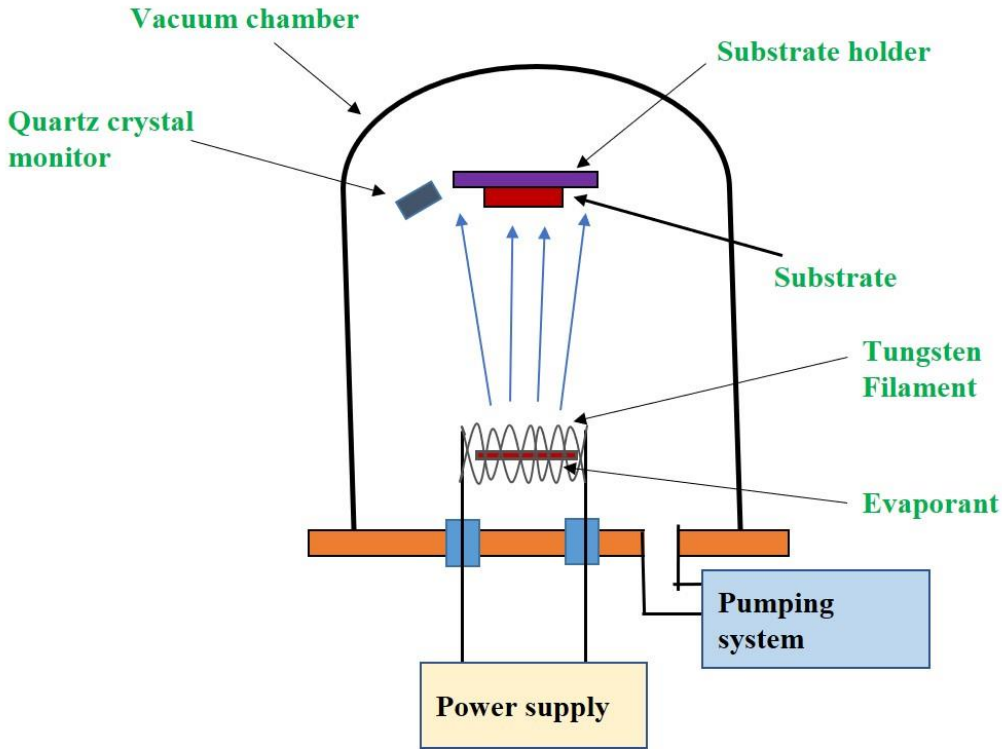

Fig. 2.12 Schematic representation for the experimental set up of thermal evaporation technique.

Crucible: The material for thin film deposition is taken inside a crucible which is subsequently heated. The crucibles are usually made with materials such as tungsten, molybdenum, or tantalum, having a very high melting point and very low vapor pressure. The shape of the crucibles used is in the form of a coil. Their endpoints are directly connected to the heavy copper or stainless-steel electrodes for the completion of the electrical circuit. In our case, we have used tungsten crucible during contact growth.

Tungsten Filament: The material inside the crucible is heated through the Joule heating effect of a filament made of tungsten.

Vacuum Pump: A turbopump in conjugation with an oil pump (a rotary pump can also be used) is used to reach an overall vacuum level of 10^{-6} mbar and sustain it for the deposition.

Substrate Holder: A metal plate is used for holding the substrate.

Heater: To heat the sample for the deposition of thin-film at high temperature. The maximum achievable temperature is 400^{o} C. It is attached to the substrate holder.

Quartz Crystal Monitor: For measuring the thickness and growth profile of the grown material.

2.4.2 Photo-current measurement

Photo-current spectroscopy is a routine characterization technique for measuring the photocurrent in the form of a spectrum, generated through the absorption of monochromatic radiation over a certain range of frequencies. The motion of photo-generated electron-hole pairs driven by the device built-in electric field towards the metallic contacts grown on the semiconductor sample gives rise to the spectral photocurrent. The device parameter, spectral photo-responsivity of a specimen is defined as

$$R_\lambda = I_\lambda / P_\lambda \qquad (2.4.2.1)$$

where I_λ is the wavelength-dependent photogenerated current and P_λ is the spectral power of the incident radiation. The external quantum efficiency or quantum yield is defined as

$$EQE = R_\lambda hc / \lambda q \qquad (2.4.2.2)$$

Where λ is the wavelength of the incident photon, h is the Planck's constant and q is the electronic charge. The peak wavelength corresponding to the maximum of the spectral photo-response, provide information about different energy gaps in quantum dot confined structure.

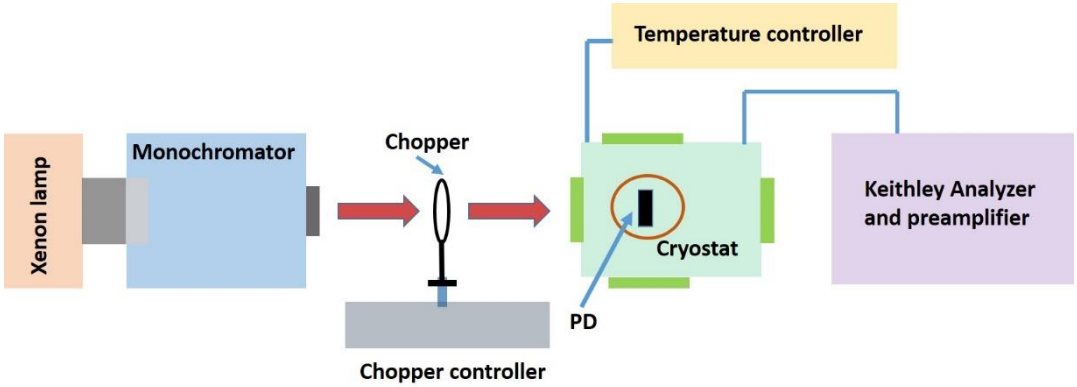

Fig.2.13 *Schematic representation of a complete experimental unit for photocurrent measurement.*

Photo-current measurements of the quantum dot structures were carried out by using a 450W xenon lamp excitation source with tuneable wavelength covering a spectral range from 150 nm to 1000 nm. The experimental set-up with its components is schematically shown in Fig.2.13.

The sample, mounted on a probe holder is illuminated by monochromatic light. The light from the xenon lamp has been dispersed through 0.3-m Gemini-180 monochromator and directed towards the sample surface via a band-pass filter and a series of mirrors and lenses. The resulting PC in the sample has been collected via two metal contacts grown on the sample and then amplified and analyzed in a Keithley 4200 SCS source meter in conjugation with a preamplifier. PC measurements were performed as a function of applied bias voltage in the form of I-V characteristic to evaluate the dependence of the electric field on photo-response.

2.4.3 Temporal photo-response

There is also a provision of temporal measurement of the photo-response of the QDIPs. For temporal measurement, an optical pulse of desirable frequency is generated through powering a laser by an ultrafast function generator. The photo-response of the device is registered by additionally employing a Tektronix TBS2102 digital storage oscilloscope (DSO). The corresponding experimental arrangement is shown in Fig.2.14.

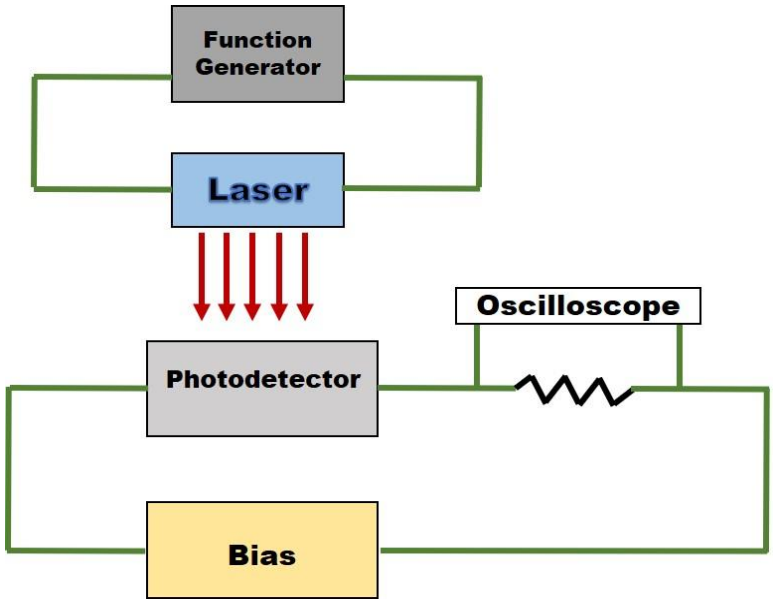

Fig. 2.14 circuit diagram for the measurement of the temporal response of the photodetector.

2.4.4 Dark current measurement

I-V characteristic at a fixed temperature and temperature dependence of injection current at a fixed bias are performed under 'no light' condition with the same set up as discussed above. For noise current measurement under dark condition, an SR-830 lock-in amplifier has been installed to measure the noise power density throughout the operating temperature range.

2.5 Bibliography

[1] W. I. Park, D. H. Kim, S.-W. Jung, and G. C. Yi, Appl. Phys. Lett. **80** (2002) 4232.

[2] S. Amelinckx, D. van Dyck, J. van Landuyt and G. van Tendeloo, editor, Electron Microscopy: Principles and Fundamentals, VCH (1997).

[3] N. Yao and Z. L. Wang, editor. Handbook of microscopy for nanotechnology Kluwer Academic Publishers, 2005.

[4] R. K. Willardson and Albert C. Beer, Semiconductors and semi-metals, vol-8.

[5] S. Doniach and M. Sunjic, J. Phys. C **431** (1970) 285.

[6] Liang, W Y, "Excitons". Physics Education **5 (4)** (1970) 226.

[7] Y. Frenkel, Phys. Rev. **37** (1931) 17.

Chapter 3

Structural and optical characterization of phase selectively grown Ge nanocrystalline thin films

3.1 Introduction

Out of two phases of Ge, viz., the cubic and the tetragonal (ST-12), the latter one is demanding for high gain optoelectronic applications due to its high direct bandgap. Unfortunately, Ge is usually found in a diamond-like cubic phase in nature. However, the ST-12 structure can be realized if the Ge crystallites are grown in a sufficiently small size. We have categorically shown the feasibility to attain a predominantly selective yield of the tetragonal phase by tuning the growth of Ge nanocrystals (NCs) by varying the kinetic energy of the impingent beam of Ge clusters on substrates. A set of Ge nanocrystalline thin films have been grown in an ionized cluster beam deposition (ICB) chamber. The generated clusters were ionized in the chamber, cooled in the second zone and then accelerated in the potential range of 0-2.5 kV. Thus, the Ge clusters were made to impinge on substrates at different kinetic energies. The corresponding structural and optical properties and the possibility of tuning the emission energy are studied as a function of cluster beam energy. These results are discussed in great detail in this chapter.

3.2 Phase selective growth Ge-NC thin films by ICB deposition

3.2.1 Basics of ICB deposition technique

Ionized cluster beam deposition (ICB) is a useful growth technique, typically employed to grow nanocrystalline thin films where an adiabatically cooled stream of ionized clusters in the vapor phase is accelerated through a high potential to impinge on a substrate and nucleate into nanocrystals of the cluster material. The components of a modern ICB system are schematically shown in Fig.3.1. A set of Ge nanocrystalline thin films have been grown on a quartz substrate by using both neutral and ionized beam of supercooled Ge clusters in ICB deposition chamber.

3.2.2 Laboratory growth of Ge-NC

A small amount of Ge powder, loaded inside a cylindrical graphite crucible of length 14 mm, thickness 1 mm and diameter 8 mm is directly vaporized by heating it up to 1700 K through a

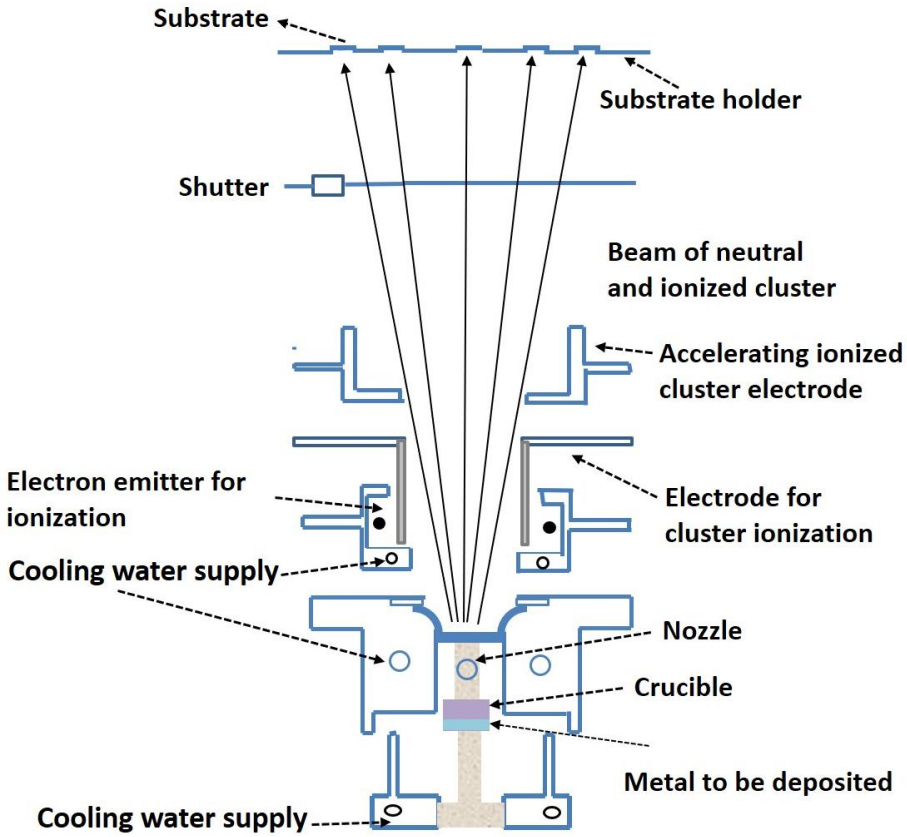

Fig.3.1 Schematic representation of different parts of the ICB deposition system.

winded resistive coil. A high purity (99.998%) supersonic jet of Ge atoms in the vapor phase is made to be ejected from the higher-pressure zone into a relatively lower pressure vacuum (~10^{-6} Torr) chamber through a constricted nozzle of diameter 0.5 mm. This conveys adiabatic expansion of the Ge vapor and subsequent rapid cooling of the Ge atoms combining into large size material clusters (~10^2-10^3 atoms). The fast-moving stream of Ge clusters was directed towards a quartz substrate, maintained at liquid nitrogen temperature (LNT). The substrate was kept 130 mm apart from the crucible. The clusters impinge on the substrate surface and nucleate into Ge nanocrystals. The size of the grown nano-crystallites may be different owing to different impinging kinetic energy which can be externally controlled by ionizing the cluster beam and subjecting to pass through different accelerating potential. The neutral beam directly impinges on the substrate surface with the minimum kinetic energy to form Ge-nanocrystalline thin film (Film 1). To produce the ionized beam, Ge clusters were partly ionized through

electron impact under constant ionization current. Then the beam of ionized clusters was subjected to different accelerating potential (1.5 kV and 2.5 kV) which consequently impinge on the substrate with different kinetic energy to form Ge-nanocrystalline films (Film 2-3). The rate of growth was maintained at 0.03 nm/sec through monitoring by a crystal oscillator. The crucible and substrate were kept apart by a distance of 120 mm. The growth rate was monitored by a crystal oscillator and was kept constant at ~0.03 nm/s.

3.3 Structural and optical characterization of Ge-NC thin films

For characterization and measurement of the structural and optical properties as a function of cluster beam energy, three sets of Ge nanocrystalline films have been grown, corresponding to the neutral beam (Film-1) and ion beam subjected to 1.5 kV (Film-2) and 2.5 kV (Film-3) respectively.

3.3.1 Phase and nano-crystallite size determination from Raman spectroscopic measurement

The Raman spectra corresponding to the three films are depicted in Fig.3.2. Evidently, in addition to a phonon peak at ~300 cm^{-1}, another broadened TO-like Raman peak has appeared

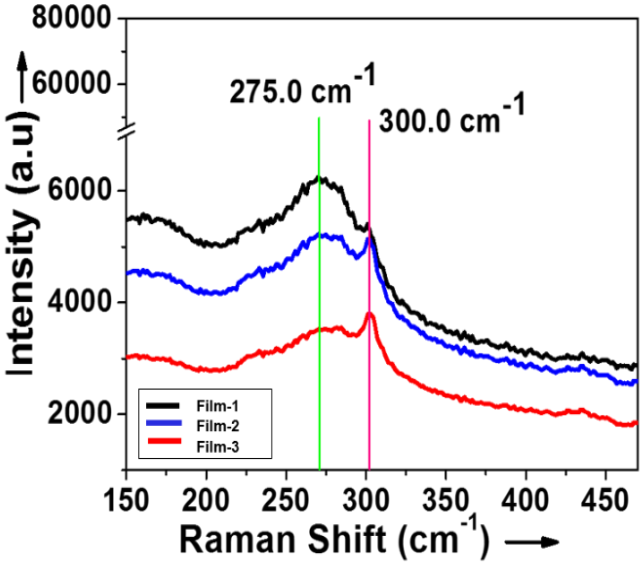

Fig.3.2 *Comparative Raman spectra of the films deposited using neutral Ge clusters (Film-1) and using ionized Ge clusters (Film-2 and Film-3) under accelerating potentials of 1.5 and 2.5 kV respectively.*

in all three spectra. The phonon peak fixed at ~300 cm^{-1} for all three samples is associated with Raman scattering from bulk regular cubical diamond-like Ge crystallite structures (Γ_{25}) [1]. The monotonic Raman redshift of the broadened lower energy TO-like Raman peak from 282 cm^{-1} to 275 cm^{-1} with decreasing cluster beam kinetic energy (2.5 kV-0 kV) suggests progressively stronger confinement-induced phonon interaction with grain boundaries inside Ge nano-crystallites [2]. The asymmetric TO-phonon response has been deconvoluted by using the standard phonon confinement model. This is an indication of the emergence of another Ge phase coexisting with the normal diamond-like structure with a comparatively smaller crystallite size. Further, redshift in Raman peak energy associated with the new phase with decreasing the beam accelerating potential (V_B~2.5 kV-0 kV) suggests a reduction in the average nano-crystallite size. The Ge-nanocrystalline film corresponding to neutral clusters has exhibited the maximum Raman redshift to ~275 cm^{-1}. From the respective shift in phonon energy, the average crystallite size associated with the second more compressed Ge-phase has been deduced to be ~ 7 nm, 10 nm and 15 nm for Film-1, Film-2 and Film-3 respectively [3-4]. One can also notice that the ratio of scattered intensity related to the broadened red-shifted peak to the normal cubical Ge-related peak (~300 cm^{-1}) increases with increasing the beam energy and becomes maximum and greater than unity for the Film-1 (neutral cluster). This suggests the progressive increment of the relative proportion of the compressed second phase of germanium as compared to the normal cubical Ge phase with increasing the cluster beam impinging kinetic energy.

3.3.2 High-resolution TEM analysis: Crystallographic measurements

The relative crystallinity study of both the co-existing Ge phases for different beam energy has been carried out through the high-resolution transmission electron microscopic (HRTEM) images and selected area electron diffraction (SAED) pattern of Film-1 and Film-2, as shown in Fig.3.3 (a)-(d). The lattice fringes are highlighted by encircled regions in the respective TEM

images. The short-range orientation of lattice fringes along different directions is much more prominent in Film-2 as compared to the Film-1 (neutral cluster), as depicted in respective HR-TEM images. The average value of crystallite size has been measured to ~ 7 nm and ~11 nm for Film-1 and Film-2 which quite closely agrees with their values as deduced from Raman measurements. The information of lattice plane spacings has been determined from the radii of the observed rings in respective SAED patterns. For Film-2, related to a beam energy of 2.5 kV, the determined lattice plane spacings (d_{hkl}) are 0.3267 nm, 0.2 nm, 0.1705 nm, and 0.1298

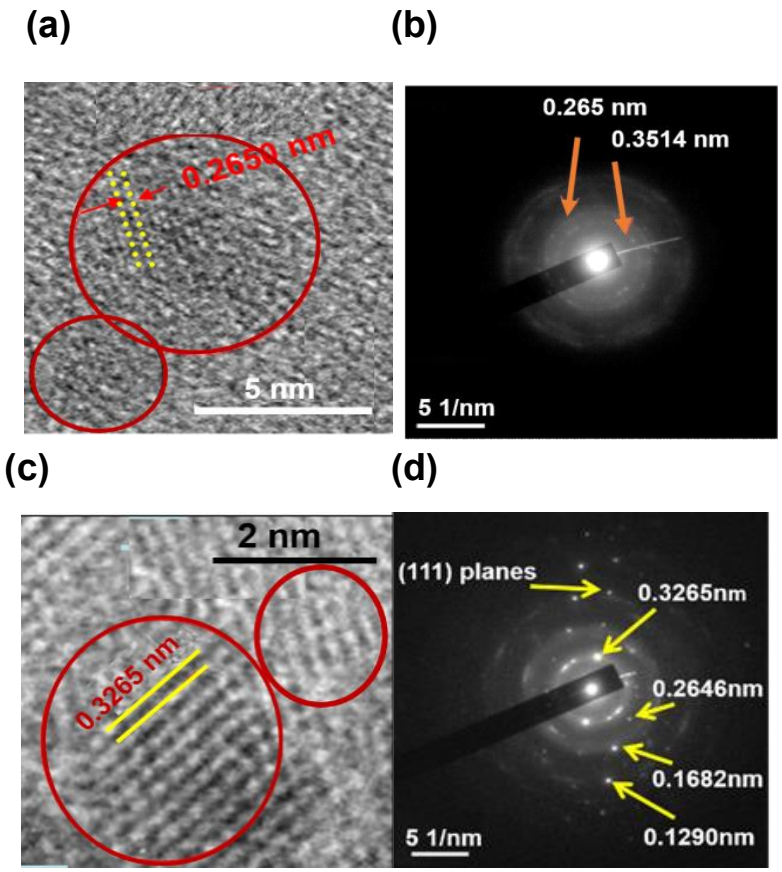

Fig.3.3 *(a,c) Cross-sectional HRTEM image and (b,d) the SAED pattern for the Ge-nanocrystalline Film-1 and Film-2. Short-range crystallographic orientations in different directions are much more prominent in Film-2 than Film-1 as represented by encircled regions.*

nm corresponding to (111), (311) and (331) lattice planes of diamond-like cubical crystal structure [5]. On the other hand, the SAED pattern (Fig.3.3 (b)) for neutral cluster Film-1 gives the impression of (111) and (210) lattice planes with determined d_{hkl} values of 0.3514 nm and 0.265 nm. This corresponds to some close-packed tetragonal crystal structure (ST-12) [6-8].

From this, it can be apparently inferred that the second phase of Ge is metastable tetragonal ST-12 structure, whose abundance relative to the normal bulk cubic Ge phase increases with decreasing the cluster beam energy. The higher relative abundance of smaller size compressed tetragonal nano-crystallites reduces the polycrystallinity of the grown films.

Discussion

Ge usually crystallizes in the normal low-pressure cubic diamond-like structure. But while depositing Ge-nanocrystals (NC) in the form of impinging clusters, the large lattice misfit between Ge and the substrate material induces high compressive stress upon the grown Ge-layers [10]. For a certain minimum critical size of the grown Ge-NC, this excess strain energy is released while permanently transforming the cubical Ge phase to smaller crystallite size tetragonal phase which subsequently crystallizes in that form [11]. The phase transformation from cubic to tetragonal Ge phase is most prominent for neutral beam Ge clusters with minimum kinetic energy. With successively higher energy charged cluster beam, resulting in greater average kinetic energy of the Ge adatoms reduce the effect of strain compression and offer stronger cohesive interaction with the adjacent NCs. This greater degree of Ge adatom migration offers coagulation of Ge-clusters in bigger NCs consisting of the normal bulk cubical structure without giving rise to any phase transformation.

3.4 Optical characterization of the Ge-NC thin films

3.4.1 Optical absorption spectra: Determination of bandgap energy

To investigate the optical properties of the Ge-nanocrystalline thin films due to the presence of different relative proportions of individual phases, the optical absorption spectra for the three films are analysed. The respective optical absorption coefficient α is plotted with irradiating photon wavelength, as depicted in Fig.3.4. The optical bandgap or equivalently the absorption band edge for different cluster deposited Ge thin films has been deduced from the individual

$(\alpha h\nu)^2$ vs $h\nu$ plot, as shown in the *inset* of Fig.3.4. The evaluated absorption band edges are 1.75 eV, 1.60 eV and 1.55 eV for the Film-1, Film-2 and Film-3 respectively. Evidently, with decreasing Ge-cluster beam energy, the optical bandgap associated with the grown Ge nano-crystalline thin film blueshifts to progressively higher values with respect to bulk Ge bandgap energy. The monotonic rise in bandgap energy for the Ge thin films possessing a higher concentration of tetragonal (ST-12) phase, apparently indicates characteristically higher bandgap for tetragonal Ge structure as compared to the bulk normal cubical structure. The

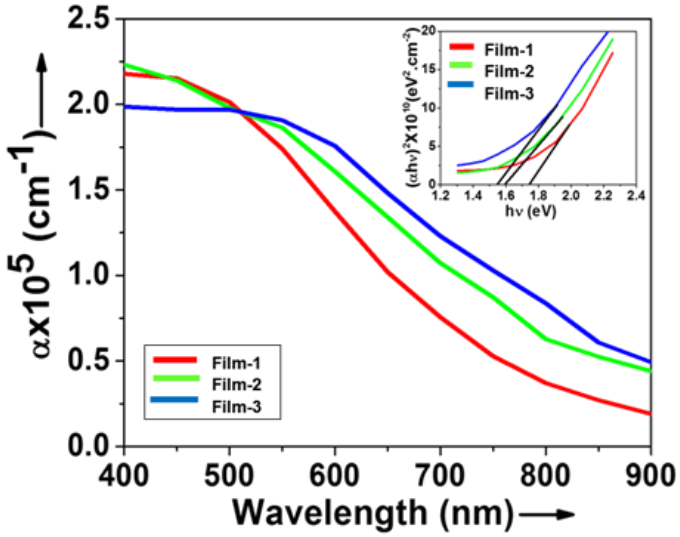

Fig3.4 *Optical absorption spectra of Ge-NC films with different relative abundance of cubic and tetragonal phase.* ***Inset:*** *Plot of $(\alpha h\nu)^2$ vs hν. From the intersections of the dotted lines with the energy axis, approximate values of optical gaps have been determined to be 1.75 eV, 1.60 eV and 1.55 eV for Film-1, Film-2 and Film-3 respectively.*

carrier confinement originated quantum size effect due to decreasing nano-crystallite size has also played a contributory role for widening the bandgap [9].

3.5 Photo-oxidation study of the tetragonal Ge phase

To quantitatively study the effect of oxidization under UV exposure upon the tetragonal Ge phase, the neutral cluster Film-1, with the greatest relative abundance of tetragonal phase, has been photo-oxidized and subsequently characterized. The measurements have been carried out

with the thin films irradiated by constant UV exposure of 30 min and 45 min and compared with the untreated as-grown neutral film (Film-1).

3.5.1 Optical absorption analysis of the photo-oxidized films

The optical bandgap of the photo-oxidized Ge-nanocrystalline films has been deduced from the $(\alpha h\nu)^2$ vs $h\nu$ plots extracted from individual optical absorption spectra, as shown in Fig.3.5. The optical bandgap for 30 min and 45 min photo-oxidized Ge thin films have been deduced to be ~ 2 eV and 2.5 eV along with ~1.75 eV for the untreated neutral Film-1. Evidently, the optical gap progressively increases with increasing photo-exposure time or equivalently with increasing thickness of the GeO_x oxide layer upon the Ge-NCs. The blueshift in the optical gap can be attributed to two different factors. Firstly, stronger quantum confinement effect with the shrinkage of Ge-NC cores under the progressively thick GeO_x layers may have led to a rise in bandgap energy [12-13]. Secondly, monotonically increasing thickness of the grown GeO_x

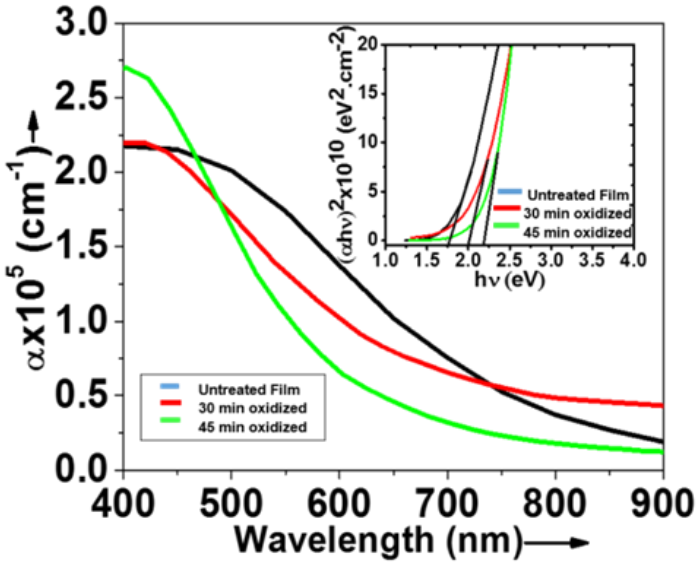

Fig.3.5 Optical absorption spectra of the neutral film under three different environments: as-grown, 30 minute photo-oxidized and 45 minute photo-oxidized. ***Inset:*** *Plot of $(\alpha h\upsilon)^2$ vs $h\upsilon$ from where the absorption band edge has been estimated to be ~1.75 eV, ~2 eV and ~2.25 eV under afore-mentioned conditions.*

layer with increasing time of photo-oxidation also offers conversion of a greater number of Ge-

Ge bonds into Ge-O-Ge bonds which can essentially give rise to enhancement in NC's bandgap [1,14].

3.5.2 Room temperature PL analysis

To analyse the effect of photo-oxidation upon the light emission properties of the Ge-NCs enriched in high energy tetragonal phase, room temperature (RT) photoluminescence (PL) spectra for the as-grown untreated (neutral) Film-1 and the 30 min-photo-oxidized film are

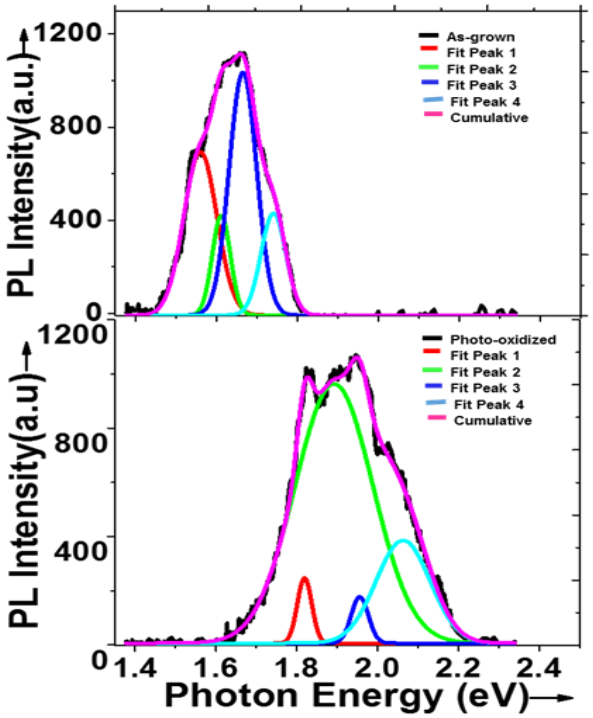

Fig.3.6 Room temperature PL spectra of Film-1 in two different condition: as-grown (top) and 30 mins photo-oxidized (bottom). The experimental data are de-convoluted (black lines) by the multiple peak Gaussian line shapes (colored lines).

recorded, as depicted in Fig.3.6 (a)-(b). For that purpose, all the samples are excited by 514 nm Ar^+ laser. Multi peak PL spectra have been properly de-convoluted by using standard Gaussian fitting function. The emission energies corresponding to the two of the multi-PL peaks that appeared in the RT-PL spectra for the as-grown film have been found to be ~ 1.7 eV and ~2.06 eV. The measured PL peak energy of ~1.7 eV is in good agreement with the deduced absorption band edge from optical absorption spectra. These PL peaks are attributed to electron-hole inter-band transition in Ge. But for the 30-min-photo-oxidized Ge film, these peaks are rather

suppressed by other stronger blue-shifted luminescence signal peaking at ~1.82-1.95 eV [15]. The multi-peak PL profile may have been originated from radiative transitions between different ground and excited excitonic states of Ge-NC thin films at room temperature. The most intense PL peak is related to the ground state excitonic transition of Ge ST-12 phase which has been considered as the PL peak energy in the thesis. The feeble lower energy peak at ~1.5 eV is related to bandgap transition of lower concentration diamond-like Ge phase. The other higher energy peak of as-grown Ge-NC film is associated to radiative transition related to the excited states. The suppression is more prominent for the photo-oxidized film as compared to the as-grown neutral film. These intense PL peaks are ascribed to bound excitonic transitions from Ge-NCs emitting in visible range [16]. With increasing degree of carrier confinement under a thicker layer of GeO_x the strength of these excitonic transitions is further enhanced as compared to the electron-hole pair inter-band recombination [17-18]. The consequent carrier confinement inside compressed NC cores under GeO_x cover leads to the blueshift in the resulting PL peak energy by 300 meV from the peak energy of the as-grown film [15,]. The compressed Ge-NC cores in photo-oxidized Ge thin films thus resembles some quantum dot structure [19]. Increment of observed PL bandwidth for the photo-oxidized Ge film as compared to as-grown film is an indication of enhanced quantum dot size dispersion as a result of photo-oxidation. The GeO_x oxide layers also give rise to PL signal ~3.1 eV [20]. The effect of increasing oxygen composition (x) in GeO_x with increasing degree of oxidation increases the bandgap of GeO_x leading to blueshift of its bandgap related PL peak energy. But nevertheless, that is well beyond the range of our PL scanning energy.

3.5.3 Determination of Ge oxidation states from XPS study

To analyse different oxidation states of the tetragonal Ge-structures, X-ray photoelectron spectroscopic (XPS) measurement of the neutral cluster Ge-nanocrystalline thin film (Film-1) has been performed by employing using Al-K_α x-ray source of energy 1486.6 eV. XPS spectra

have been observed to study the oxidation states of Ge-NC subjected to three different environments: as-grown un-treated air-exposed neutral film (Film-1), UV excited photo-oxidized film and aqueous HF treated film. Aqueous HF solution has been employed to remove the oxide layer from Ge-NCs. The corresponding XPS spectra are depicted in Fig.3.7. Each spectrum has exhibited two pronounced XPS peaks at ~ 29.3 eV and ~ 32 eV associated with Ge-3d core electrons and surface sub-oxides of GeO_x. The peaks are properly de-convoluted, as depicted in the *inset* of Fig.3.7. Evidently, the air-exposed as-grown Ge film has exhibited an oxide-related peak at ~ 31.8 eV along with a chemical shift of 2.5 eV. This is associated with Ge^{3+} oxidation state. For the UV-exited photo-oxidized Ge thin film, the oxide-related peak has shifted to ~ 32.6 eV, along with a chemical shift of 3.3 eV. This is associated with the Ge^{4+} oxidation state [21]. The HF-treated Ge thin film, exhibits a much weaker oxide related peak, owing to the chemical removal of the grown oxide GeO_x layers by this treatment.

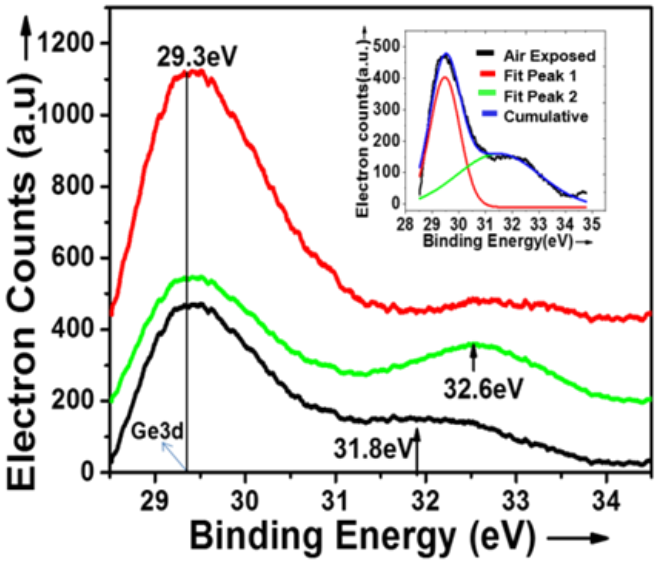

Fig.3.7 *XPS spectra of the neutral film (Film-1) under three different environments: air exposed (Black), UV photo-oxidized (Green) and aqueous HF solution (Red).* ***Inset:*** *De-convoluted XPS peaks of the air-exposed film.*

3.6 Conclusion

We have studied the feasibility of growing Ge nanocrystal with a selective yield of specific Ge phase by externally controlling the energy of the cluster beam in the ionized cluster beam deposition chamber. Through this work, we have shown a substantial amount of novel Ge tetragonal phase can be attained while suppressing the growth of the normal cubic phase by tuning the energy of impingent Ge clusters. Through adequate structural and optical analysis, it has been observed that the relative abundance of the tetragonal phase can be significantly enhanced by decreasing the kinetic energy of the bombarding cluster beam. The relative proportion of the Ge tetragonal phase is maximum in the neutral cluster film. While decreasing the beam energy, below a certain threshold value of NC's size, the normal cubical phase transforms itself into a more compressed high energy tetragonal phase. This also offers tuning of emission energy in the visible range. By using high bandgap tetragonal Ge phase, an intense sharp blue-shifted visible photoluminescence has been achieved at room temperature which offers the provision for visible light-emitting optoelectronic device application operating at room temperature. We further have studied the provision for controlled photo-oxidation of Ge thin films enriched in the tetragonal phase. In this way, it has been possible to further tune the luminescence to green color (~550 nm) while decreasing the effective size of the NC cores under oxide cover.

3.7 Bibliography

[1] Sato, S. Nozaki and H. Morisaki, J. Appl. Phys. **81** (1997) 1518.

[2] R. J. Kobliska, Phys. Rev. Lett. **29** (1972) 725.

[3] Y. Batra, D. Kabiraj and D. Kanjilal Solid State Commun. **143** (2007) 213.

[4] H. Campbell, P. M. Fauchet, Solid State Commun. **58** (1986) 739.

[5] Y. Saito, J. Cryst. Growth **47** (1979) 61.

[6] J. Jiang, K. Chen, X. Huang, Z. Li, D. Feng, Appl. Phys. Lett. **65** (1994) 1799.

[7] Dana, S. Agan, S. Tokay, A. Aydmh and G. Finstad, Phys. Status Solidi. **4** (2007) 288.

[8] J. S. Kasper, S. M. Richards, Acta Crystallogr. **17** (1964) 752.

[9] E. B. Gorokhov, V. A. Volodin, and D. V. Marin, Semiconductors **39** (2005) 1168.

[10] J. Diao, K. Gal and M. L. Dunn, Nat Mater **2** (2003) 656.

[11] S. J. Kim, O. Quy,L. Chang, E. Stach, C. A. Handwerker and A. Wei, J. Mater. Chem **20** (2010**)** 331.

[12] G. Wilfried, H. van Sark, Patrick Frederix, Dave Van den Heuvel, Hans Gerritsen, Ageeth Bol, Joost van Lingen, Celso de Mello Donegá and A. Meijerink, J. Phys. Chem. B **105** (2001**)** 8281.

[13] S. Sato, S. Nozaki, H. Morisaki and M. Iwase, Appl. Phys. Lett. **66** (1995) 3176.

[14] G. Armatas and M. Kanatzidis, Nature (London, U. K.) **441** (2006) 1122.

[15] Y. Kanemitsu, H. Uto and Y. Masumoto, Y. Maeda, Appl. Phys. Lett. **61** (1992) 2187.

[16] G. Dukovic, F. Wang, D. Song, Matthew Y. Sfeir, Tony F. Heinz and Louis Brus, Nano. Lett. **5** (2005) 2314.

[17] X. Shi, S. Zheng, W. Gao, W. Wei, M. Chen, F. Deng, J. Nanopart. Res. **16** (2014) 2741.

[18] Steinhoff, J. H. Kim, F. Jahnke, M. Rosner, D. S. Kim, C. Lee, G. H. Han, M. S. Jeong, T. O. Wehling and C. Gies, Nano Lett. **15** (2015) 6841.

[19] S. Koch, W Kira, G. Khitrova and H. M. Gibbs, Nat. Mater. **5** (2006) 523.

[20] M. Zarachias and P. M. Fauchet, Appl. Phys. Lett.**71** (1997) 380.

[21] H. Adhikary, P. Mclntyre, S. Sun, P. Pianetta and C. Christopher, Appl. Phys. Lett. **87** (2005), 263109.

Chapter 4

MBE growth of self-assembled InAs/GaAs quantum dots

4.1 Basics of Molecular Beam Epitaxy (MBE)

Epitaxial growth refers to an ordered layer-by-layer growth of a crystal on some well-defined crystalline substrate with the growing layer having a definitive crystallographic relation with the substrate. The successively grown layers follow the in-plane crystal structure of the underlying epilayer. Crystalline films can be grown on a substrate having the same lattice constant by the process of homo-epitaxy whereas the growth of epilayer on a lattice-mismatched substrate is called the hetero-epitaxy. Molecular beam epitaxy is an ultra-high vacuum process which provides the possibility to prepare such epitaxially grown high-quality complex multilayers with abrupt interfaces for a wide range of Gr IV and III-V semiconductor materials [1]. This offers precise control over the composition and thickness of the grown thin film up to atomic level accuracy [2-3].

MBE technique has been first introduced in Bell Laboratories, USA in the early 1970s. The growth process essentially consists of the deposition of atomic or molecular beams on a single-crystal substrate inside an ultra-high vacuum chamber (UHV) with a residual pressure of 10^{-9}-10^{-10} Torr. The source materials, either in liquid or solid form are evaporated or sublimated in an effusion cell equipped with computer-controlled exit shutters. The well-directed stream of thermal atoms or molecules issued from the effusion cell impinges onto a single-crystal substrate, conveniently heated to an elevated temperature. The arriving stream of particles gets adsorbed on the substrate surface. The adsorbed entities with sufficient thermal energy start to migrate all over the substrate surface to adopt the crystallographic orientation of the substrate and complete the layer growth with adsorbents sitting in the adequate lattice sites. The elevated substrate temperature helps to serve enough kinetic energy to the adatoms to migrate over the surface to those lattice sites. But a higher substrate temperature also leads to some degree of interfacial diffusion and desorption from the surface. Therefore, optimization is done by usually setting the temperature to a moderate value. The nearly collision-free motion of the

impinging atoms through the UHV helps to achieve uniform beam flux over the substate. The presence of UHV and a fast switching shutter make it possible to grow a film of pristine quality with a provision of changing the composition of the impinging flux quite abruptly. More interestingly, the composition of the beam flux can be changed within a time scale much shorter than the time it would require to grow a single atomic layer of the film. This offers a huge potentiality of crystal growth by tailoring composition and impurity level layer-by-layer in the MBE technique. Usually, layer by layer growth at the atomic scale is obtained at a typical rate of 0.1-1 μm/h by deliberately employing a low flux beam.

4.2 Details of the setup

The (Riber Epineat III-V) MBE system at nanofabrication Facility (NF), IIT Bombay is specially designed to grow As-based compound semiconductor crystal. The system consists of three main pump-controlled inter-locked vacuum chambers: a growth chamber, a load lock, and a buffer chamber, as shown in Fig.4.1. The load lock is used to bring samples in and out of the vacuum environment while restoring the vacuum integrity of the rest of the chambers. This is employed to achieve greater material throughput in which one or more substrate is loaded without exposing the outgassed constituents of the growth chamber to the atmosphere.

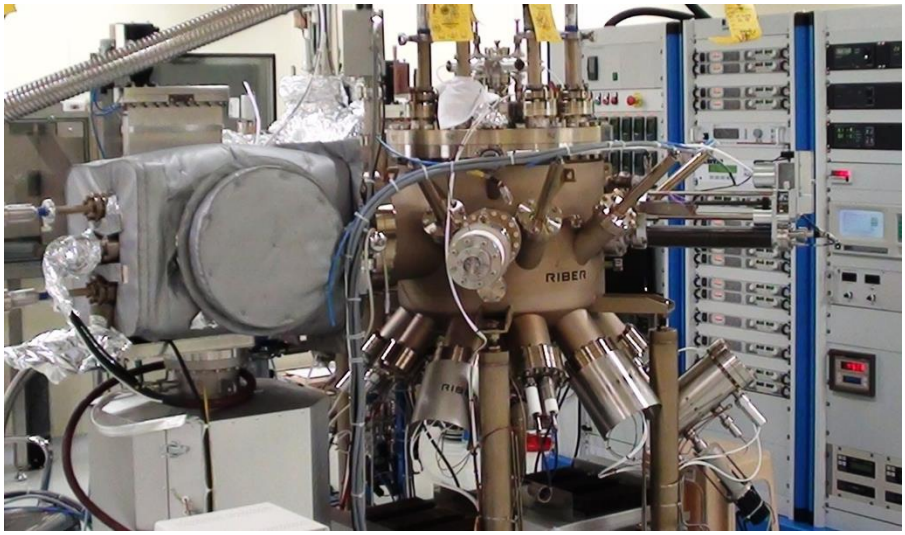

Fig.4.1 *The Riber Epineat MBE system at IIT Bombay, specially designed to grow As-based compound semiconductor crystal.*

A vacuum inter-lock or introduction chamber is employed to allow inter-chamber transport of substrate through a small vacuumed carrying device without introducing much air load into the main vacuums. The transportation of the substrate from the loading chamber to the growth chamber is very crucial to keep vacuum integrity intact. In modern days MBE systems, this is done by employing magnetically coupled transport rods in conjugation with some trolley system and rotary pumped to vacuum. The buffer chamber is often used for additional substrate preparation and storage. Surface characterization tools like XPS or AES are installed inside the buffer chamber. Tools like Mass Spectroscopy or Electron Diffraction are also employed for real-time measurements. The third vacuum chamber is used for actual growth which is kept in isolation while material growth or the introduction of the substrate. The isolation is compulsory for maintenance of contamination-free growth during the pressure burst related to the opening of the introduction chamber and incorporation of surface probes at the time of growth.

Modern-day MBE systems, designed for large commercial throughputs employ simultaneously grown multiple large area wafers. This is usually achieved by mounting the large area wafer on a rotating platen capable of receiving the beam flux from multiple sources. This effectively increases the size of the growth chamber and material output.

4.2.1 Details of the growth chamber

The growth chamber which is the most critical part of the MBE system typically constituted of the following essential components, as shown in Fig.4.2:

Source ovens: The growth chamber contains heated Knudsen effusion cells for III-element source material like Ga, In, Al, Be (p-doping), Si (n-doping) and a cracker cell for V-element As. The sources are designed according to the material-dependent temperature of evaporation. All the cells are mounted and surrounded by a chilled liquid N_2-filled panel to reduce radiative heating of the chamber. The cells containing the sources are usually made of pristine pyrolytic

boron nitride (PBN) which is the least reactive with a wide range of source material, including highly reactive elements like Al and Ga. The cells are equipped with conically shaped crucible to ensure high uniformity of the deposited layer. The As the source is equipped with a needle valve and cracker wherein the ejected As-flux from a heated As ingot is controlled with the valve, After crossing the valve system, the As the beam passes through a cracker tube which converts As_4 to other molecular species As_2. The beam of As_2 is preferred over As_4 mainly due to lower consumption and more efficient incorporation into GaAs substrate. This finally leads to better crystal growth with pristine quality.

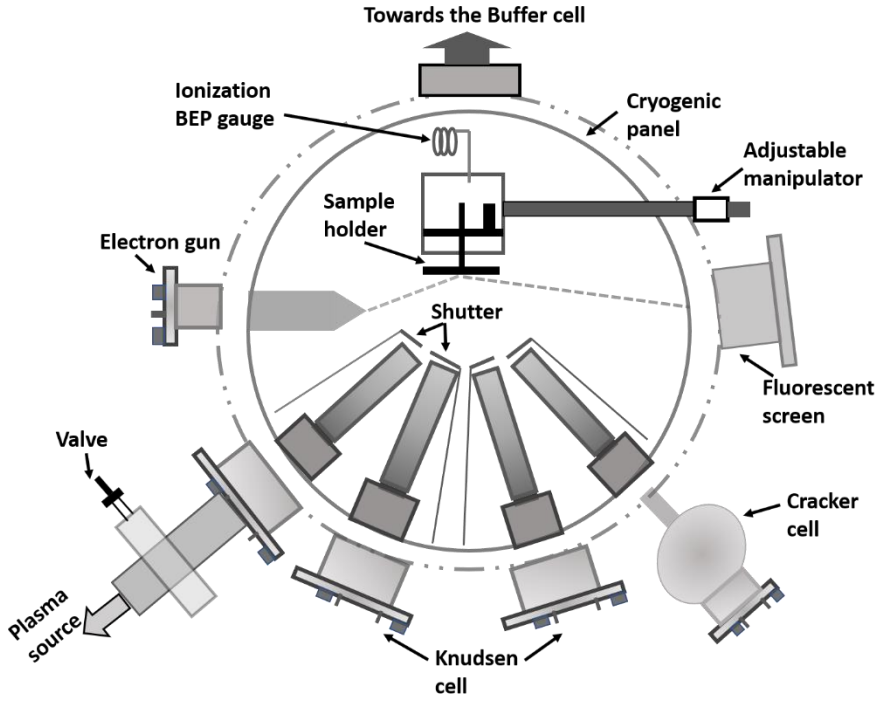

Fig.4.2 Schematic representation of experimental MBE set-up with its components.

Beam shutters and actuators: Beam shutters are basically Ta plates installed across the beam to tune the time of flux reaching the substrate.

Substrate holder and heating arrangement: Substrate mounting is an important aspect for epitaxial growth where precise control over temperature is critical. A wafer of crystalline semiconductor material is mounted on a holder and heated by an underlying metal heater through a proper thermal contact with the substrate. Usually, a low melting metal such as In is

employed to make liquid thermal contact with the heater at the growth temperature. Alternatively, the use of a more advanced radiative coupling between substrate and heater has become more popular nowadays. The wafer of suitable dimension to fit into a particular holder is placed on an open ring with a ribbon wound around it. The radiation with an energy greater than the semiconductor wafer bandgap rapidly heats the substrate.

There is additional importance of substrate holder related to the uniformity of grown layers when more than one sources are used. For example, when Ga and In beams are directed along with two different directions onto a large substrate to grow films of binary alloy InGaAs, there is a great chance of inducing a high concentration gradient on the wafer. This is avoided by continuously rotating the holder along with the wafer throughout the growth. Typically, for a growth rate of 1 ML/s, the speed of rotation has to significantly fast to avoid the formation of any concentration fluctuation. However, the rotation of the substrate gives rise to a designing difficulty to mount a thermocouple for accurate temperature measurement which usually needs a good stationary thermal contact with the substrate surface. Taking this into consideration, modern MBE systems are equipped with a non-contacting stationary thermocouple to measure the temperature through recording of the radiant flux from the substrate. But this only provides the information of relative change in temperature. For absolute calibration of substrate temperature, the infrared optical pyrometer is used in order to measure temperature in the range 400-700 degree C. For temperature measurement of the semiconductor substrate, the energy window of the pyrometer is chosen above the bandgap of the substrate.

Vacuum pumps: A system of ionic pumps in conjunction with cryo panels in the growth chamber help to keep a vacuum as high as 10^{-9}-10^{-10} torr while the effusion cells are heated to the working temperature. Samples are loaded onto a rotating sample holder inside the growth chamber through a magnetically coupled transfer rod. The sample holder is designed for executing continuous azimuthal rotation for better uniformity of the grown epilayer. The

chamber pressure or more specifically the beam equivalent pressure (BEP) of the material sources is determined by an ion gauge mounted on the opposite side of the sample. A system of additional cryopumps is used to remove the residual undesirable gases like CO_2 and H_2O which is capable of keeping the respective partial pressure less than 10^{-11} Torr.

In-situ growth characterization tools: The in-situ growth rate measurements are most commonly obtained from RHEED observations of growing film or crystal structure. RHEED system consists of an electron gun and a phosphor screen displaying the real-time RHEED pattern of the growing surface under the exposure of the molecular beam [4]. RHEED works on recording the time-dependent diffracted intensity coming from the temporary evolution of the growing structure. Usually, the information like growth rate, surface topography, and composition of the evolving structure are monitored by observing the intensity of the specular diffracted beam as a function of time.

The ultra-low density of ambient atomic concentration in the UHV also makes the operation of tools like Mass spectroscopy and Electron diffraction possible which are used for real-time measurement of the growing layer surface and its environment in the close vicinity of the growing region. In addition to RHEED, these are also very useful tools for in-situ observation.

4.2.2 Chamber preparation prior to growth

While growing III-V based compound in MBE, the substrate temperature and the V/III ratio are chosen in such a way that the adatom diffusion and the growth rate is effectively controlled by the incorporation rate of group-III element alone, depending upon their growth kinetics [5-7]. For fabrication of GaAs-based heterostructures, GaAs substrate mounted on molybdenum supports are introduced into the loading chamber where they are degassed for 2 hours at 120˚C prior to the sample growth. Then, it is taken into the preparation chamber where it is heated for two hours at a temperature around 400˚C. After that, the heated substrate is brought into the

growth chamber and heated to 630˚C under an over-pressure arsenic atmosphere to remove the protective surface oxide layer. Then a 200 nm-thick GaAs layer is deposited at 590˚C to achieve the working surface quality before the actual growth of the multilayers. The substrate temperature is measured by an optical pyrometer mounted on the sample holder facing the sample surface.

4.3 General mechanism of MBE growth

Information about the dynamics of the growing surface is very essential to optimize the growth mechanism. Many real-time measurements have shown that MBE growth produces a well-ordered surface with great freedom of altering surface chemical composition and the arrangement in atomic layers. The theory of the basic MBE growth model is reviewed by Tsao et al [8].

At the beginning of the growth, usually, the surfaces are rough at the nanoscale. But, once the epitaxial growth sets in, the surfaces start to become smooth rapidly. This was explained by Frank and van der Marwe as a consequence of the migration of atoms over the flat terraces of rough surface and incorporation of step edges advancing the terraces [9]. The step edges bounded by wider terraces advance more rapidly as compared to those which are bounding the narrow terraces. As a result of that, the wider terraces grow in a bigger size while the narrow ones disappear and the surface becomes smoother.

Homo-epitaxial and hetero-epitaxial growth of single component growth (one element, like Si and Ge) and compound growth (more than one element, like SixGe1-x, GaAs, AlAs, $Al_xGa_{1-x}As$ and $In_xGa_{1-x}As$, etc) are routinely performed in MBE system.

4.4 Hetero-epitaxial growth of strained layers

Fabrication of two-dimensional structure is one of the most important aspects of MBE where alternating thin layers of two different semiconducting materials are grown which have similar

or dis-similar lattice constants. If layers of different materials having the same lattice constants, namely homoepitaxial layers are stacked with certain periodicity larger than the lattice spacing, it forms a superlattice. On the other hand, if a hetero-epitaxial layer is grown on a lattice-mismatched substrate, the initial growth of the film occurs through adopting the in-plane lattice constant of the substrate. This growth of the film over the substrate is 'pseudomorphic' where a uniaxial tensile strain is induced on the film. Now with increasing the lattice mismatch, the distortion causes increasing strain in the film up to an extent. Above that, the excess strain becomes relaxed through the formation of some misfit dislocation in the interfacial plane. There is a characteristic thickness of the film layer at which the strain is sufficient for the formation of dislocation, called 'critical thicknesses'. The critical thickness for pseudomorphic growth depends on the elastic constant of the film material. But as long as the film thickness is below the critical thickness, there are some artificial as well as spontaneous processes to get rid of the possibility of dislocation generation. Sometimes, the structure of the substrate and high temperature of the film surface may force the epilayer growing into a thermodynamically stable pseuodomorphic configuration, depending upon the interfacial energy and lattice strain. This may result in the formation of islands of epitaxial material instead of a smooth surface through layer-by-layer deposition by Frank-van der Merwe mode [10]. Island formation can occur in two ways, either on clean surfaces with no 2-D layer (Volmer-Weber growth) or after the growth of the surface above one monolayer (Stranski-Krastanov growth) [11-12]. The spontaneous growth of three-dimensional islands by Stranski-Krastanov (SK) mode is commonly known as a self-assembled quantum dot.

4.4.1 Growth of self-assembled quantum dot

Self-assembled quantum dots are formed as a consequence of excess strain relaxation between epitaxially grown lattice-mismatched epilayers. InAs/GaAs QD is one such model systems for self-assembled formation with large lattice mismatch (~7%) between InAs and GaAs epilayer.

However, with piling up more material above the critical thickness, the accumulated strain can also lead to the formation of extended defects. Thus, the thickness of the grown QD layer must have enough precession to fabricate defect-free structures. The introduction of epitaxial growth techniques, like the Molecular beam epitaxy (MBE), can provide such atomic order precession to the layer thickness. Now depending upon the amount of QD material (InAs) deposition in the host material (GaAs), the growth of QDs can be mediated through two distinct growth modes: Stranski-Krastanov and sub-monolayer epitaxial deposition. SK growth mode is related to layer coverage in between 1-2 monolayer (ML) or above. This is a more conventional way to grow self-organized QDs. The sub-monolayer growth mode is limited to the layer coverage below 1 ML. Growth of self-assembled InAs/GaAs quantum dots by both of these two modes are discussed in detail in this chapter.

4.4.1.1. SK quantum dot

Heteroepitaxial growth of thin films on a crystalline substrate is mainly mediated through three processes depending upon the strength of interaction of the adatoms with the substrate surface, as schematically shown in Fig.4.3. The adatoms stick to the preferential sites of the substrate surface when the compressive strain on the epitaxial layer grown on the substrate is minimal. This leads to the growth of atomically smooth two-dimensional (2D) layers through the Frank-van der Merwe mode. The strain starts to increase with the thickness of the epitaxial layer and beyond a certain critical thickness of the epilayer, it finds an easy route of reliving the excess strain energy by reducing the surface area through the formation of isolated 3D islands. This mode of quantum dot growth is referred to as Stranski-Krastanow (SK) mode where a transition from 2D layer-by-layer to 3D islands takes place. This is the most widely accepted growth mode of self-assembled QDs with high crystal quality and better optoelectronic properties. On the other extreme, if the strain is very high due to the large lattice misfit between the epilayer and the substrate, the adatom-adatom interaction dominates over the interaction between

adatom-substrate which eventually leads to direct formation of 3D adatom islands. This regime of growth is called the Vollmer-Weber growth mode. The three growth modes are schematically represented in Fig.4.3 for different layer coverage in between 1-2 monolayer (ML) or above.

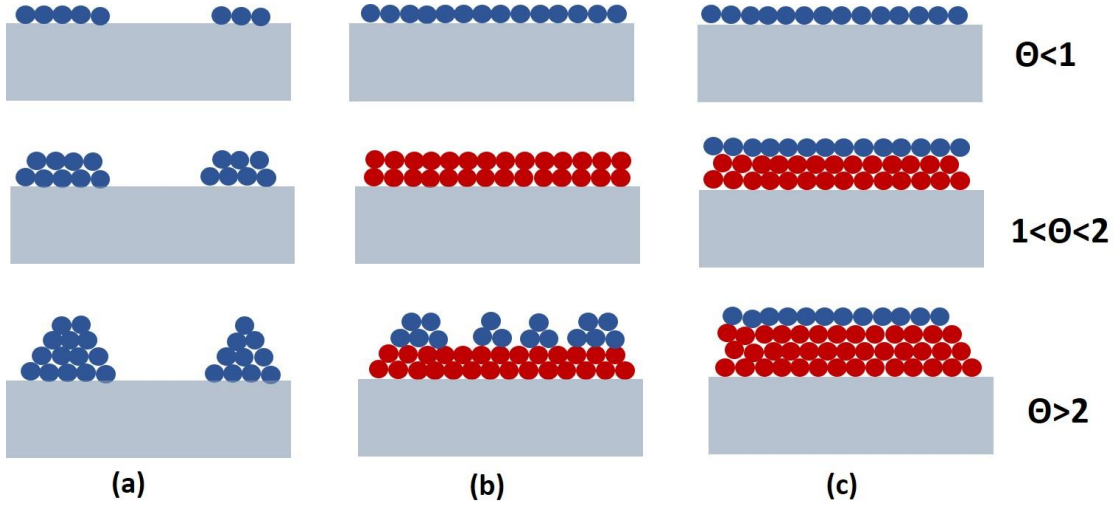

Fig.4.3 The schematic representation of the three main growth modes for different values of surface coverage Θ: (a) Volmer-Weber (VW), (b) Stranski-Krastanow (SK) and (c) Frank-van der Merve (FM).

4.4.1.2 Sub-monolayer quantum dot

There is also an alternative epitaxial technique to grow self-assembled QDs by inserting less-than-a-monolayer thick layers of quantum dot material in the host matrix of higher bandgap material. When the amount of deposited QD material (InAs) is lower than that required to form a complete 2-D monolayer over the substrate, an InAs-rich patch like isolated flat islands with 6-8 nm in diameter are formed due to the effect of lattice strain between epitaxial layer and substrate. The existence of a minimum in total energy per particle for a certain number of particles, as formulated from different theoretical frameworks supports the formation of such a stable structure [13]. In other words, deposition of material over a substrate in a small amount (below 1 ML coverage) can lead to the formation of stable 2-D islands (low height/diameter ratio) or sub-monolayer QDs depending upon the elastic constants of the growing material. While alternatively stacking the hetero-epitaxial layers of QD material (like InAs) and substrate

(like GaAs) along the growth direction, such islands become embedded in the heterostructure and start to vertically correlate due to surface strain. The electronic wave functions of such vertically aligned islands in the multi-stack have a strong degree of overlap which makes it characteristically equivalent to a quantum dot. This sub-monolayer epitaxial growth mode is schematically represented in Fig.4.4 for different layer coverage below 1 ML.

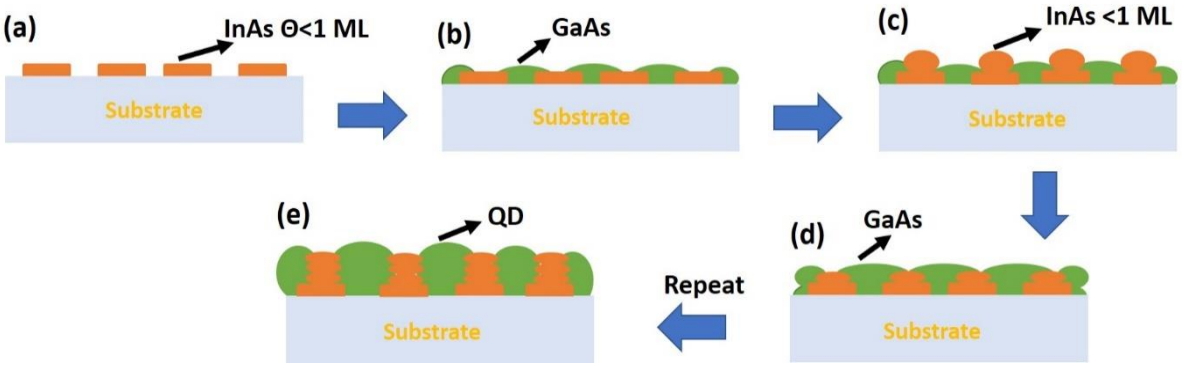

Fig.4.4 *The SML-QDs growth process. (a) Flat InAs islands with surface coverage below 1 ML, (b) Island buried due to subsequent deposition of GaAs layer, (c) The second layer of InAs islands, vertically self-aligning to the previous InAs layer islands due to the surface strain, (d) Islands again buried under subsequent GaAs layer, (e) After repeating the (a)-(d) process, QDs are formed.*

4.5 Laboratory MBE growth

InAs/GaAs self-assembled quantum dots are grown in our MBE system upon semi-insulating crystalline (001) GaAs wafer, both by SK mode and sub-monolayer epitaxy.

4.5.1 Growth of InAs/GaAs SK-QD heterostructure

A semiconductor heterostructure has been grown in our MBE system with InAs/GaAs self-assembled SK-QD. At first, a 200 nm-thick GaAs buffer layer was grown at 590°C under a background pressure of $1x10^{-7}$ Torr. This is followed by the growth of the active region consisting of four stacks of alternative deposition of InAs and GaAs epilayers. One such structure has been repeated twice to form the heterostructure. The InAs layers were grown 2.2 ML thick at the rate of 0.1 ML/s. During the growth, the temperature of the active region was set at 480°C and As_2 pressure was lowered to $1x10^{-5}$ Torr. In our case, SK QDs were grown as

a reference sample which enables characteristic comparison with the InAs/GaAs sub-monolayer quantum dots grown under identical conditions.

4.5.2 Growth of InAs/GaAs SML-QD heterostructure

The sample under consideration was grown by molecular beam epitaxy (MBE) equipped with As_2 cracker source on a semi-insulating GaAs (100) substrate. The active region of the sample consists of 4 stacks of alternative insertions of InAs sub-monolayer (less than a monolayer coverage) and lattice-mismatched 1.5 ML thick GaAs barrier layers. Consequently, In-rich small clusters or quantum dots are spontaneously formed in the GaAs host matrix. This structure is repeated for two periods each of which is separated vertically by 1 nm thick GaAs spacer layer, as shown by a schematic in Fig.4.5. The thin spacer layers are capable of

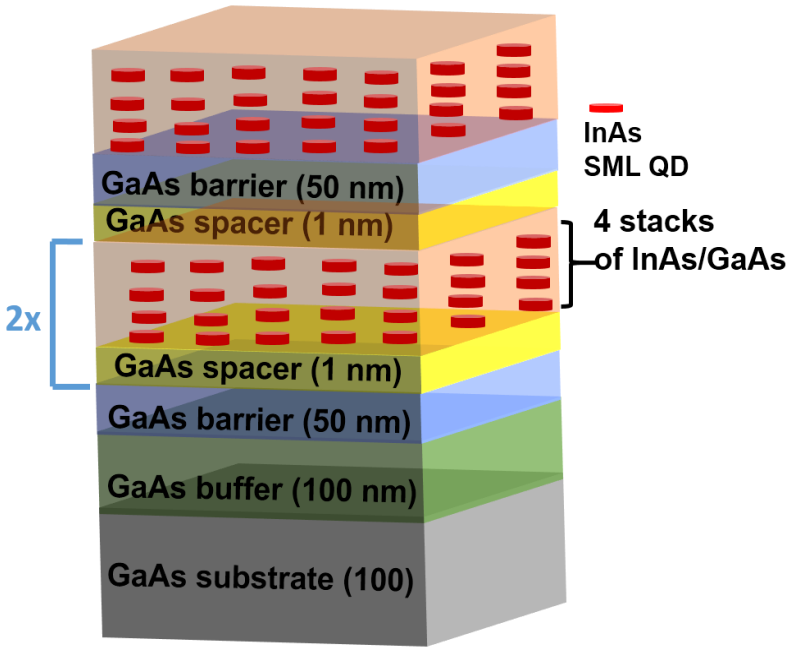

Fig.4.5 *Vertical multi-structure containing a periodic array of embedded InAs SML quantum dots in GaAs matrix.*

transferring the strain fields to the next quantum dot layer and thus can offer better vertical correlation [14-15]. The sub-monolayers were deposited at a very slow rate of 0.032 μm/hr to maintain uniformity in the grown islands. The growth time of InAs layer deposition has been set at 13 sec, 20 sec, 23 sec and 26 sec for 0.4 ML, 0.6 ML, 0.7 ML, and 0.8 ML surface

coverage respectively. First, a 200 nm thick GaAs buffer layer was grown at 590 ºC. Then the temperature was reduced to 480 °C to grow the SML stacks and GaAs spacer layer followed by a 50 nm thick GaAs barrier layer grown above the active region at 590ºC. For sub-monolayer growth, Arsenic pressure was set at ~ $1x10^{-5}$ Torr with As_2 flux of ~$5x10^{10}$ cm^{-2} sec^{-1}.

4.6 Bibliography

[1] M. Ettenberg, Appl. Phys. Lett. **27** (1975) 652.

[2] Z. Alferov, D. Garbuzov, V. S. Grigor'ev, Y. Zhilyaev, L. Kradinova, V. Korol'kov, E. Morozov, O. Ninua, M. K. Trukan, Sov Phys. Solid State **9** (1967) 208.

[3] S. Mukherjee, A. Pradhan, T. Maitra, S. Mukherjee, S. Sengupta, S. Chakrabarti, A. Nayak, S. Bhunia, J. Lumin. **215** (2019) 116597.

[4] John R. Arthur, Surface Science **500** (2002) 189-2175.

[5] P. Smilauer, D. D. Vedensky, Phys. Rev. B **48** (1993) 17603.

[6] Zangwill, C. N. Luse, D. D. Vvedensky, M. R. Wilby, Surf. Sci. Lett. **274** (1992) 529.

[7] K. Myers-Beghton, D. D. Vvedensky, Phys. Rev. B **42** (1990) 5544.

[8] C. T. Foxon and B. A. Joyce, Surf. Sci. **64** (1977).

[9] F. C. Frank and J. H. van der Merwe, Proc. Roy. Soc. A **198** (1949) 125.

[10] W. Mo, B. S. Swartzentruber, R. Kariotis, M. B. Web, M. G. Lagally, Phys. Rev. Lett. **63** (1989) 239340.

[11] M. Volmer, A. Weber, Z. Phys. Chem. **119** (1926) 277.

[12] N. Stranski, L. Krastanov, Ber Akademie der Wissenschaften und der LiteraturMathe,matisch-Naturwissenschaftliche Klasse, **146** (1939) 797.

[13] E. Bauer and H. Poppa, Thin Solid Films **12** (1972) 167.

[14] Phu Lam, Jiang Wu, Mingchu Tang, Qi Jiang, Sabina Hatch, Richard Beanland, James Wilson, Rebecca Allison, Huiyun Liu, Solar Energy Materials & Solar Cells **126** (2014) 83–87.

[15] S. Shetty, S. Adhikary, B. Tongbram, A. Ahmad, H. Ghadi, S. Chakrabarti, J. Lumin. **158** (2015).

Chapter 5

Structural and optical characterization of InAs/GaAs sub-monolayer quantum dot

5.1 Introduction

The optical and electronic properties of low-dimensional structures strongly depend on shape and size. The strain in the system also plays a very important role to determine the luminescence properties. To explore the dependence of optoelectronic properties of sub-monolayer QD heterostructure on its structural details with varying InAs sub-monolayer coverage, a combined study of strain, size and in-plane spatial distribution of QDs has been performed systematically. The experimental and simulation results with adequate explanations are discussed in detail in this chapter.

5.2 Structural characterization

5.2.1 Determination of morphology of surface QDs from AFM measurement

The variation in morphology of the surface quantum dots as a function of coverage fraction from 0.4 ML to 0.8 ML has been investigated by Atomic force microscopy (AFM) in contact mode. AFM micrographs, as shown in Fig.5.1 (a)-(d) have been obtained by analysing the uncapped quantum dots. The lateral size distribution of QDs for different SML coverage (0.4, 0.6, 0.7 and 0.8 ML) have been extracted from the respective micrographs and represented as histograms in Fig. 5.1 (e)-(h). The average QD diameter has been evaluated by fitting the respective size distribution by suitable fitting functions. The measured average diameter of 8, 12, 14 and 17 nm for 0.4, 0.6, 0.7 and 0.8 ML respectively, indicates a clear decreasing trend of QD diameter with decreasing SML coverage. The areal dot density is also reduced by an order of magnitude from $9x10^{10}$ cm^{-2} to $2x10^{10}$ cm^{-2} as the coverage fraction is reduced from 0.8 ML to 0.4 ML.

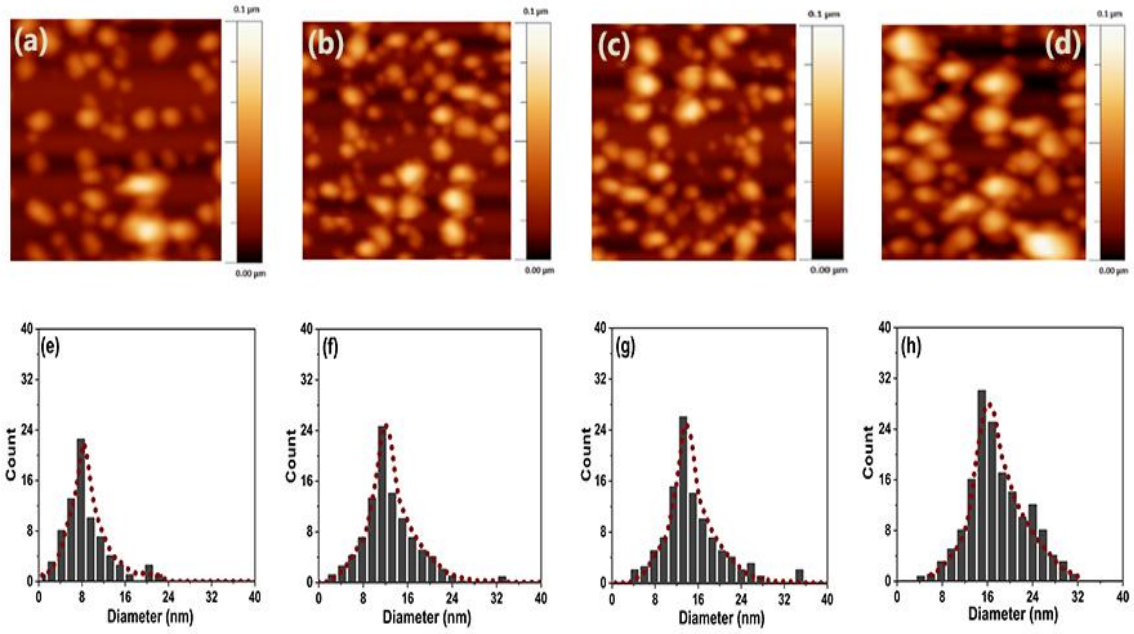

Fig.5.1 *AFM image (a, b, c, d) of the surface SML QDs taken within a scan range of 0.8 x 0.8 µm^2 and the respective QD diameter histogram (e, f, g, h) for different InAs coverage (0.4, 0.6, 0.7 and 0.8 ML). The dotted line is representing the fitting of QD diameter distribution.*

5.2.2 Structural impression of QDs from TEM imaging

The two-period cyclic insertion of InAs SML dots in GaAs host matrix is visualized by the two strip regions of width 7-9 nm, separated by a gray barrier layer of GaAs, exhibiting a significant contrast in the cross-sectional bright-field transmission electron microscope (TEM) image as shown in Fig.5.2 (a). The dark patches in the associated high-resolution TEM (HRTEM) images (Fig.5.2 (b)) provides the impression of the grown SML QDs or InAs-rich regions with low height to diameter aspect ratio. To detect the existence of quantum dots formed by vertical stacking, a depth-wise line profile has been obtained by energy dispersive x-ray (EDX), as shown in (Fig.5.2 (d)). The periodic peaking up of In concentration is the signature of cyclic insertion of InAs sub-monolayers in GaAs matrix. To visualize the lateral arrangement of the SML QDs, elemental mapping over a selected area has been performed by employing high angle annular dark-field scanning transmission electron microscopy (STEM-HAADF). Figure

5.2 (e)-(g) illustrates the elemental (Ga, AS and In) mapping corresponding to a selected area of the TEM image, as shown in Fig.5.2 (c).

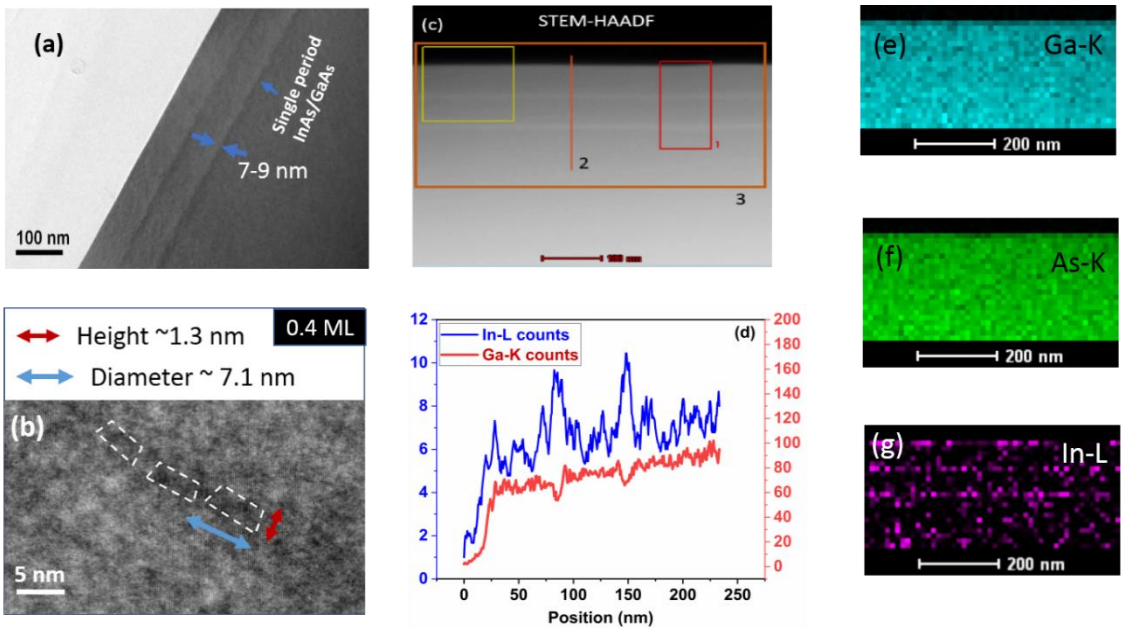

Fig.5.2 *(a) The bright field cross-sectional and (b) the corresponding high resolution TEM image for 0.4 ML InAs coverage. The encircled objects with black contrast are characteristically showing the InAs-rich regions or sub-monolayer quantum dots. (c) High angle annular dark-field scanning transmission electron microscopy (STEM-HAADF) image. (d) EDX depth-wise line profile along the selected line '2' and (e)-(g) the elemental mapped images over the selected area '3' in figure (c).*

5.2.3 Strain analysis from XRD measurement

The average strain in the heterostructure and the effect of surface stress upon the growth of the embedded InAs-rich islands have been analysed by θ-2θ x-ray diffraction (XRD) scan as a function of InAs sub-monolayer coverage. as shown in Fig.5.3. Two Bragg peaks appeared for each of the samples. The peaks are de-convoluted by a standard Gaussian fitting function. The fitting has been performed with reduced χ^2.value of ~5×10^{-3}. The narrower and more intense peak at θ_s ~33.1º is related to the Bragg reflection from substrate GaAs (004) crystal planes whereas the broadened peak located at a lower angle (θ_{QD}) is associated to (004) Bragg reflection from InAs quantum dots. The average out-of-plane hydrostatic lattice strain in the multi-structure acting upon the embedded dots relative to the substrate layer has been estimated as a function of InAs sub-monolayer coverage by using the relation [1-2]

$$\varepsilon_z(d_{InAs}) = (sin\theta_S - sin\theta_{QD})/sin\theta_S \qquad (5.2.3.1)$$

The evaluated strain values are enlisted in the Table-5.1 for different sub-monolayer coverage. The progressive shift of angle (θ_{QD}) of the QD related XRD peak away from the substrate peak with decreasing SML coverage is a signature of increasing out-of-plane tensile strain in the grown multi-structure.

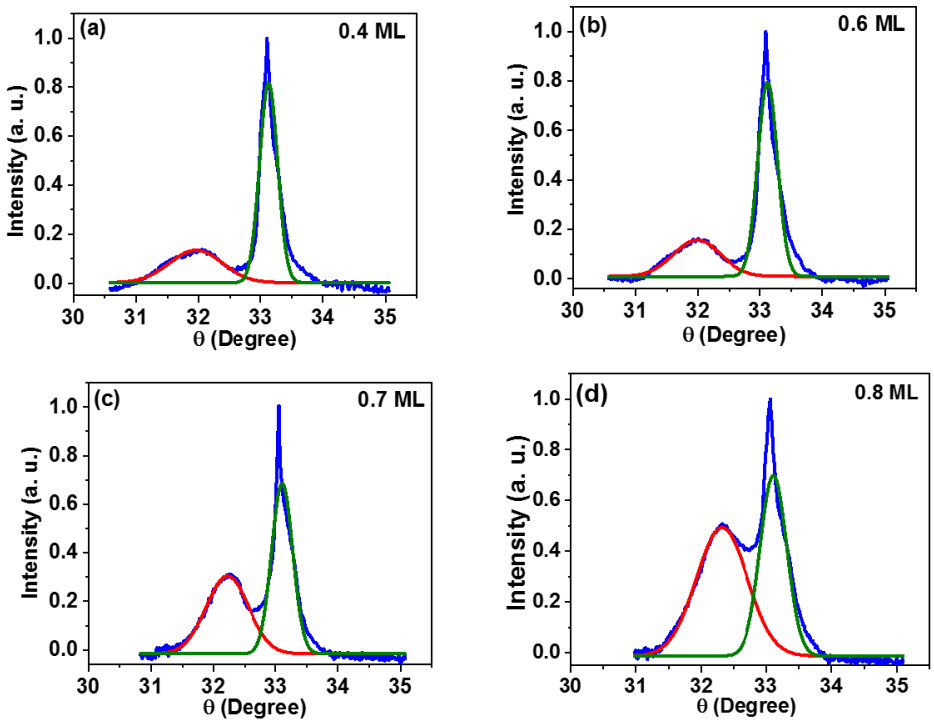

Fig.5.3 *Intensity vs θ plot of θ-2θ XRD scan (dotted lines). The experimental results have been de-convoluted with fitting function (solid lines) with reduced χ^2.value ~ 10^{-3}, for different InAs coverage (0.4-0.8 ML). Evidently, the broad peak related to (004) InAs reflection gradually shifts towards the (004) GaAs related peak with increasing SML coverage.*

The corresponding average in-plain component of this strain acting upon the embedded quantum dot surfaces is evaluated by using bi-axial strain relation

$$\varepsilon_{xx} = \varepsilon_{yy} = \varepsilon_{\parallel} = -\frac{\varepsilon_z}{\sigma_{st}} \qquad (5.2.3.2)$$

where $\sigma_{st} = 2C_{12}/C_{11}$ is the Poison's ratio of the grown InAs pseudomorphic layer [1]. C's are the elastic constants of InAs having the values of C_{11}=0.833 and C_{12} =0.453 [3]. This strain is compressive in nature and isotropic over the entire x-y plane. This is a valid approximation,

as long the active shear strain is negligibly small. The associated surface stress of the compressed InAs layers due to locally exerted strain is estimated by using

$$\sigma_0 = \frac{Y}{1-\sigma_{st}}\varepsilon_{\parallel} \qquad (5.2.3.3)$$

where Y is Young's modulus of pure InAs pseudomorphic layer [4]. The measured values of ε_z, $\varepsilon_{\parallel}$ and σ_0 for different SML coverage (0.4-0.8 ML) are enlisted in Table-5.1. The effective compressive stress has been measured to increase from 54.5×10^8 to 178×10^8 as the sub-monolayer coverage is reduced from 0.8 ML to 0.4 ML. Evidently, the reduction of InAs coverage leads to building up of excess in-plane strain and compressive surface stress upon the SML-QDs embedded in GaAs host matrix.

Table-5.1 ***Measured quantities from XRD scan***

InAs coverage (ML)	**Θ_S (degree)**	**Out-of-plane strain ε_Z (x 10^{-2})**	**In-plane compressive strain $\varepsilon_{\parallel}$ (x 10^{-2})**	**Compressive Surface stress σ_0 (x10^8 Pascal)**	**Average QD height (nm)**
0.4	32±0.008	3.08±0.003	-3.1±0.003	178±0.4	1.4
0.6	32.05±0.009	2.814±0.001	-2.96±0.002	171±0.3	1.55
0.7	32.24±0.007	2.478±0.004	-2.6±0.004	135±0.2	1.9
0.8	32.39±0.008	1.784±0.004	-1.9±0.005	54.5±0.2	2.3

5.2.4 Raman Analysis: Simulations by using phonon confinement model

Observation of phonon response is an important aspect both for providing spectral evidence of the formation of the QDs and for quantitative understanding phonon-energy shifts due to the confinement and strain inside the QDs. Figure 5.4 (a) shows the Raman spectra of the SML-QDs which exhibits several key features and trends, such as (i) two-mode asymmetric and broadened optical phonon response at lower energies related to the sample structure which gets red-shifted with decreasing fractional coverage of InAs and (ii) strong transverse (TO) and

longitudinal (LO) optical phonon response for the host GaAs material at 270 cm^{-1} and 295 cm^{-1}, respectively [5]. The appearance of the additional feature of strong GaAs TO Raman peak under back-scattering geometry which were absent in the pure bulk GaAs sample without quantum dot (Fig.5.4 (b)) indicates relaxation of certain phonon selection rules attributed to release of some strain induced in the GaAs matrix in the presence of the QDs [6-7]. In addition to that, the asymmetric and broadened redshifted phonon line-shapes which could be de-convoluted to obtain two distinct peaks (Fig.5.4 (c)) characteristically confirms the formation of InAs quantum dot structure with inhomogeneous vertical size distribution [8-9]. The de-convoluted asymmetric Raman peaks which obeyed all the selection rules of phonon modes (TO and LO) in normal zinc blend material can thus be readily considered to be first-order InAs-like TO and LO phonon peaks related to InAs SML-QDs [10-12]. As the InAs coverage is decreased, these peak positions are increasingly red-shifted from bulk InAs TO (230 cm^{-1}) and LO (240 cm^{-1}) which serves the spectral evidence of progressively enhanced confinement effect in InAs SML-QDs [13]. One may also notice that the spectral intensity of the SML-QDs relative to that of GaAs substrate material progressively increases with increasing coverage of InAs layer which indicates the increment of the effective volume of the grown quantum dots.

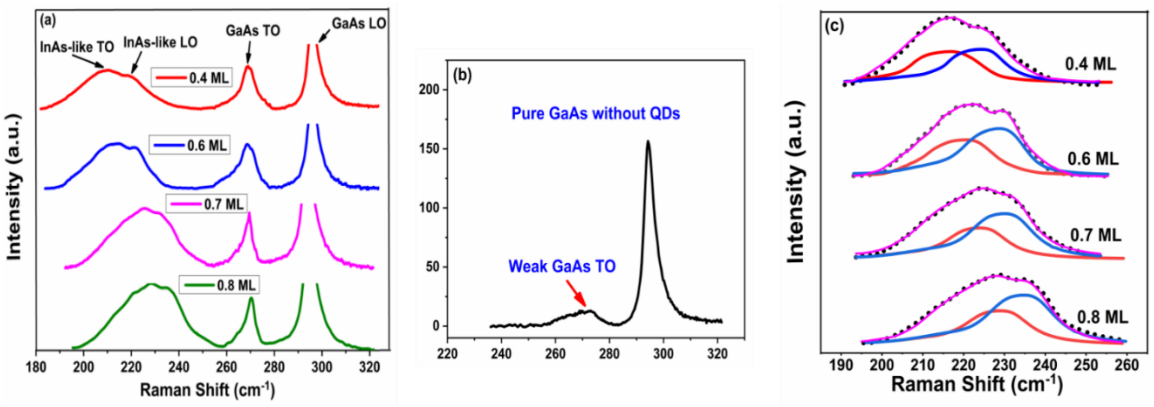

Fig.5.4 *(a). Raman spectra from the QD samples for different InAs sub-monolayer coverage. (b) Raman spectra of reference pure GaAs sample. (c) Enlarged view of QD related contribution (dotted) with resolved InAs-like TO and LO phonon response (red and blue) fitted by PCM model with reduced χ^2 values of ~10^{-3}. Evidently, both the Raman modes red-shifted with decreasing InAs coverage.*

Both the effects of phonon confinement and average strain may simultaneously lead to the shift of phonon energy from the bulk value [14-17]. Spatial confinement of phonons gives rise to Raman redshift whereas the compressive strain leads to blueshift in Raman peak energy [18]. In our case, the energy blueshift due to the compressive lattice strain as estimated from the XRD analysis, has been incorporated as a correction term to the phonon energy in the expression of scattered phonon intensity following the phonon confinement model. The asymmetric Raman line shape can be well described by a model of phonon confinement inside the inhomogeneous nanometre-sized InAs islands which is used to fit the two-mode QD phonon response by considering a Gaussian confinement function [19].

The total scattered Raman intensity I(w) from an ensemble of nano-crystallites of dimension L, defined as integral of a superposition of weighted Gaussian contributions from all the wave vectors throughout the whole Brillion zone can be approximated to [20]

$$I(w) = \sum_{i=1}^{2} \int_{0}^{\infty} \frac{exp\,(-(L-L_0)^2/2\sigma^2)}{\sqrt{2\pi}\sigma} \times \int_{BZ} \frac{C(q)^2 d^3q}{(w - \{w_i(q) + \Delta w_i(q)\})^2 + (\Gamma/2)^2} \quad (5.2.4.1)$$

where Γ is the natural Raman full width at half maximum (FWHM), q is the wave vector, $w_i(q)$ is the linear two-atom InAs phonon dispersion function [1] for the selected Raman mode. The discrete sum is taken over two selected modes with necessary weightage to fit the experimental Raman line shape. The spatial phonon confinement inside the QDs is represented by the Fourier coefficient of the Gaussian phonon confinement function $C^2(q) = \exp(-q^2L^2/8\beta)$, where L is the length dimension (dot height) along the direction of phonon confinement and $\beta=2\pi^2$ according to Campbell's Phonon confinement (PCM) model [21-22]. More realistically, the SML-QDs may have a size distribution which can cause more asymmetric broadening of Raman line shape. This has been incorporated in the model by a Gaussian size distribution function centered at the mean size (vertical) L_0 with standard deviation σ (Table-5.2). The combined effect of phonon confinement and average compressive strain including the QD

finite-size dispersion seemed to explain well the energy shift and asymmetric broadening of the phonon peak at lower energy. The effect of the weak average (inhomogeneous) compressive strain [23] leading to small energy blue shift of the two-mode InAs-like Raman response is justifiably incorporated in the model (Eq. 5.2.4.1) by the extra term $\Delta w_i = -3\gamma_i w_i(q)\varepsilon_{||}$ in the phonon energy expression, where $\varepsilon_{||}$ is the average in-plane compressive strain, directly used from the respective XRD data (from Table-5.1) associated with different InAs ML coverage and γ_i is the Grüneisen parameter for the selected Raman mode of InAs [1]. The mean QD height (L_0), SD of QD height distribution (σ) and Raman peak FWHM (Γ) are the extracted parameters obtained by fitting the experimental Raman line shapes by the aforesaid phonon confinement function with reduced χ^2.value of $2x10^{-3}$-$6x10^{-3}$. The measured Raman redshift, extracted average QD height (L_0) with finite-size dispersion (σ) for different InAs coverage are tabulated in Table-5.2 and plotted as functions of InAs layer coverage in Fig.5.5. Both the

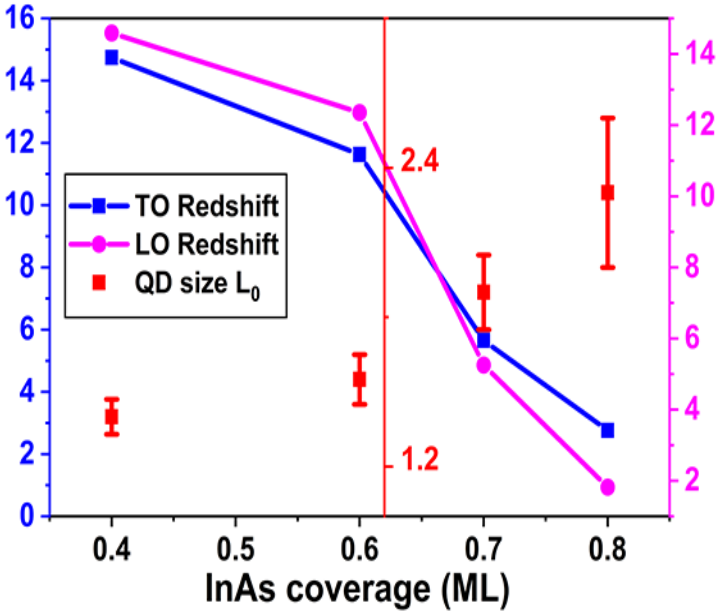

Fig.5.5 *Dependence of observed redshift of InAs-like LO and TO Raman peak and the extracted average QD size (height~L_0) with corresponding QD size dispersion (σ) quantitatively represented by the error bar.*

InAs-like (TO and LO) Raman peaks are observed to get more redshift with decreasing InAs layer coverage which is a measure of stronger phonon confinement induced by quantum size

effect inside SML-QDs of decreasing size. From the Raman redshift, the effect of exciton-phonon interaction can be inferred qualitatively [7]. As stronger phonon confinement inside lower dimensional structures is usually associated with enhanced exciton-phonon coupling via the Fröhlich [14] interaction, it is very likely that with decreasing InAs coverage the exciton-phonon coupling strength increases [24]. This may affect the luminescence properties by playing a vital role in phonon-assisted carrier relaxation, especially at higher temperatures. The estimated small SD of QD size distribution of 5-12% with respect to the mean QD height L_0 for different InAs coverage (0.4-0.8 ML), as shown in Table-5.2, suggests a reasonably homogenous growth of QDs by sub-monolayer epitaxy. The QD size distribution gets a little dispersed with increasing InAs coverage. This is evidence of tuning the dot size with very small size fluctuations by varying the active thickness of InAs sub-monolayer.

Table-5.2 ***Extracted QD size with dispersion from the PCM model***

InAs Coverage (ML)	**TO redshift (cm^{-1})**	**LO redshift (cm^{-1})**	**Average dot height L_0 (nm)**	**Size Dispersion (nm)**
0.4	14.6±0.35	14.47±0.94	1.4±0.005	0.06±0.009
0.6	12.35±0.82	11.65±0.69	1.55±0.009	0.098±0.009
0.7	5.25±1.12	5.65±0.80	1.9±0.009	0.17±0.005
0.8	1.82±0.54	2.76±0.55	2.3±0.003	0.35±0.006

5.2.5 Qualitative strain-size correlation

A qualitative correlation between average quantum dot size, as extracted from Raman measurement and the effective lattice compressive strain deduced from XRD measurement can be drawn. The progressively decreasing trend of InAs-rich islands or SML-QDs with decreasing sub-monolayer coverage can be described as a consequence of the increasing degree of in-plane compressive stress acting on the local strain centers. The accumulated compressive strain can control further evolution of surrounding islands by constricting the adatom (In)

diffusion through the matrix owing to enhanced potential barrier [29]. This, in turn, reduces the average size of the grown islands. E. Penev et al have previously reported such strain-controlled kinetic evolution of uniform island growth, purely based on density functional theory (DFT) framework [25]. Similarly, while depositing InAs in GaAs matrix, the resulting excessive compressive strain due to lattice misfit between InAs and GaAs accumulated near the islands (strain centres) hinders adatom (In) migration throughout the host matrix. Subsequently, it diminishes In adatom concentration at the nucleation sites, thus retards the adjacent islands from further growing up in size [26]. The monotonically increasing degree of compressive strain with decreasing SML coverage (0.8-0.4 ML) thus essentially gives rise to a more homogeneous distribution of progressively small size, isolated InAs islands [27]. Greater relaxation of strain energy with increasing SML coverage basically leads to weaker control over the island evolution which essentially attributes to the growth of closely-spaced high density bigger islands with lower size uniformity [13], as deduced from AFM measurements. With decreasing SML coverage, the increasing effect of built-in strain upon the size and morphology of the grown InAs islands is schematically shown in Fig.5.6.

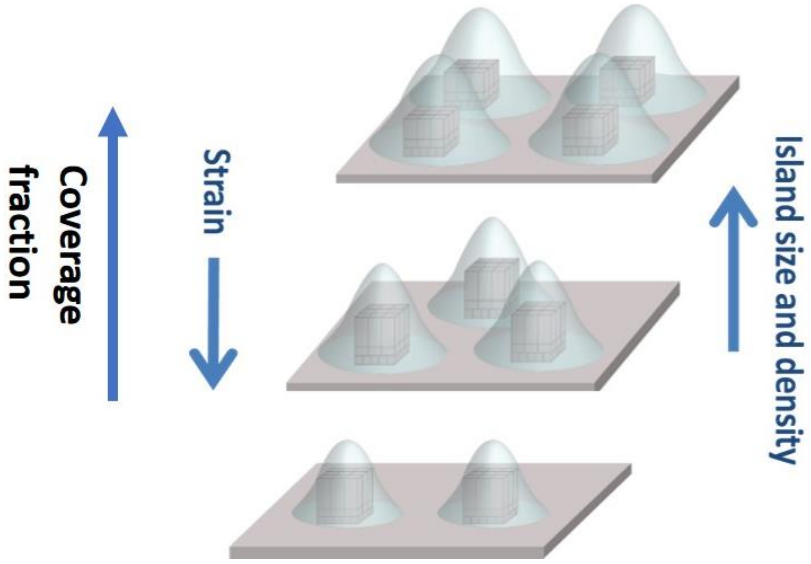

Fig.5.6 *Schematic representation of the effect of hydrostatic strain upon the growth of InAs islands for different InAs SML coverage. With decreasing InAs layer coverage, the locally accumulated compressive strain gradually increases which leads to small-size scattered isolated well-separated islands with less number density.*

5.2.6 Measurements of in-plane dot-to-dot separation from GISAXS study

The in-plane spatial arrangement and average lateral separation of the embedded SML-QDs have been quantitatively analyzed by grazing-incidence small-angle scattering (GISAXS) measurements. The samples were irradiated by x-ray originated from synchrotron source. The relative variation in the associated feature as a function of sub-monolayer coverage has been discussed in this section.

The in-plane information about a point along different azimuthal directions has been obtained by collecting the scattered x-ray intensity while rotating each sample around the surface normal from -15° to 115°, as schematically illustrated in Fig.5.7. The rotation angle 0° is set to align

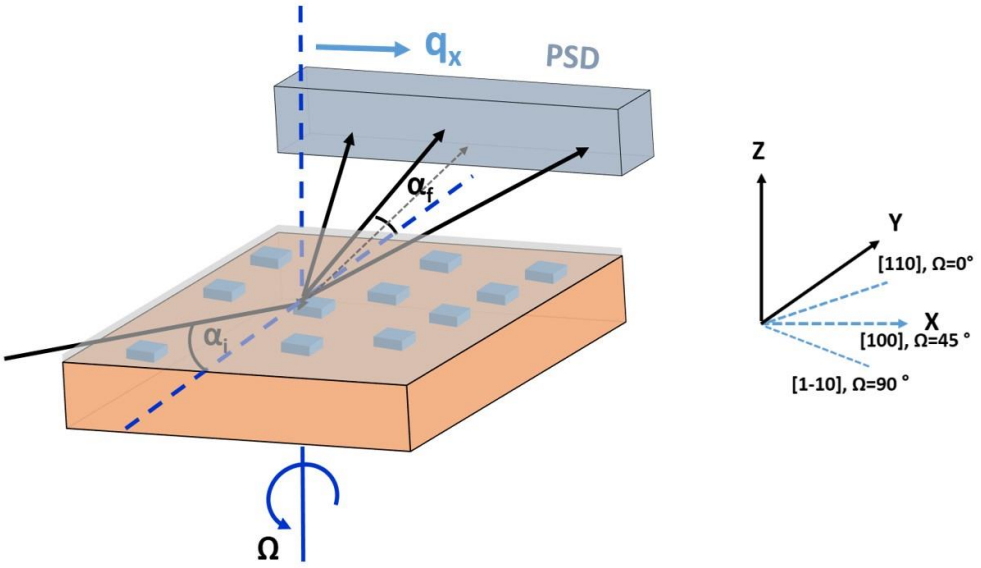

Fig.5.7 *Schematic illustration of the scattering geometry in GISAXS experiment. The scattered small-angle near-specular intensity is recorded by a linear PSD as a function of q_x. The angle of incidence (α_i = 0.14°) of the x-ray beam is set to a value close to the critical angle (α_c =0.16°) of total external reflection. Different azimuthal directions on the sample surface can be scanned by rotating the sample surface about the sample surface normal by angle Ω.*

to [110] azimuthal direction. The scattered x-ray intensity along the x-direction is collected by a position-sensitive detector (PSD) and the extracted I-q_x GISAXS peak profile is depicted in Fig.5.8 (a)-(e). The GISAXS profile for each of the samples vividly depicts the appearance of satellite peaks corresponding to the non-specular scattering from embedded SML-QDs symmetrically oriented about the central (q_x=0°) specular peak. Three distinct sets of GISAXS

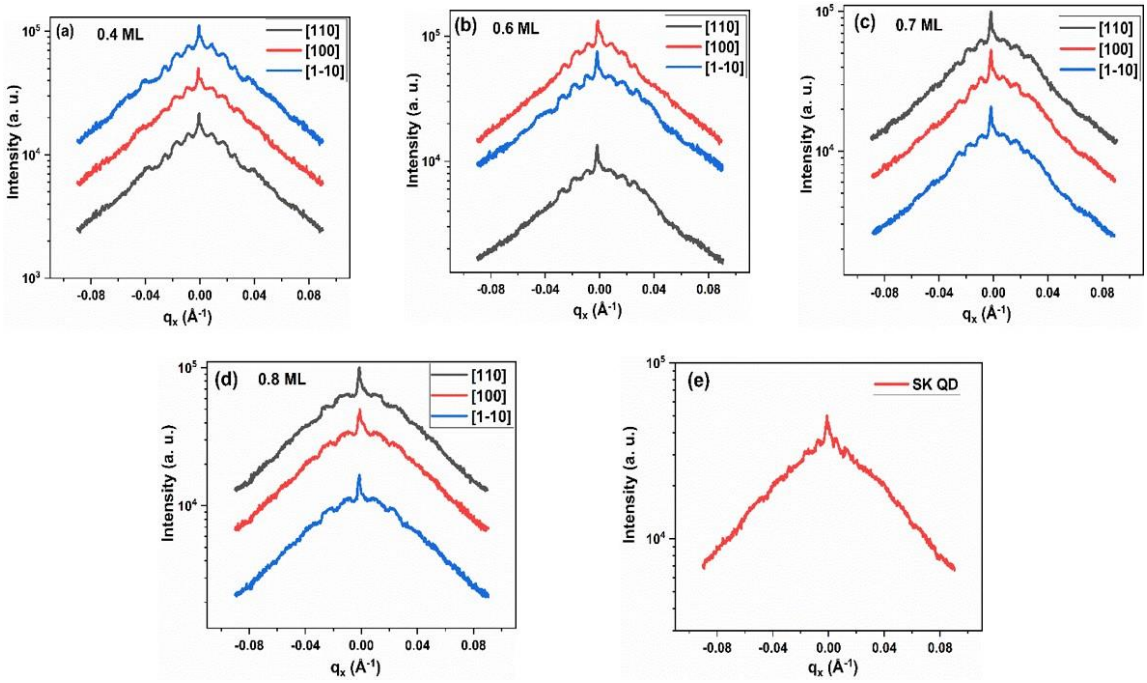

Fig.5.8 *The scattered x-ray intensities from the embedded InAs QDs measured along q_x in different azimuthal sample orientations. The peaks on both sides of the central 0^{th} order peak at $q_x = 0$ A^{-1} peak are the satellite peaks. Moreover, the satellite peaks are almost absent for x-ray scattering from SK-QD.*

profiling have been performed corresponding to 0°[110], 45°[100] and 90°[1-10] azimuthal directions. The appearance of well-resolved satellite peaks after de-convoluting them by standard weighted Lorentzian line-shape with suitable instrumental resolution function [1], indicates some sort of in-plane regular ordering in the spatial arrangement of the embedded quantum dot structures [28]. The characteristic length scale (L_b) related to the periodicity of the arrangement has been determined by the relation $L_b \sim 2\pi/\Delta q_x$ where Δq_x is the separation between 0^{th} order specular peak and de-convoluted 1^{st} order satellite peak, directly measured from the respective I-q_x profile [29-30]. This length scale corresponds to the average inter-dot lateral separation. The measured average dot-dot separation along the mentioned three azimuthal directions from different sub-monolayer coverage (0.4-0.8 ML) are enlisted in Table-5.3. Evidently, the average inter-dot separation decreases with increasing SML coverage. The well-separated higher-order satellite peaks with progressively greater separation from the 0^{th} order peak also manifest more closely spaced spatial distribution of SML-QDs at

Table 5.3 ***GISAXS results: Dot-dot separation along different lateral directions***

InAs coverage (ML)	Azimuthal orientation	Average dot-dot Separation L_Ω (nm)	Correlation length L_C (nm)
0.4	[110] [100] [1-10]	85±5 98±5.2 87±4.4	127±8.8 148±9.8 115±8.9
0.6	[110] [100] [1-10]	68±5 71±4.4 75±5.1	95±5 112±10.2 98±9
0.7	[110] [100] [1-10]	47±4.2 43±1.4 44.7±2.1	52±8.5 49±5.4 55±6.4
0.8	[110] [100] [1-10]	39±4.9 40±1 37.5±2.3	44±6 47±6 41±6
SK	[100]	105±6.7	

higher InAs coverage. Notably, the inter-dot average separation for reference InAs SK-QD has been found to quite larger as compared to InAs SML QD samples, mainly attributed to one order higher density of QDs [31]. The variation in measured satellite peak FWHM for different SML coverage reflects a different type of short-range periodicity in the in-plane spatial arrangement of the QD ensemble. This may have been attributed to the local variation of some planner properties in the vicinity of each QDs, leading to a coherent broadening of the non-specularly scattering peaks [31]. This is represented by a correlation length L_c, manifesting the spatial range of local in-plane ordering of dots. The corresponding correlation length have been quantitatively determined by using the relation $L_c \sim 2\pi/\Delta$ where Δ is the measured instrument-corrected FWHM of the 1st order satellite peak [32]. The calculated correlation lengths along

different azimuthal scanning directions for different SML coverage (0.4-0.8 ML) are listed in Table-5.3. Evidently, the correction length has been found to increase with decreasing SML coverage which indicates a higher range of existing lateral ordering of QDs. The appearance of a greater number of prominent higher-order satellite peaks is also a sign of a greater degree of QD correlation for low InAs coverage fraction. The higher-order satellite peaks flatten out for higher SML coverage (0.7-0.8 ML) which is an indication of a more limited range of lateral QD correlation. The standard deviation (SD) associated with the measured inter-dot average separation has been evaluated for different lateral directions. The estimated SD of 20% along [100] azimuth has been found to be lower than the SD of 29% along other directions for 0.4 ML coverage. This indicates a relatively more uniform spatial ordering of dots along [100] direction for 0.4 ML coverage [29]. This also suggests the markedly anisotropic distribution of average QD separation. The quantum dot distribution becomes more azimuthally randomized with increasing the SML coverage, as is reflected in evaluated SD of the mean inter-dot separation enhanced up to ~40% at 0.8 ML. Noticeably, the difference in magnitude of average dot-to-dot separation along different azimuthal directions progressively decreases with increasing InAs SML coverage which indicates a more isotropic in-plane distribution of embedded quantum dots.

5.3 Optical characterization

The optical properties, carrier confinement effect and carrier localization in the SML-QD based heterostructure have been investigated by low-temperature photoluminescence measurements. The relative variation of characteristic optical properties for different sub-monolayer coverage has been discussed in this chapter in detail.

5.3.1 Low-temperature PL study

The carrier confinement inside the sub-monolayer quantum dots and the modified excitonic binding energy under quantum confinement have been quantitatively analysed by low-temperature photoluminescence (PL) spectroscopy. The PL measurements of the SML-QDs with different coverage fraction (0.4-0.8 ML) have been performed at 4K, as depicted in Fig.5.9 (a). A sharp and strong luminescence has been observed from all the samples originated from a ground state Wannier excitonic transitions between confined states in quantum dots [33]. This is mediated by radiative recombination between an electron (e) and a heavy hole (hh) pair [34]. The PL peak energy exhibits blueshift from 1.406 eV to 1.496 eV with decreasing InAs sub-monolayer coverage from 0.8 ML to 0.4 ML, as depicted in Fig.5.9 (b). The increasing degree of QD size inhomogeneity [34-35] with increasing sub-monolayer coverage is reflected in progressively increasing PL linewidth, as graphically shown in Fig. 5.9 (b). This is quite similar to the increasing trend of Raman extracted QD size dispersion.

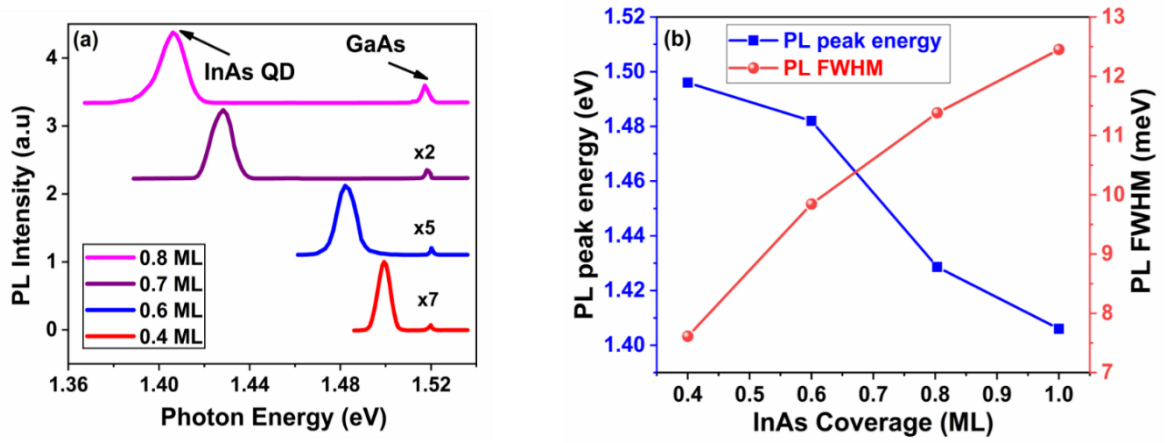

Fig.5.9 (a) Low temperature (4 K) normalized PL spectra of SML-QD heterostructure for different InAs coverage (0.4-0.8 ML). The PL peak at ~1.52 eV is related to the inter-band transition in GaAs layers which are represented magnified. (b) Variation of QD-related PL peak energy and FWHM with InAs coverage fraction.

5.3.2 Carrier confinement and excitonic binding energy

Photoluminescence peak energies are evaluated by de-convoluting the respective peak by standard Gaussian fitting functions with reduced χ^2 value of the order of 10^{-4}. The electron and

hole confinement energies (ΔE_C and ΔE_V) are calculated by using the variational method under envelope-function approximation [36,40]. The SML-QDs with characteristically low height to diameter ratio has been quiet justifiably approximated as quasi-two-dimensional 'lens-like' structures [37]. Thus, an array of laterally coupled SML-QDs can be simplistically represented as a series of cylindrical potential wells with very small height to base diameter ratio, separated by finite potential barriers [38-40]. The measured quantum dot height and diameter for different coverage fraction are fed into the model. The estimated quantum confinement energy (ΔE_C+ΔE_V) is enlisted in Table-5.4 which clearly suggests an increasing trend of confinement energy with decreasing sub-monolayer coverage. This has led to the observed blueshift in PL peak energy with decreasing InAs sub-monolayer coverage. Both quantum confinement and strain have played a vital role to determine the peak emission energy, as given by

$$E_g = E_{InAs} + \Delta E_C + \Delta E_V + \Delta E_{strain} \quad (5.3.2.1)$$

where E_g is the smallest energy difference between the electron and heavy-hole state, modified due to the combined effect of strain and confinement [41]. The correction in the electronic transition energy due to the compressive strain ($\varepsilon_{\parallel}$) is incorporated by the term ΔE_{strain}, which has been estimated for different SML coverages by using the relation [47]

$$\Delta E_{Strain} = -2a\frac{C_{11} - C_{12}}{C_{11}}\varepsilon_{\parallel} \quad (5.3.2.2)$$

where a=6.058 Å is the lattice constant of bulk InAs. This has led to a redshift in PL peak energy [40]. The corresponding estimated values are enlisted in Table-5.4. E_{InAs} =0.43 eV is the bandgap energy of bulk InAs at 4K [40]. The effective mass of the electron and heavy hole under InAs QD confinement, used in the energy calculation are $m_e^*=0.026m_0$ and $m_h^*=0.41m_0$ respectively [42]. The energy gap E_g has been estimated to be 1.51 eV, 1.49 eV, 1.44 eV and 1.41 eV for 0.4 ML, 0.6 ML, 0.7 ML and 0.8 ML respectively. Evidently, the combined effect

of quantum confinement and strain has led to the enhancement of the energy gap with a reduction in sub-monolayer coverage.

Table-5.4 ***Determined energy shift due to strain and quantum confinement***

InAs coverage (ML)	**PL peak energy (eV)**	**PL redshift Due to strain ΔE_{strain} (meV)**	**Calculated confinement energy ΔE_{con} (meV)**
0.4	1.496±4x10^{-4}	-2.3±0.07	1074±12
0.6	1.482±3x10^{-4}	-2.1±0.09	928±9.5
0.7	1.430±9x10^{-4}	-2±0.03	865±10.3
0.8	1.406±5x10^{-4}	-1.4±0.06	676±6.9

5.3.3 Excitonic binding energy and exciton dimension

The binding energy of the electron-hole pair in the bound excitonic state is approximately evaluated by using the relation

$$E_b = E_g - E_{PL} \qquad (5.3.3.1)$$

where E_{PL} is the observed PL transition energy, as enlisted in Table-5.5 [41]. Evidently, the energy of the e-hh bound state increases with decreasing coverage fraction which is attributed to enhanced Coulomb energy due to reduced e-h separation mediated by decreasing QD dimension along the direction of spatial confinement.

The associated excitonic Bohr radius a_B^* is evaluated by using the relation

$$E_B = \hbar^2/2\mu {a_B^*}^2 \qquad (5.3.3.2)$$

where $\mu = m_e^* m_h^*/(m_e^* + m_h^*)$ is the excitonic mass. This is a measure of the effective physical dimension of the e-hh pair bound state in the presence of active quantum confinement. The

confinement-induced excitonic radius as listed in Table-5.5, have been found to be smaller than the bulk InAs Bohr radius a_0~34 nm [43] and further monotonically decreases with decreasing sub-monolayer coverage. The enhancement of the measured exciton binding energy (BE) with monotonically reduced average QD size (1.4-2.3 nm), much less than the bulk Bohr radius (~34 nm) is in good agreement with Hribrank's model of potential well thickness-dependent excitonic BE in quantum well structure [44]. The deviation in exciton radius from its bulk value due to the effect of spatial confinement is more directly characterized by lowering exciton dimension relative to the bulk, as empirically given by

$$a_B^* = \frac{a_0}{2\sqrt{D}} \qquad (5.3.3.3)$$

where D is the excitonic dimensionality constant. The dimensionality constant varies from 0.25 to 1 when the exciton is lowered from three-dimension to two-dimension. The calculated D values (shown in Table-5.5) have been found to increase from 0.4 to 0.92 as InAs sub-monolayer is reduced from 0.8 ML to 0.4 ML. Evidently, the excitonic properties are shifting more toward the 2D-like nature from 3D bulk characteristics with decreasing coverage fraction as a consequence of stronger confinement induced progressively increasing binding energy.

Table-5.5 ***Evaluated exciton BE and effective Bohr radius***

InAs coverage (ML)	**Excitonic BE E_b (meV)**	**Excitonic Bohr radius (nm)**	**Dimensionality Constant (D)**
0.4	11.4±0.03	16.2±0.09	0.92±0.006
0.6	8.3±0.04	17.4±0.10	0.8±0.004
0.7	6.13±0.07	20.2±0.16	0.6±0.009
0.8	4.4±0.05	24.7±0.14	0.4±0.004

5.4 Summary

In this chapter, we have discussed molecular beam epitaxial growth of InAs/GaAs sub-monolayer quantum dot multi-stack heterostructure and their combined strain, structural and optical characterization. We have demonstrated the feasibility of spectrally tuning their excitonic photoemission in the near-IR region by controlling InAs sub-monolayer coverage from 0.4 to 0.8 ML. Through systematic high-resolution x-ray diffraction, Raman scattering and low-temperature photoluminescence measurement, we have explicitly discussed the variation in spectral properties with varying InAs coverage, as a consequence of the different degree of the quantum size effect. The progressive spectral blueshift with InAs coverage has been attributed to the increasing degree of carrier confinement due to smaller quantum dot size. We have observed that the built-in compressive surface stress due to lattice misfit between InAs and GaAs layer increases with decreasing SML coverage which helps to control the quantum dot growth and plays a leading role to determine their density and size distribution for different InAs sub-monolayer coverage. The reduction of layer coverage in the sub-monolayer domain has induced a reduction in QD size and number density.

With progressively increasing quantum confinement effect, the strength of exciton-phonon interaction is subjected to increase which can play a serious impact on the PL spectra at higher temperatures. Therefore, the temperature variation of PL spectra becomes very important to study as a function of SML coverage which is discussed in the following chapter.

5.5 Bibliography

[1] S C Jainyz, M Willanderx, and H Maesy, Semicond. Sci. Technol.**11** (1996) 641–671.

[2] J. F. Chen, P. Y. Wang, J. S. Wang, N. C. Chen, X. J. Guo, and Y. F. Chen, J. Appl. Phys. **87** (2000) 1251.

[3] J. Ibanez, A. Patane, M. Henini, and L. Eaves, Appl. Phys. Lett. **83** (2003) 15.

[4] S.C. Jain, M. Willander, and H. Maes, Semicond. Sci. Technol. **11** (1996) 641.

[5] Yu. A. Pusep, G. Zanelatto, S. W. da Silva, J. C. Galzerani, P. P. Gonzalez-Borrero, A. I. Toropov and P. Basmaji, Phys. Rev. B **58** (1998) 4.

[6] J. Ibanez, A. Patane, M. Henini, and L. Eaves, Appl. Phys. Lett. **83** (2003) 15.

[7] Y. I. Mazur, Z.M. Wang, G.J. Salamo, V. V Strelchuk, V.P. Kladko, V.F. Machulin, M.Y. Valakh, M.O. Manasreh, J. Appl. Phys. **99** (2006) 23517.

[8] J. Ibáñez, A. Patanè, M. Henini, L. Eaves, S. Hernandez, R. Cusco, L. Artús, Y.G.G. Musikhin, P.N. Brounkov, Appl. Phys. Lett. **83** (2003) 3069–3071.

[9] D. A. Tenne, A. G. Milekhin, A. K. Bakarov, O. R. Bajutova, V. A. Haisler, A. I. Toropov, S. Schulze and D. R. T. Zahn, Mat. Res. Soc. Symp. Proc. **737** (2003) 81.

[10] L. Artús, R. Cuscó, S. Hernández, A. Patanè, A. Polimeni, M. Henini and L. Eaves, Appl. Phys. Lett. **77** (2000) 3556.

[11] E. Giulotto, M. Geddo, M. S. Grandi, G. Guizzetti, G. Trevisi, L. Seravalli, P. Frigeri, and S. Franchi, Appl. Phys. Lett. **98** (2011) 111903.

[12] J. Groenen, R. Carles, G. Landa, C. Guerret-Piecourt , C. Fontaine and M. Gendry, Phys. Rev. B **58** (1998) 10452.

[13] W. J. Choia, H. Rho, J. D. Song, J. I. Lee, and Y. H. Cho, Physica E **26** (2005) 115–118.

[14] H. Rho, H. E. Jackson, S. Lee, M. Dobrowolska and J. K. Furdyna, Phys. Rev. B **61** (2000) 15641.

[15] R. Rao, A. M. Rao, B. Xu, J. Dong, S. Sharma, and M. K. Sunkara, J. Appl. Phys. **98** (2005) 094312.

[16] H. Richter, Z. P. Wang, and L. Ley, Solid State Commun. **39** (1981) 625.

[17] S. Mukherjee, A. Pradhan, T. Maitra, S. Mukherjee, A. Nayak, S. Bhunia, Advanced Material Letters **8** (2017) 891-896.

[18] Q. Xie, A. Madhukar, P. Chen, and N. P. Kobayashi, Phys. Rev. Lett.**75** (1995) 254.

[19] M. Grundmann, O. Stier and D. Bimberg, Phys. Rev. B **52** (1995) 11969.

[20] Z. D. Dohcevic-Mitrovic, M. J. S cepanovic, M. U. Grujic-Brojcin, Z. V. Popovic, S. B. Boskovic, B. M. Matovic , M. V. Zinkevich, F. Aldinger, Solid State Commun. **137** (2006) 387–390.

[21] Pengfei Qiao, Chien Yao Lu, Dieter Bimberg, and Shun Lien Chuang, Opt Express **21** (2013) 25.

[22] H. Campbell and P. M. Fauchet, Solid State Commun.**58** (1986) 739.

[23] Z. D. Dohcevic-Mitrovic, M. J. Scepanovic, M. U. Grujic-Brojcin , Z. V. Popovic, S. B. Boskovic, B. M. Matovic , M. V. Zinkevich, F. Aldinger, Solid State Commun.**137** (2006) 387–390.

[24] Todd D. Krauss and Frank W. Wise, Phys. Rev. B **55** (1997) 9860.

[25] E. Penev, P. Kratzer and M. Scheffler, Phys. Rev. B **64** (2001) 085401.

[26] P. Kratzer, E. Penev and M. Scheffler, Appl. Phys. A **75** (2002) 79.

[27] J. F. Chen, P. Y. Wang, J. S. Wang, N. C. Chen, X. J. Guo and Y. F. Chen, J. Appl. Phys. **87** (2000) 1251.

[28] Feng Wu, Jun Zhang, Shuai Wang, Hanling Long, Jiangnan Dai, Zhe Chuan Feng, Zheng Gong, and Changqing Chen, Opt Mater Express **5** (2015) 11.

[29] F. Hopfer, A. Mutig, M. Kuntz, G. Fiol, D. Bimberg, NN Ledentsov, VA Shchukin, SS Mikhrin, DL Livshits, IL Krestnikov, Appl. Phys. Lett. **89** (2006) 141106.

[30] Z. Xu, K. Leosson, D. Birkedal, V. Lyssenko, J. M. Hvam, J. Sadowski, Nanotechnology **14** (2003) 1259–1261.

[31] L. Krestnikov, M. Straßburg, M. Caesar, A. Hoffmann, U. W. Pohl, D. Bimberg, N. N. Ledentsov, P. S. Kop'ev, Zh. I. Alferov, D. Litvinov, A. Rosenauer, D. Gerthsen, Phys. Rev. B **60** (1999) 8695.

[32] S. Shetty, S. Adhikary, B. Tongbram, A. Ahmad, H. Ghadi, S. Chakrabarti, J. Lumin. **158** (2015) 1456.

[33] L. Krestnikov, N. N. Ledentsov, A. Hoffmann and D. Bimberg, Stat. Sol. (a). **183** (2001) 207.

[34] E. Assaid, E. Feddi, J. E. Khamkhami and F. Dujardin, J. Phys.: Condens. Matter **15** (2003) 175–184.

[35] G. Wang, S. Fafard, D. Leonard, J. E. Bowers, J. L. Merz, and P. M. Petroff, Appl. Phys. Lett. **64** (1994) 2815.

[36] S. S. Li, Y. Wang, J. Wang, and L. L. Chang, Phys Rev B Condens. Matter **54** (1996) 11575-11581.

[37] E. Rajaei and M. A. Borji, Int. J. Nanosci. Nanotechnol.**12** (2016) 45-53.

[38] S. Le Goff and B. Stebe, Phys. Rev. B **47** (1993) 2.

[39] H. Rodriguez and H.Y. Ramirez, Eur. Phys. J. B **66** (2008) 235–238.

[40] Shu-Shen Li, Jian-Bai Xia, Z. L. Yuan, and Z. Y. Xu, Phys. Rev. B **54** (1996) 16.

[41] Jun-Jie Shi, Solid State Commun. **124** (2002) 341–345.

[42] E. Rajaei and M. A. Borji, Int. J. Nanosci. Nanotechnol. **12** (2016) 45-53.

[43] K. Takei, H. Fang, S. Bala Kumar, R. Kapadia, Q. Gao, A. Javey, Nano Lett. **11** (2011) 5008–5012.

[44] Ľ. Hrivnák, J. Appl. Phys. **72** (1992) 3218.

[45] J. Brübach, J. E. M. Haverkort, J. H. Wolter and P. D. Wang, Mater Res Soc Symp Proc **406** (2011) 283.

[46] E. O. Gobel, H. Jung, J. Kuhl, and K. Ploog, Phys. Rev. Lett. **51** (1983) 17.

[47] Hiromitsu Asai and Kunishige Oe, J. Appl. Phys. **54** (1983) 4.

Chapter 6

Study of photo-carrier escape mechanism in InAs/GaAs sub-monolayer quantum dots from temperature-dependent photoluminescence measurement

6.1 Introduction

The intensity of photoluminescence depends on the number of radiative recombination which is proportional to the free carrier population in excited electronic states. At elevated temperature, this population density depletes and redistributes in different energy states through different relaxation channels. This has a direct consequence to the variation in spectral properties. The processes of photocarrier relaxation can be significantly modified in the presence of discretized carrier states under quantum dot spatial confinement. We have analyzed the temperature-induced relaxation of photogenerated carriers for different InAs sub-monolayer coverage from temperature-dependent photoluminescence (TDPL) measurements. From the respective spectral analysis, the relative degree of energy relaxation through the confined states for different InAs coverage fraction has been studied by comparing the temperature dependence of PL peak integrated intensity, peak energy, and linewidth. A simulation study of photocarrier relaxation in the electronically coupled assembly of SML-QDs has been performed to describe different features of temperature-dependent photoluminescence as a function of InAs layer coverage. The experimental and simulation results are elaborately discussed in this chapter.

6.2 TDPL measurement: Experimental results

6.2.1 Temperature-induced quenching of PL intensity for different coverage fraction

Radiative recombination of the dissociated carriers gives rise to photoluminescence whose intensity is proportional to the number density of the dissociated excitons. In addition to that, another carrier relaxation mechanism becomes significant at higher temperatures due to non-radiative (NR) recombination mediated by thermal scattering of the confined carriers [1]. This gives rise to quenching of PL intensity with increasing temperature (shown in Fig.6.1), the

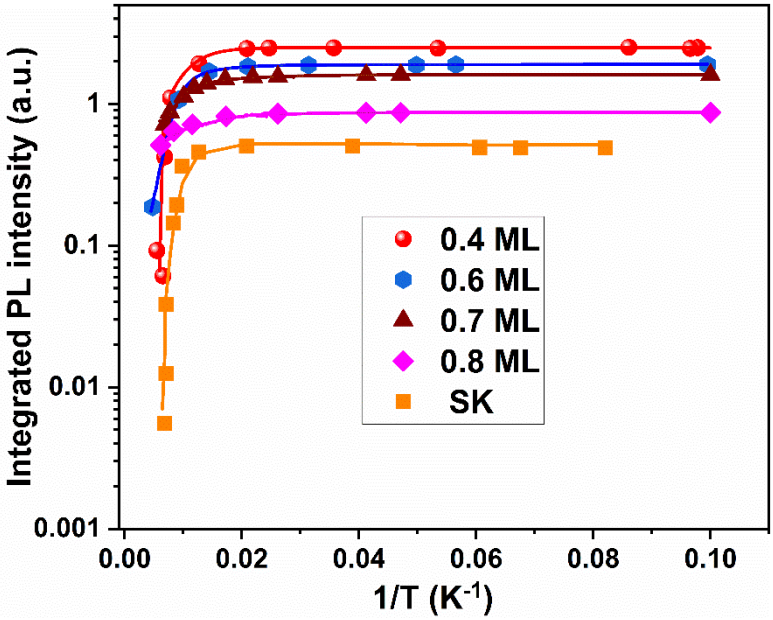

Fig.6.1 *Temperature variation of wavelength-integrated intensity (discrete points) and respective Arrhenius fits (solid lines; reduced $\chi^2 \sim 10^{-2}$) with double activation energy (E_{a1} and E_{a2}) related to two independent thermal carrier escape channels. The extracted lower thermal activation energies (E_{a1}) are 27±4.3, 51±5.4, 107±4.2 and 144±9.7 meV respectively for different (0.4-0.8 ML) InAs coverage. The relatively higher activation energy (E_{a2}) related to the second thermal escape channel has been extracted to be 235±4.5, 274±3.4, 252±5.6 and 305±5.3 meV for 0.4, 0.6, 0.7 and 0.8 ML.*

onset of which is quantitatively characterized by ground state thermal activation energy E_a. The activation energy is extracted by fitting the observed high-temperature variation of PL intensity (shown in Fig.6.1) by the standard Arrhenius relation for bi-channel thermal quenching [2]

$$I(T) = \frac{I_0}{1+A_1 \exp\left(-\frac{E_{a1}}{kT}\right)+A_2 \exp\left(-\frac{E_{a2}}{kT}\right)} \qquad (6.2.1)$$

where I_0 is the lowest temperature (4K) PL intensity, k is Boltzmann constant, E_a´s are the activation energies related to the corresponding thermal quenching channels and A´s are the associated weightage of the respective decay channels characteristically equivalent to the ratio of radiative to NR recombination lifetimes (τ_r/τ_{nr}) [3]. The fitting extracted values of A´s and activation energies are enlisted in Table-6.1. The activation energy associated with the stronger photocarrier quenching channel has been extracted to be E_{a1} ~43 meV, 65 meV, 120 meV and 155 meV for 0.4 ML, 0.6 ML, 0.7 ML and 0.8 ML coverage respectively. Their values are

apparently found to be coinciding (within the error bar) with the energy separation (E_{GaAs}-E_{QD}) of 39 meV, 50 meV, 100 meV and 140 meV between the respective excitonic ground state and GaAs barrier (1.52 eV) level. Therefore, the associated NR PL quenching channel can be readily described as an escape pathway of thermally excited confined carriers from QD excitonic ground state to the barrier (GaAs) continuum state with an energy equal to E_{a1} needed to surmount the potential barrier [2-4]. Evidently, extracted large value of A´s and monotonically decreasing activation energy with decreasing coverage fraction indicates relatively easier NR thermal escape of the confined carriers into the barrier [56]. This leads to a faster degree of quenching of PL intensity for lower sub-monolayer coverage (0.4-0.6 ML) initiated at a relatively lower temperature of 175 K-210 K, as shown in Fig.6.1 [5]. The thermal energy relaxation is mediated by exciton-phonon interaction with progressively increasing strength of coupling that may have been boosted by highly localized excitons and confined phonons inside QDs of decreasing size [6]. Stronger quantum confinement associated with the reduced QD size (at lower coverage) has decreased the potential offset (E_{GaAs}-E_{QD}) at the QD-barrier interface by uplifting QD electronic ground and thus has assisted easy direct NR transfer of carriers into the barrier. The relatively larger activation energy E_{a2} of 235±4.5, 274±3.4, 252±5.6 and 305±5.3 meV associated to the weaker quenching channel is more likely to be responsible for non-radiative thermal carrier transfer to some of the higher excited barrier states lying above the GaAs CB edge [7].

On the other hand, for higher InAs coverage fraction, fitting extracted relatively larger activation energy E_{a2} and lower value of τ_r/τ_{nr} manifest suppression of NR thermal carrier transfer and thus helps to maintain high luminescence efficiency $I(T)/I_0$ up to relatively higher temperature, as shown in Fig.6.1 [8]. For higher sub-monolayer coverage, reduction in quantum confinement (increasing dot size) leads to enhancement of barrier potential offset (E_{GaAs}-E_{QD})

that effectively constrict the thermal escape of the dissociated electrons from QD ground state by overcoming the potential barrier.

Table-6.1 ***Extracted parameters from Arrhenius fitting***

SML coverage (ML)	Calculated E_{GaAs}-E_{QD} (meV)	Thermal activation energy		PL Weightage constants	
		E_{a1} (meV)	E_{a2} (meV)	A_1	A_2
0.4	33±1.3	43±2	235±4.5	101390±113	214538±225
0.6	44±2.1	65±5	274±3.4	45544±98	189453±176
0.7	100±2.8	120±9	252±5.6	2460±25	245329±112
0.8	127±4.2	155±8	305±5.3	759±18	97890±127

6.2.2 Temperature dependence of spectral linewidth and energy redshift

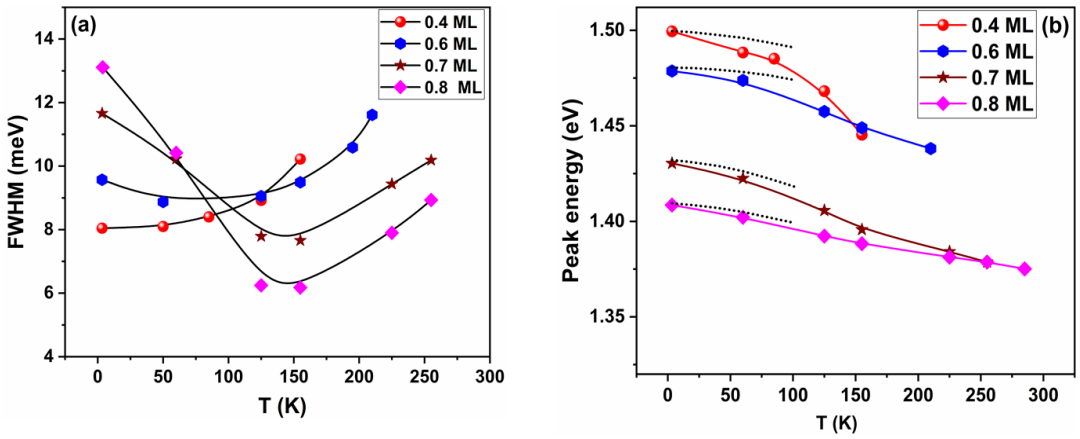

Fig.6.2 *(a) Temperature dependence of measured PL FWHM and (b) peak energy with corresponding Varshney fittings for different InAs coverage (0.4-0.8 ML).*

The redshift of PL peak energy has significantly slowed down at higher InAs coverage fraction, as clearly depicted in Fig.6.2 (a). Higher sub-monolayer coverage QD sample (0.7-0.8 ML) has also exhibited a monotonic reduction in PL linewidth with temperature up to 150 K (shown in Fig.6.2 (b)) which is anomalous in character as PL peak usually broadens due to enhanced degree of electron-phonon scattering under thermal excitation [9]. The relatively higher

thermal activation energy (E_{a1}), weakening of peak energy redshift and anomalous reduction in PL FWHM with the temperature at higher sub-monolayer coverage can be explained by considering an alternative non-thermal carrier relaxation pathway other than the thermal escape process, leading to faster quenching of PL intensity. Inter-dot tunneling of QD confined carriers through the intermediate GaAs barrier seem to be the most adequate direct loss-free process for photocarrier relaxation from confined states of one quantum dot to the energy states of the near-by dots without undergoing any NR thermal recombination [9]. For larger QDs (higher SML coverage), relatively loosely bound carriers (lower exciton BE) easily find an alternative escape pathway for tunneling among closely-spaced dots in GaAs matrix which is much more efficient than the thermal carrier escape process due to high surmounting potential barrier height [1]. The increasing rate of carrier tunneling with increasing sub-monolayer coverage due to progressively narrowing down of intermediate GaAs barrier thickness is more elaborately and quantitatively discussed in the next section.

Tunneling of carriers through the intermediated barrier is a two-step process mediated by two successive relaxation processes [1]. The dissociated carriers are firstly thermally excited from the excitonic ground state to the electronic ground state in QD conduction band followed by their escape from QD confinement and direct relaxation into the electronic (ground) states of the adjacent QDs with relatively lower in energy by quantum mechanical tunneling through finite barrier [9]. The strength of tunnel-induced carrier relaxation increases with decreasing effect of carrier localization (less excitonic BE) at higher coverage assists the dissociated photocarrier to effectively relax through a greater number of accessible electronic states over a longer spatial range without any absorption and recombination [10]. This leads to sustainable luminescence intensity up to high temperature (close to RT) as compared to the lower coverage QD samples. The anomalous reduction in PL linewidth and almost temperature-independent redshift of PL peak energy up to ~ 150K for higher coverage (0.7-0.8 ML), as shown in Fig.6.2

(a)-(b), can be described as a consequence of dominance of tunneling effect over the thermal carrier escape in the low-temperature region from 0K to 150K. The normal spectral broadening with increasing temperature, as exhibited by the lower coverage (0.4-0.6 ML) samples, is typically attributed to an increasing degree of accessible states for carrier relaxation through electron-phonon scattering. But at higher sub-monolayer coverage (0.7-0.8 ML), fast tunnel-induced inter-dot direct carrier transfer offers the opportunity for redistributing the dissociated carriers from all the adjacent QDs to preferably relax to some relatively lower energy states of the local QD distribution [9]. In other words, the greater strength of tunneling has led to a redistribution of carriers in the adjacent QD states before they could recombine within the QD confinement states or thermally escaped. This has given rise to an anomalous reduction in PL linewidth with temperature up to 150K for higher sub-monolayer coverage, as depicted in Fig.6.2 (a). The quantitative study of the time scales of tunneling and recombination is discussed in the next section in more detail. At higher temperature (T≥150K), NR thermal relaxation due to electron-phonon scattering takes over the tunnel-assisted inter-dot carrier transfer which leads to monotonically increasing normal thermal spectral broadening with temperature. The carrier relaxation at low temperature (≤ 150K) for higher InAs coverage (0.7-0.8 ML) is mainly controlled by the temperature-independent tunneling process. This is manifested in the consequent redshift of respective PL peak energy with very little temperature dependence up to 150 K, as depicted in Fig. 6.2 (b).

6.3 Analysis of photocarrier relaxation

The relative effect of carrier relaxation upon the temperature dependence of photoluminescence signal is discussed in this section which has been quantitatively analyzed through theoretical simulation by using a model equation of photo-carrier relaxation in the coupled system. The lifetimes related to radiative recombination and carrier tunneling have been extracted by fitting the respective TDPL spectra by the model equation and compared for different InAs coverage.

The ratio of characteristic lifetimes of these two relaxation processes has been found to determine the temperature dependence of spectral properties for different coverage fraction. All the fitting extracted lifetimes are also compared with a reference SK quantum dot sample.

6.3.1 Theoretical simulation of photo-carrier relaxation

The relaxation of QD confined photocarriers is generally mediated through various possible relaxation channels characterized by respective lifetimes [11]. The dissociated photo-generated carriers can either undergo direct recombination in quantum dot ground state or escape out of the QD confinement potential. The photocarrier escape is mediated either through the transfer of thermally excited carriers to GaAs medium by surmounting the QD-GaAs potential barrier offset or through direct relaxation of electrons from QD ground state to the electronic states of the adjacent dots by the process of quantum mechanical tunneling through the intermediate GaAs barrier [12-15]. The possible photocarrier relaxation routes are illustrated schematically in Fig.6.3. Here our objective is to study the temperature dependence of PL spectra under the

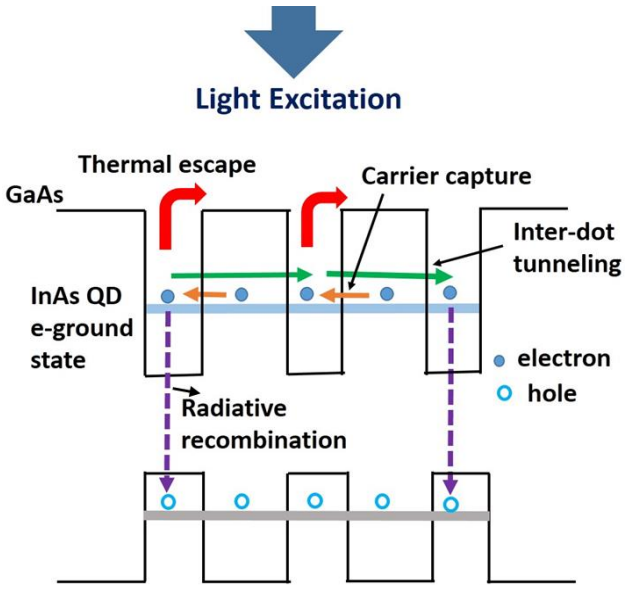

Fig.6.3 *Different relaxation channels for QD captured photo-carriers in laterally coupled QDs embedded in GaAs host matrix where the dots are treated as array of quantum wells separated GaAs potential barrier. The captured photo-generated carriers under QD confinement potential can recombine back to its ground state (violet line) or escape out of the QD. The carrier escape can be conveyed either by thermal transfer to the barrier (red line) or by non-dissipative transfer to the neighboring QD states by quantum mechanical tunneling (green line) through the intermediate GaAs barrier.*

combined effect of all these carrier relaxation processes, with quantitative determination of the associated lifetimes. There have been a few reports of studying the effect of carrier relaxation dynamics, but each of which is based on the separate study of each of the relaxation mode under very simplified structural model approximation [16-18]. In this thesis work, we have quantitatively analyzed the combined effects of the co-existing dynamical photocarrier relaxation processes through laterally coupled 'disc-shaped' two-dimensional SML-QD structure upon the TDPL spectra and described their relative variation in strength as a function of InAs sub-monolayer coverage [19].

The QD related excitonic PL spectra for different SML coverage (0.4-0.8 ML) at different temperatures in the range 5-285 K have been fitted by localized state function (LSF) model-based general photocarrier decay rate equation, as depicted in Fig.6.4. The mathematical framework of the LSF model, as first proposed by Xu et al, is based on adding up the rates of photocarrier transfer in different relaxation channels in and out of the QD ground state, over a Gaussian density of states [20]. The time variation of the confined carrier distribution function f(E, T) at temperature T in quantum dot ground state of energy E is expressed by the model rate equation as given by

$$\frac{\partial f(E,T)}{\partial t} = \frac{\rho_d(E)}{\tau_{cap}} - \frac{f(E,T)}{\tau_r} + \frac{\int_E^{\infty} \rho_d(q)dq}{\tau_t}\left(1 - \frac{f(E,T)}{\rho_d(E)}\right) - \frac{f(E,T)}{\tau_t}\int_{-\infty}^{E}\left[1 - \frac{f(q,T)}{\rho_d(q)}\right]dq - \frac{f(E,T)\exp\left[-\left(E_{b,w} - E\right)/k_bT\right]}{\tau_{th}} \quad (6.3.1.1)$$

Where $\rho_d(E) = \rho_0 \exp[(E - E_0)^2/2\delta^2]$ is the density of carrier states following a Gaussian distribution about an average energy E_0 with a bandwidth of δ [20]. The total QD density N_d is given by the term $\int \rho_d(E)dE$. The terms on the RHS of the equation represent rates of growing or decaying photocarrier density conveying to different relaxation channels. The 1st term represents the capture of photocarriers generated in the host GaAs matrix into the confined states of the QDs with a characteristic timescale of τ_{cap}. The 2nd term represents the reduction

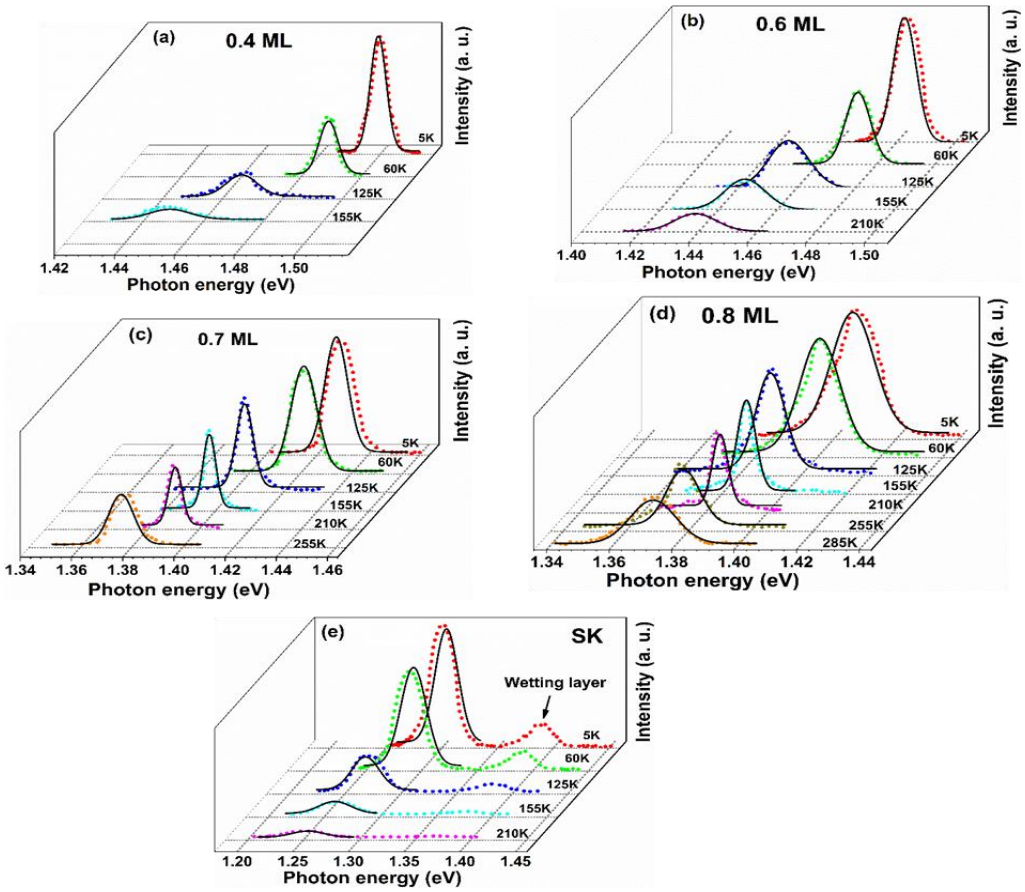

Fig.6.4 *PL spectra (dotted lines) of SML QDs for different InAs SML coverage (0.4-0.8 ML) and reference SK QD sample at different temperature (5-285 K). The solid lines are the respective fits by using standard LSF model carrier rate equation with reduced* $\chi^2 \sim (2x10^{-3}- 6x10^{-3})$*. The reference SK-QD sample exhibits an additional broadened PL peak at ~1.38 eV related to QD wetting layer electronic transition which is absent in PL spectra of SML-QDs.*

in carrier density due to the radiative recombination of carriers in quantum dot ground state with a characteristic lifetime of τ_r. The 3rd (4th) term describes tunneling of the confined carriers with characteristic lifetime of τ_t, into (out of) the ground state of energy E from (to) all energy states of the near-by QDs above (below) E. The 5th term describes escape of thermally excited carriers with a associated lifetime of τ_{th}, from quantum dot ground state (E) either into GaAs medium by surmounting an effective potential barrier of ~E_b-E or into the QD wetting layer states by overcoming a potential barrier offset of ~E_w-E. E_b and E_w are respectively the barrier state energy and wetting layer state energy. The thermal relaxation is conveyed only between the QD state and GaAs barrier states in SML-QDs, due to the absence of any wetting layer. On

the other hand, for conventional SK-QD, thermal relaxation to the wetting layer states becomes significant due to relatively lower potential offset across the QD-wetting layer interface. This, in turn, gives rise to an enhanced degree of photocarrier loss in the SK-QD system.

The PL intensity originated from radiative recombination of the carrier distribution f(E, T) in QD ground state is expressed as

$$I(E) = [C_{PL} \times f(E,T) \times \rho_d(E)]/\tau_r \qquad (6.3.1.2)$$

where C_{PL} is a fitting normalization factor. The experimental PL spectra at different temperatures (5-285K) are fitted by the functional equation (6.3.1.2) with a reduced χ^2 value of ~10^{-3}. The value of the fixed fitting parameters τ_{th}, N_d, $E_{B,}$ and E_w are enlisted in Table-6.2.

Table-6.2 ***Fixed and TDPL fitting extracted parameters***

Coverage (ML)	**Fixed parameters**					**Fitting extracted lifetimes (ps)**		
	τ_{th} (ps)	**E_b (eV)**	**E_w (eV)**	***N_d*** **($10^{10}cm^{-2}$) [12]**	**Thermal activation energy E_a (meV)**	**τ_{cap}**	**Γ_r**	**Γ_t**
0.4	10	1.52		2	43	30±3	172±20	1008±42
0.6				7.5	65	48±3	242±25	828±30
0.7				8.6	120	62±5	453±22	437±24
0.8				9.1	155	78±7	1125±45	350±28
SK QD (Ref)			1.38	8.9	32	93±8	1012±30	1328±38

The values of energy E_0, related to QD excitonic transition at different temperatures for different SML coverage are fed into the model equation (6.3.1.2) directly from the respective

PL spectra, as discussed in the previous chapter. The lifetimes of different carrier relaxation process τ_{cap}, τ_t and τ_r and FWHM σ of ground state energy distribution for different SML coverage are extracted from the model PL fitting which enlisted in Table-6.2. The thermal activation energies (E_{a1}) related to the dominant thermal carrier channel through the potential offset at the QD-GaAs barrier interface are directly taken from Table-6.1 and fed into the model equation (6.3.1.2) as an input parameter. The extracted tunneling lifetime τ_t and radiative recombination lifetime τ_r have been found to be almost temperature independent for all coverage fraction throughout the temperature range from 5K to 285K, except a small fluctuation about its average value, as shown in Fig.6.5. Therefore, quite justifiably, the

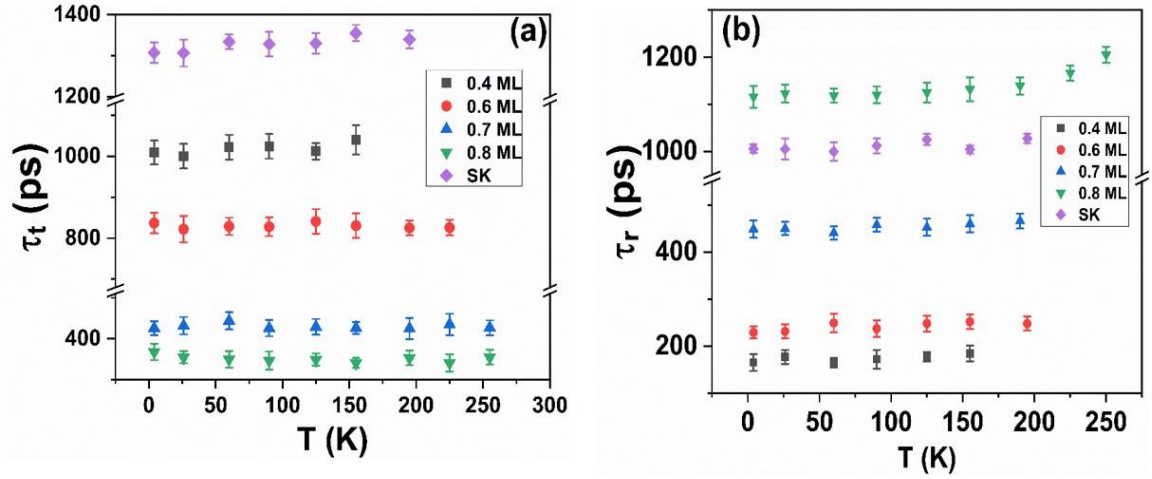

Fig.6.5 *Temperature variation of TDPL extracted (a) inter-dot carrier tunnel time τ_t and (b) carrier radiative recombination time τ_r and for different SML coverage (0.4-0.8 ML) along with the reference SK QD sample. Both the characteristic lifetime has been found to be fairly constant with temperature with a standard deviation of 1.3-3.2 % and 1-3.9 % relative to their respective mean values.*

extracted tunneling and recombination lifetimes are replaced by the corresponding temperature averaged values Γ_t and Γ_r [21]. In the rest of the discussion on the temperature dependence of PL spectra for different InAs sub-monolayer coverage, only these time-averaged lifetimes are considered. From the extracted lifetimes plotted with InAs coverage fraction (0.4-0.8 ML) in Fig.6.6, it is quite evident that with increasing the SML coverage, the (temperature) average tunnel time Γ_t decreases whereas the average radiative recombination lifetime Γ_r increases. More importantly, the ratio of recombination lifetime and tunnel lifetime Γ_r/Γ_t has exhibited an

increasing trend from 0.17 to 3.33 with increasing SML coverage from 0.4 to 0.8 ML. This suggests progressively increasing relative strength of inter-dot tunnel induced carrier escape process as compared to radiative recombination in quantum dot ground state. Noticeably, the value of Γ_r/Γ_t is less than unity at comparatively lower coverage (0.4-0.6 ML) which reflects the dominance of carrier recombination process over the tunneling strength. On the other hand, at relatively higher coverage (0.7-0.8 ML), the value of Γ_r/Γ_t greater than unity indicates that interdot tunneling strength takes over the carrier recombination rate.

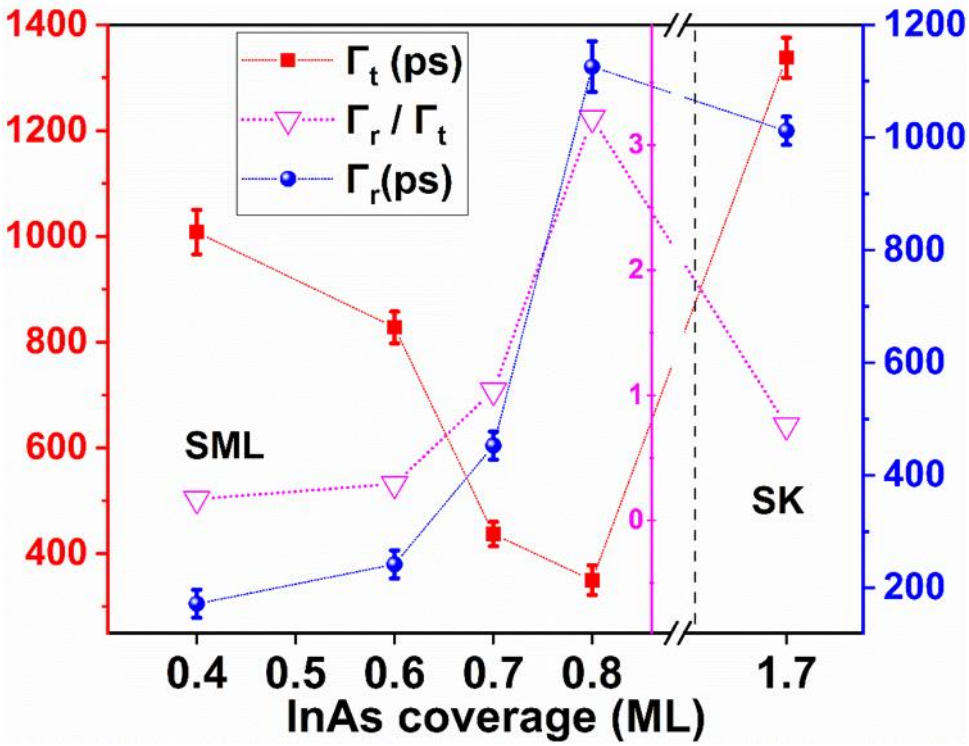

Fig.6.6 *Variation of temperature averaged Γ_t, Γ_r and Γ_r / Γ_t with InAs SML coverage (0.4-0.8 ML) along with reference SK QD grown with threshold coverage of 1.7 ML. Evidently, Γ_r and Γ_t have exhibited increasing and decreasing trend with increasing SML coverage whereas their ratio Γ_r/Γ_t undergoes gradual enhancement.*

Progressive reduction in quantum confinement with increasing InAs SML coverage, as previously discussed in the chapter-5, attributes to enhanced carrier recombination lifetime or alternatively decreases the rate of recombination [12,22].

For reference SK-QD, the associated tunnel and recombination lifetime have been extracted to be Γ_t =1328 ps and Γ_r =1012 ps. Evidently, the rate of tunneling in InAs/GaAs SML-QD system

is much faster than SK-QD owing to a more closely spaced distribution of QDs with a higher number density.

6.3.2 Dependence of tunnelling lifetime on InAs coverage

Dot-to-dot tunnelling through intermediate GaAs medium can be modelled as quantum mechanical carrier tunnelling among an array of potential wells separated by narrow barrier layers. The associated lifetime Γ_t^{WKB} for tunneling approximately follows the WKB relation [23], as given by

$$\Gamma_t^{WKB} \propto \exp(2L_b) \qquad (6.3.2.1)$$

where L_b is the barrier layer thickness. The model estimated tunnel time Γ_t^{WKB} is plotted as a function of SML coverage in Fig.6.7. The thickness of the intermediate GaAs layer or

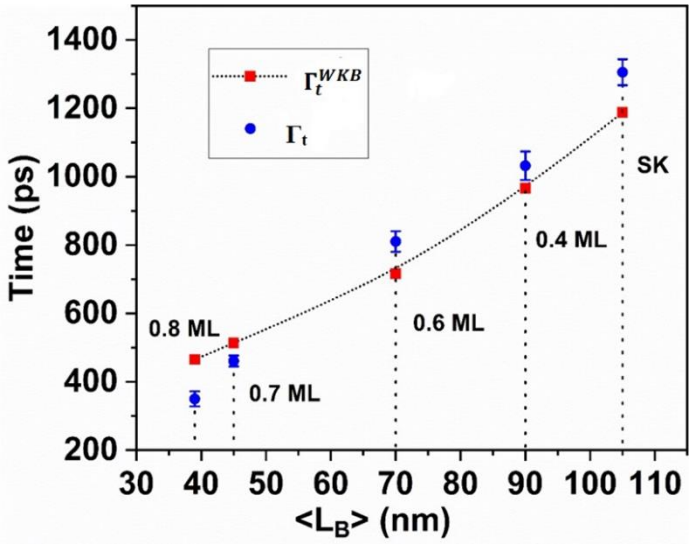

Fig.6.7 *Variation of TDPL extracted carrier tunnel time Γ_t and theoretically calculated inter-dot carrier tunnel time Γ_t^{WKB} with average inter-dot lateral separation $<L_B>$ related to different InAs SML coverage. Close agreement of their respective values justifies the co-relation between PL extracted fitting parameter Γ_t and average inter-dot separation L_B extracted from GISAXS measurements.*

alternatively the average dot-to-dot separation for different SML coverage are directly used from GISAXS measurements. The close agreement (apparat from a proportionality constant) of the model estimated and TDPL fitting extracted tunnel lifetimes, justifies our PL modeling.

This indicates that relatively closely-spaced laterally coupled distribution of QDs at higher SML coverage have mediated more efficient tunnel-induced carrier escape with shorter tunnel time than among well-separated QDs at lower coverage fraction. This is schematically illustrated in Fig.6.8. The larger tunnel time (Γ_t ~1328±38 ps) for the reference SK-QD sample in comparison with the InAs SML-QD sample is the consequence of existing large average inter-dot separation (105±6.7 nm), as evaluated from GISAXS measurements.

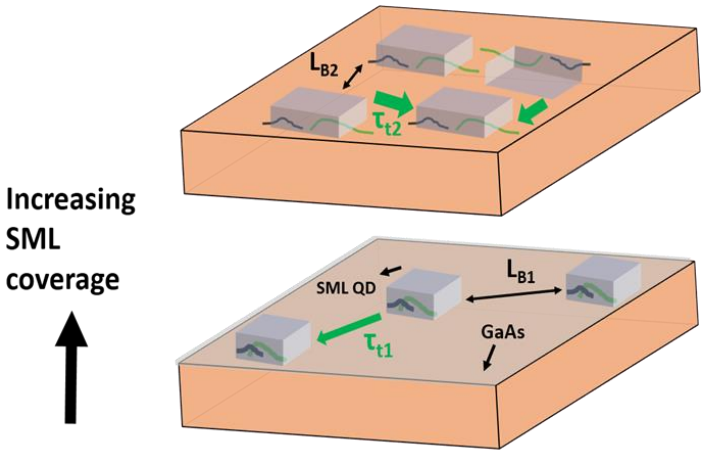

Fig.6.8 *A schematic representing the relative measure of different average inter-dot in-plane separation L_B and carrier tunneling time Γ_t as a function of InAs SML coverage. With increasing SML coverage, decreasing the degree of e-h wavefunction (green and black) overlap in QD ground state and a smaller value of L_B ($L_{B2} < L_{B1}$) is associated with a faster rate of inter-dot carrier tunneling ($\Gamma_{t2} < \Gamma_{t1}$).*

6.3.3 Average lifetime for photoluminescence quenching

The combined effects of co-existing independent processes like quantum dot recombination, inter-dot tunneling and thermal transfer of dissociated carriers to the continuous states of GaAs host matrix determine the overall rate at which PL signal quenches. The average steady-state lifetime τ_{PL}, related to the decay of the PL signal can be determined through the relation [24]

$$1/\tau_{PL} = 1/\Gamma_t + 1/\Gamma_r + \left(\frac{1}{\tau_{th}}\right) x\, exp\left[-\left(E_{b/w} - E_0\right)/k_b T\right] \qquad (6.3.3.1)$$

The evaluated PL decay time for different SML coverage and reference SK-QD sample are plotted with the operating temperature in the range from 5K to 285K, as shown in Fig.6.9 (a).

Evidently, PL decay time drops relatively sharply with increasing temperature for the SK-QD sample leading to rapid quenching of the PL intensity. The rate of quenching gets accelerated with increasing temperature. This has been attributed to significant direct thermal transfer of photogenerated carriers from QD confined states to the dissipating wetting layer states owing to low surmounting potential barrier E_w–E_0 across the QD-wetting layer interface [25]. On the other hand, the overall PL decay time for SML QDs remains almost constant with increasing temperature and thus effectively equivalent to some temperature averaged decay time Γ_{PL}. The temperature-independent and comparatively higher PL decay time than the SK-QD sample indicate a much weaker dissipative thermal relaxation process. Therefore, the photocarrier relaxation and temperature dependence of PL spectra in the SML-QD system are mainly controlled by the radiative recombination and inter-dot tunneling. Evidently, the (temperature) average overall PL decay time increases from 130 ps to 270 ps with increasing SML coverage from 0.4 ML to 0.8 ML, as shown in Fig.6.9 (b). Either of the carrier recombination and tunneling processes having a shorter lifetime, effectively determine the overall PL decay time Γ_{PL}. At low SML coverage (0.4-0.6 ML), recombination time (Γ_r), shorter than the tunneling lifetime (Γ_t) determines PL quenching which prompts confinement induced faster excitonic recombination in individual QD ground state before the photocarriers could tunnel to the carrier states of the next quantum dot [12]. On the other hand, at higher coverage fraction (0.7-0.8 ML), tunneling lifetime, shorter than the recombination lifetime prompts the confined photocarriers to relax to the carrier states of the adjacent QDs by tunneling through the GaAs barrier before they could recombine within the confinement potential of individual quantum dots [26]. The mutually counteractive effect leads to a monotonic rise in overall PL decay time with increasing SML coverage. It has been possible to achieve an inter-dot tunneling time as low as ~350 ps, significantly faster than the carrier recombination time of ~1125 ps by employing a laterally correlated array of SML QD at 0.8 ML InAs coverage. In conclusion, the

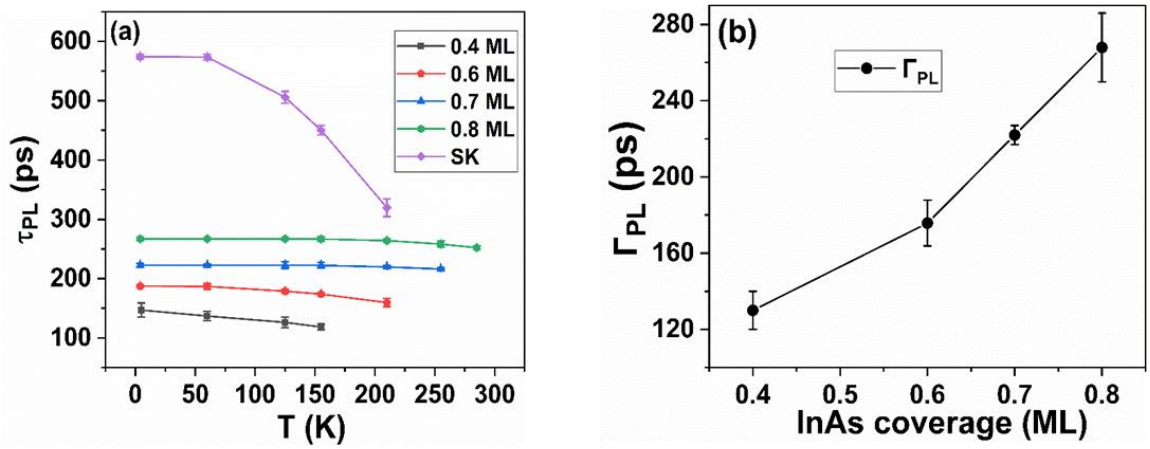

Fig.6.9 (a) Temperature variation of estimated steady-state total PL decay time τ_{PL} for different InAs SML coverage (0.4-0.8 ML) and the reference SK QD. Evidently, the PL intensity falls at a more accelerated rate for SK QD with temperature as compared to SML QDs. (b) The effective steady-state PL decay time increases with increasing InAs coverage.

absence of any wetting layer loss and efficient tunneling among very closely-spaced coupled embedded quantum dots, have assisted to effectively speed up carrier transfer through the heterostructure. This has given rise to the enhanced potentiality of keeping up photoluminescence intensity up to higher temperatures by employing SML-QDs with higher coverage fraction.

In comparison to the SML-QD system, the PL decay time (Γ_{PL}) is measured to be much shorter than the extracted tunnel time Γ_t (1328 ps) for SK-QD (reference sample). This indicates faster capturing to the confined photocarriers into the dissipative wetting layer states of the SK-QD system before they could tunnel to the carrier states of the near-by quantum dots [27].

6.3.4 Explanation of TDPL spectra in terms of carrier lifetimes

Temperature dependence of the PL parameters, like PL peak energy, FWHM and integrated intensity of the InAs sub-monolayer quantum dot-based heterostructure with varying coverage fraction are interpreted in the light of relative extracted timescales of mutually competing relaxation processes.

The temperature dependence of PL peak FWHM, peak energy and integrated intensity for different SML coverage (0.4-0.8 ML) are explicitly depicted in Fig.6.10 (a)-(c). The bandwidth (δ) of the ground state energy dispersion in their ground states for different SML coverage, as extracted from the respective TDPL fitting has been found to be in close agreement with the experimental PL peak FWHM, as shown in Fig.6.10 (a). The regular spectral broadening with

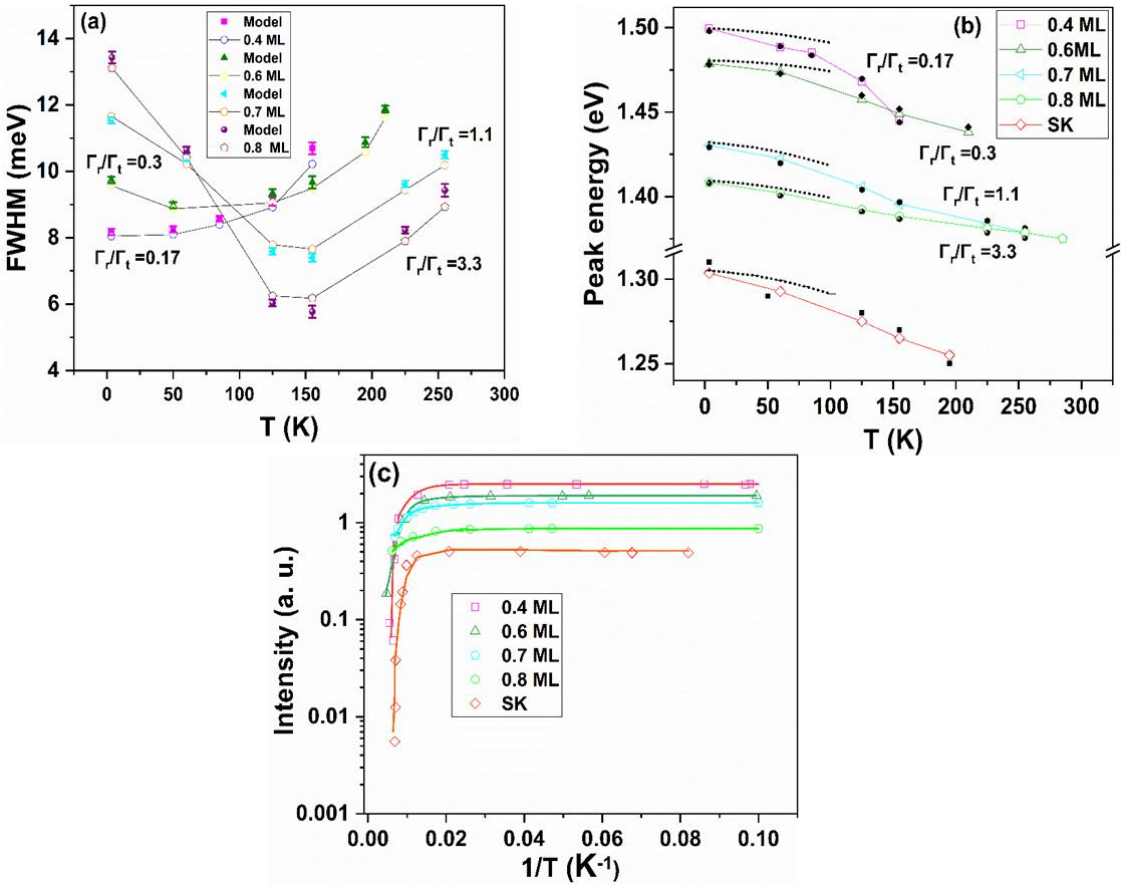

Fig.6.10 *(a) The variation of PL FWHM (unfilled dots) with temperature for different InAs SML coverage (0.4-0.8 ML) along with the FWHMs of the respective fitted PL lineshapes (solid dots) characterized by different values of the* Γ_r/Γ_t *ratio. At higher SML coverage (0.6-0.8 ML) PL linewidth showed an anomalous decrease with temperature in the range 5K to 150K associated with* $\Gamma_t < \Gamma_r$*. (b) The redshift of PL peak energy (unfilled dots) with temperature for different SML coverage along with respective fitted PL peak energies (filled dots) and Varshni's peak energy fitting curve (dotted lines). (c) Quenching of integrated model PL intensity (unfilled dots) with temperature along with respective Arrhenius fits (solid lines).*

increasing temperature, as exhibited in lower coverage (0.4-0.6 ML) sample, is due to dominant thermal relaxation to the continuous barrier states. This can be interpreted as a consequence of much longer tunnel lifetime Γ_t as compared to the overall PL decay time Γ_{PL} which causes

trapping of the photocarriers in the dissipative continuous barrier layer states before they could tunnel to the next QDs [28-29]. Moreover, lower recombination lifetime (Γ_r) than the tunnel time (Γ_t) also leads to faster recombination of the carriers in individual QD ground states before they could be transferred to the energy states of the adjacent QDs. This expedites PL quenching. On the other hand, for higher InAs coverage (0.7-0.8 ML), progressive reduction in PL FWHM with temperature in the range of 0K to 150K can be interpreted as a consequence of shorter tunneling time than recombination lifetime, as represented by value of Γ_r/Γ_t greater than unity (Γ_r/Γ_t ~1.1 and 3.3) [1,30]. This is attributed to faster inter-dot tunneling of carriers outplaying the phonon-aided escape into GaAs barrier in the low-temperature range (5-150K). The provision of efficient dot-to-dot tunneling induces preferred net photocarrier transfer to some local minimum energy states of the adjacent QDs [31]. This energy selective photocarrier relaxation gives rise to a reduction of range of carrier relaxation states which consequently leads to the anomalous reduction of PL linewidth with temperature. With further increase in temperature (>150K), the thermal scattering process again takes over other relaxation processes which leads to regular spectral broadening with temperature.

For lower coverage fraction (0.4-0.6 ML), the drastic redshift in PL peak energy with increasing temperature, as shown in Fig.6.10 (b) is reflected in much lower PL decay time (Γ_{PL}), mainly attributed to temperature-induced strong thermal scattering of confined photocarriers. On the other hand, for higher coverage fraction (0.7-0.8 ML), the rate of the redshift of PL peak energy with temperature reduces, which almost resembles the Varshni's curve for bulk InAs, as given by [32]

$$E_g(T) = E_g(0) - \frac{\alpha T^2}{\beta + T} \dots\dots\dots\dots\dots\dots\dots\dots\dots\dots\dots\dots\dots\dots\dots\dots\dots\dots\dots\dots\dots .. (6.3.4.1)$$

where E_g (T) is the temperature dependent bandgap, E_g (0) is the bandgap at the lowest temperature. The bulk bandgap E_g (0) of InAs at the lowest temperature (4 K) is 0.43 eV. This

is attributed to photocarrier escape by efficient tunnel-induced efficient non-thermal transfer of photocarriers, outplaying the phonon-assisted thermal relaxation. This is represented by associated shorter tunnel lifetime and longer PL decay time.

The relative quenching of integrated PL intensity with temperature (shown in Fig.6.10 (c)) for different SML coverage can be interpreted as the consequence of mutually interacting inter-dot tunneling, carrier recombination, and phonon-assisted thermal escape processes. The thermal activation energy E_a is evaluated by fitting the temperature variation of the respective model integrated PL intensity by standard Arrhenius relation, as elaborately disused in the previous sub-section 6.1.1 [33-34]. Evidently, the increasing value of E_a with increasing InAs SML coverage, as listed in Table-6.2, is a signature of existing higher luminescence efficiency sustainable up to higher temperature [35]. The luminescence from the 0.8 ML sample associated with activation energy as high as 155±8 eV, has been found to sustain up to 285 K. This is a consequence of dominance of tunnel-induced non-dissipative direct inter-dot carrier transfer strength over carrier recombination and thermal escape processes as reflected in higher value of Γ_r/Γ_t and overall PL decay time Γ_{PL}. The deduced PL decay time (Γ_{PL}) in the SK QD (reference sample) is found to be significantly lower than the SML-QD samples due to substantial thermal quenching of PL intensity at a relatively lower temperature, as represented by the lower activation energy of 32±5 meV.

6.4 Summary

In this chapter, the photo-carrier escape mechanism in an assembly of correlated self-assembled sub-monolayer InAs/GaAs quantum dots has been discussed as a function of InAs fractional coverage. The relative lifetime of excitonic recombination and inter-dot tunneling (Γ_r/Γ_t ~0.17-3.3), as extracted from a simulation of photocarrier relaxation rate in an electronically coupled system has been found to play the decisive role to determine the temperature variation of PL spectra. Progressively increasing rate of inter-dot tunneling relative to excitonic recombination

with increasing SML coverage as represent by increasing value of Γ_r/Γ_t, has given rise to high luminescence efficiency up to elevated temperature, more temperature stable emission energy and an anomalous decreasing trend of spectral linewidth with temperature (5-150K). Temperature independent carrier recombination and more efficient inter-dot transfer of photogenerated electrons in coupled SML-QD system offer more thermal stability than conventional SK QD which makes it more demanding for optoelectronic applications. Moreover, the different degrees of inter-dot carrier transit throughout the strongly correlated array of InAs/GaAs sub-monolayer quantum dots with varying layer coverage offers a further provision of engineering electric transport properties. In that respect, an electronic study as a function of spatial correlation may be clinical which can provide a more elemental picture of dot-dot carrier coupling and intricate energy relaxation process. This is discussed in the following chapter.

6.5 Bibliography

[1] Y Dai, G. Bailey, C. Kerestesl, David V. Forbesl and Seth M. Hubbard, IEEE 38th Photovoltaic Specialists Conference (2012) 000039-000044.

[2] L. Seravalli, G. Trevisi, P. Frigeri, S. Franchi, M. Geddo, G. Guizzetti, Nanotechnology **20** (2009) 275703.

[3] J. Krustok, H. Collan, K. Hjelt, J. Appl. Phys. **81** (1997) 1442–1445.

[4] T. Torchynska, J. Casas Espinola, L. Borkovska, S. Ostapenko, M. Dybiec, O. Polupan, N. Korsunska, A. Stintz, P. Eliseev, K. Malloy, J. Appl. Phys. **101** (2007) 024323.

[5] Jayita Patwari, Hemant Ghadi, Samim Sardar, Jashan Singhal, Binita Tongbram, Sanjib Shyamal, Chinmoy Bhattacharya, Subhananda Chakrabarti, Samir Kumar Pal, Mater Res Express **4** (2017) 016301.

[6] Todd D. Krauss and Frank W. Wise, Phys. Rev. B **55** (1997) 9860.

[7] S. Mazzucato, D. Nardin, M. Capizzi, A Polimeni, A Frova, L. Seravalli, S. Franchi, Mater. Sci. Eng. C. **25** (2005) 830–834.

[8] N. V Baidus, A. Chahboun, M.J.M. Gomes, M.I. Vasilevskiy, P.B. Demina, E.A. Uskova, B.N. Zvonkov, Appl. Phys. Lett. **87** (2005) 53109.

[9] X. L. Zhou, Y. Chen, H. Zhang, G. Zhou, T. Li, J. Q. Liu, X. Ye, J. Q. Liu and Z. G. Wang, J. Appl. Phys.**109** (2011) 083501.

[10] W. H. Chang, T. M. Hsu, C. C. Huang, S. L. Hsu, and C. Y. Lai, Phys. Rev. B **62** (2000) 2.

[11] E. Assaid, E. Feddi, J. E. Khamkhami and F. Dujardin, J. Phys.: Condens. Matter **15** (2003) 175–184.

[12] S. Mukherjee, A. Pradhan, S. Mukherje, T. Maitra, S. Sengupta, B. Satpati, S. Chakrabarti, A. Nayak, S. Bhunia, J of Luminescence **210,** (2019) 311-321.

[13] S. S. Li, J. B. Xia, Z. L. Yuan, and Z. Y. Xu, Phys. Rev. B **54** (1996) 16.

[14] E. Rajaei and M. A. Borji, Int. J. Nanosci. Nanotechnol.**12** (2016) 45-53.

[15] H. Van, E. Goovaerts and G. Borghs, Phys. Rev. B **46** (1992) 6982-6989.

[16] W. H. Chang, H. Lin, S. Y. Wang, C. H. Lin, S. J. Cheng, and M. C. Lee, Phys. Rev. B **77** (2008) 245314.

[17] P. W. Fry, J. J. Finley, L. R. Wilson, A. Lemaitre, D. J. Mowbray, M. S. Skolnik, M. Hopkinson, G. Hill, and J. C. Clark, Appl. Phys. Lett. **77** (2000) 4344.

[18] M. A. Kapteyn, F. Heinrichsdorff, O. Stier, R. Heitz, M. Grundmann, N. D. Zakharov, D. Bimberg, and P. Werner, Phys. Rev. B **60** (1999) 14265.

[19] Z. Y. Xu, Z. D. Lu, X. P. Yang, Z. L. Yuan, B. Z. Zheng, J. Z. Xu, W. K. Ge, Y. Wang and L. L. Chang, Phys. Rev. B **54** (1996) 11528.

[20] X L Zhou, Y H Chen, C. H. Jia, X. L. Ye, Bo Xu and Z. G. Wang, J. Phys. D: Appl. Phys. **43** (2010) 485102.

[21] G. Weng, S. Chen, B. Zhang, X. Hu, S. Kuboy, K. Onabe, Opt Express **25** (2017) 24745-24755.

[22] E. O. Gobel, H. Jung, J. Kuhl, and K. Ploog, Phys. Rev. Lett. **51** (1983) 17.

[23] S. Sanguinetti, M. Henini, M. Grassi Alessi, M. Capizzi, P. Frigeri, and S.Franchi, Phys. Rev. B **60** (1999) 8276.

[24] W. H. Chang, T. M. Hsu, C. C. Huang, S. L. Hsu, C. Y. Lai, N. T. Yeh, T. E. Nee and J. I. Chyi, Phys. Rev. B **62** (2000) 11.

[25] N Debbar, D Biswas and P Bhattacharya, Phys. Rev. B **40** (1989) 1058.

[26] S. Sanguinetti, M. Henini, M. Grassi Alessi, M. Capizzi, P. Frigeri, and S.Franchi, Phys. Rev. B **60** (1999) 8276.

[27] W.-H. Chang, T. M. Hsu, C. C. Huang, S. L. Hsu, C. Y. Lai, N. T. Yeh, T. E. Nee and J. I. Chyi, Phys. Rev. B **62** (2000) 11.

[28] M. B. Smirnov, V. G. Talalaev, B. V. Novikov, S. V. Sarangov, N. D. Zakharov, P. Werner, U. Gosele, J. W. Tomm, and G. E. Cirlin, Phys. Status Solidi B **247** (2010) 347–352.

[29] M. T. Man and H. S. Lee, Sci. Rep. **5** (2015) 8267.

[30] S. Muto, T. Inata, A. Tackeuchi, Y. Sugiyama, and T. Fujii, Appl. Phys. Lett. **58** (1991) 2393.

[31] Y. I. Mazur, X. Wang, Z. M. Wang, G. J. Salamo, M. Xiao and H. Kissel, Appl. Phys. Lett. **81** (2002) 13.

[32] X. Lu, J. Vaillancourt, and H. Wen, Appl. Phys. Lett. **96**, (2010) 173105.

[33] L. Seravalli, G. Trevisi, P. Frigeri, S. Franchi, M. Geddo, G. Guizzetti, Nanotechnology **20** (2009) 275703.

[34] J. Krustok, H. Collan, K. Hjelt, J. Appl. Phys. **81** (1997) 1442-1445.

[35] L. Krestnikov, N. N. Ledentsov, A. Hoffmann and D. Bimberg, Stat. Sol. (a). **183** (2001) 207.

Chapter 7

Photodetector application and carrier transport studies in laterally correlated quantum dot self-assembly

7.1 Introduction

The performance of quantum dot photodetector is mainly determined by the degree of free photocarrier extraction and their subsequent transport through laterally coupled embedded QDs. This chapter is devoted to such a study of photo-response properties of InAs/GaAs SML-QD based detector as a function of InAs sub-monolayer coverage through analysis of photocurrent (PC) spectra, both by experiment and simulation. The mutual competition between QD excitonic recombination and tunnel-assisted carrier transport plays a leading role to control the photoconduction dynamics which essentially describes the device performance. The relative magnitude of such dynamical carrier escape processes is fundamentally represented by the associated characteristic lifetime. This study is all about analyzing the relative time scale of carrier transport and bound state recombination in the photodetector. The details of it are discussed in this chapter.

7.2 Photodetector fabrication

For photodetector (PD) fabrication, two metal contacts are grown on top of the SML-QD based heterostructure. One Schottky and ohmic metal contacts have been grown by depositing Au and alloyed Au-Ge metal respectively by thermal evaporation technique. For ohmic contact fabrication, deposited Au-Ge sites have been annealed into the sample at 440°C. The schematic representation of the photodetector is shown in Fig.7.1.

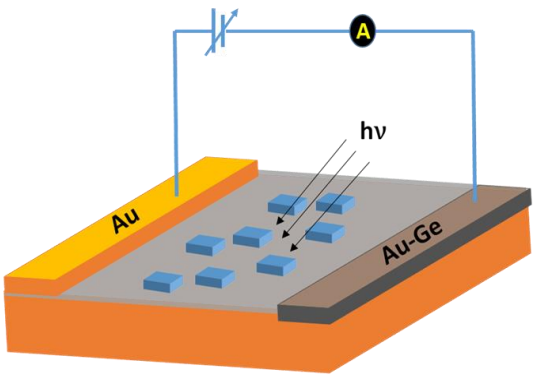

Fig.7.1 *Schematic representation of the fabricated photodetector device with two top metal contacts.*

7.3 Photocurrent analysis

The spectral photo-response, temperature and bias voltage-dependent steady-state and transient PC measurements of the QD-photodetector have been performed by using Keithley 4200 SCS and Tektronix TBS2102 digital storage oscilloscope (DSO). A 450W Xenon lamp in conjunction with a Gemini-180 monochromator has been employed as the monochromatic excitation source. The consecutive measurements are discussed in the following sub-sections.

7.3.1 Spectral photo-response

The resulting photocurrent (I_{ph}) has been recorded as a function of irradiating excitation wavelength in the range from UV to near-infrared under a fixed reverse bias of -2 V. The corresponding responsivity has been evaluated by using the relation $R=I_{ph}/PA$ where I_{ph} is the measured photocurrent, P is the power per unit illuminated area and A is the effective area of the detector's upper surface. The individual responsivity spectrum is recorded for different SML coverage at 80 K, as depicted in Fig.7.2. Evidently, all the spectrums exhibit well-defined

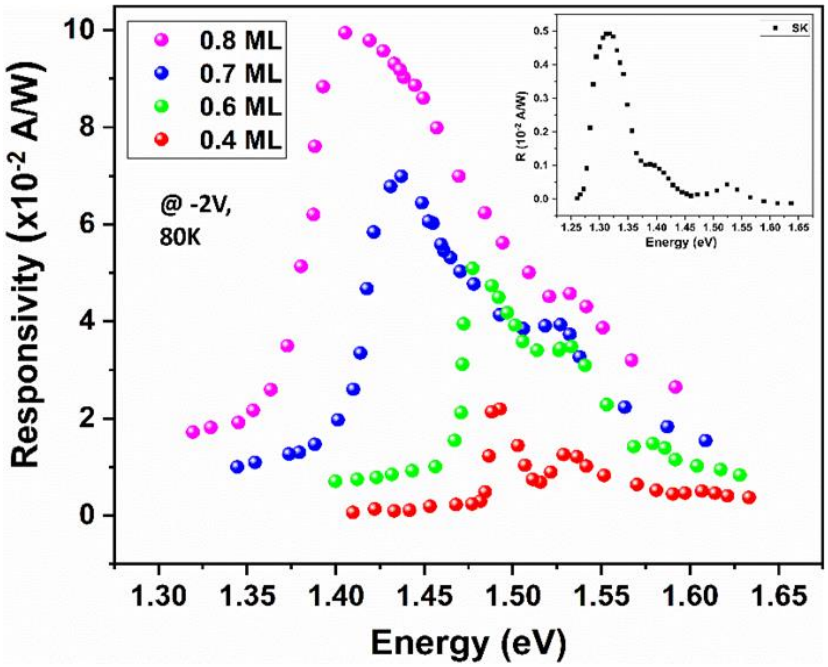

Fig.7.2 Near-infrared spectral photo-response for different SML coverage (0.4-0.8 ML) at 80K under -2V applied bias. Evidently the photo-response redshifts with increasing coverage fraction. Inset: Spectral response for the reference SK QD sample under the same conditions with a peak responsivity of 0.5x10^{-2} A/W.

near-infrared (NIR) photo-response peaked at 1.49 eV, 1.47 eV, 1.43 eV and 1.4 eV for 0.4 ML, 0.6 ML, 0.7 ML and 0.8-ML coverage respectively. The stronger responsivity peaks are attributed to quantum dot inter-band absorption which undergoes a progressive blueshift with decreasing InAs sub-monolayer coverage due to confinement induced enhanced bandgap [1]. The peak specific responsivity exhibits an increasing trend with increasing SML coverage. Noticeably, by employing SML-QDs, a twenty times higher responsivity than that of 0.5 mA/W corresponding to the reference SK QD, has been achieved at 0.8 ML. The comparatively weaker responsivity peak at ~ 1.51 eV is associated with the GaAs bandgap absorption [1].

7.3.2 Kinematic simulation of temperature-dependent photocurrent

The relative temperature dependence of the measured photo-current intensity for different SML coverage is depicted in normalized I_{ph} *-1/T* plots in Fig.7.3. The samples have been put in a He-cooled cryostat whose temperature has been controlled and varied in the range from 5 K to 250 K by using a temperature controller.

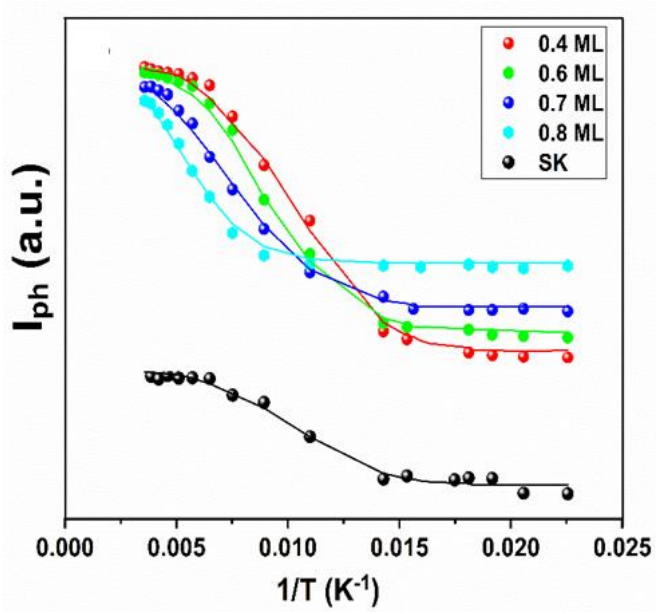

Fig.7.3 *(a) Temperature dependence of photocurrent for different SML coverage including the reference SK QD sample. The discrete dots and the solid lines are representing the experimental results and model fits respectively. In the low temperature (≤100K) regime, a higher coverage sample exhibits higher* I_{ph}*. In the temperature-controlled (100 ≤T ≤180K) region, lower coverage samples exhibit a more rapid rise in* I_{ph} *with increasing temperature. (b) Calculated photocarrier dissociation efficiency and photoconductive gain in arbitrary units for different SML coverage. Both of them were found to increase with coverage.*

The photocurrent across the two top electrodes is mediated by the transport of free electrons along a conduction channel through the lateral array of SML-QDs embedded in the GaAs matrix. The dissociated electrons in QD states are photoexcited to the conduction band from the valence band through near-infrared inter-band absorption [2]. Then the excited electron has two distinct choices, either it can be recaptured back into the ground state by recombining with a hole in the valance band or can escape the QD confinement potential. The possible carrier relaxation routes in the lateral array of QDs in between two semiconductor-metal junctions are schematically shown in an energy band representation as a function of distance from the carrier injecting junction Fig.7.4. The escape of photocarriers from the QD bound states is mediated

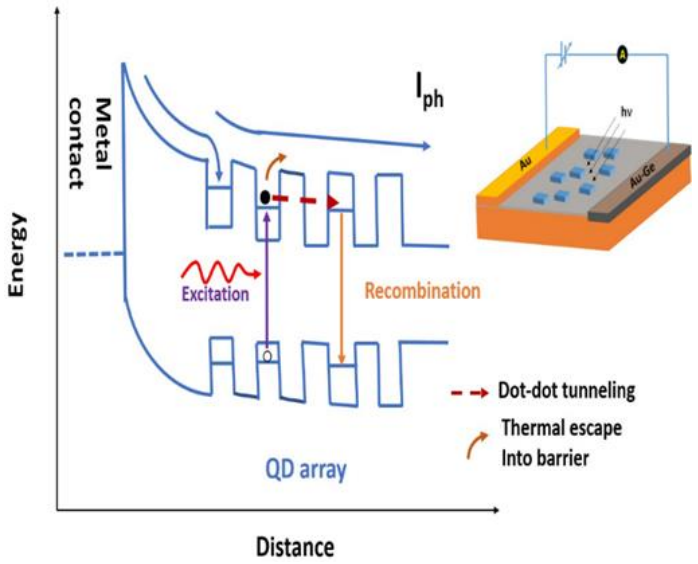

Fig.7.4 *Schematic representation of energy band structure with distance for QD photodetector including different carrier capturing and relaxation channels. Inset: SML QD based photodetector with two top metal contacts of Au and Au-Ge.*

by two different lateral conductive channels: (i) direct transfer to the adjacent dots by quantum mechanical tunneling through the intermediate GaAs barrier medium and (ii) thermionic emission to the continuum barrier states as free charge carriers [3]. The overall photocarrier escape time (τ_{esc}) is given by

$$1/\tau_{esc} = 1/\tau_{tun} + 1/\tau_{th} \exp(-E_A/kT) \qquad (7.3.2.1)$$

where τ_{tun} is the tunnel time, τ_{th} is the lifetime for thermal relaxation and E_A is the thermal activation energy [4-6]. The electrons reach the edge of the depletion region by tunneling through a series of laterally coupled quantum dots followed by a thermionic escape into GaAs medium. They are subsequently subjected to the sweeping field of the depletion region which accounts for the photocurrent signal collected at the electrodes.

The photo-current intensity is related through a model carrier rate equation which describes the effective rate of photocarrier population n(t) in QD ground state, as given by [3]

$$\frac{dn(t)}{dt} = \eta_{ph} - \frac{n(t)}{\tau_{rec}} - \frac{n(t)}{\tau_{esc}} \qquad (7.3.2.2)$$

where η_{ph} is the rate of photocarrier generation in QD states. Under the steady-state condition, characterized by $\frac{dn}{dt}$ = 0, when the rate of photocarrier generation and relaxation counter-balances each other, leads to a steady photocurrent (I_{ph}) as given by

$$I_{ph} = {}^{n_{eql}}/_{\tau_{esc}} = \frac{\eta_{ph}}{1 + \tau_{esc}/\tau_{rec}} \qquad (7.3.2.3)$$

The characteristic recombination lifetime τ_{rec}, tunnel time τ_{tun} and thermal activation energy for different SML coverage (0.4-0.8 ML) are extracted by fitting the respective temperature-dependent peak-related photocurrents by the model equations (7.3.2.2) and (7.3.2.3), as shown in Fig.7.3. The evaluated fitting parameters are listed in Table-7.1. All the parameters are compared with the same extracted parameters corresponding to the reference SK-QD sample. The values of lifetimes and thermal activation energy for different SML coverage as extracted from the steady-state charge transport simulation are in good agreement with the same parameters deduced from the temperature-dependent PL measurements.

Table-7.1 ***Fitting extracted carrier lifetimes and measured responsivity***

SML Coverage (ML)	Fitting extracted parameters			Estimated E_C (meV)	Measured responsivity @V_B= -2V, f=400 Hz, and T=80 K
	τ_{tun} (ps)	τ_{rec} (ps)	E_A (meV)		R (10^{-2} A/W)
0.4	1029±34	131±21	35±2	134	1.9
0.6	876±32	216±20	52±5	119	5
0.7	415±16	478±18	110±9	92	7.8
0.8	314±20	1155±35	133±8	80	9.5
SK	1432±42	1009±30	21±5	33	0.5

7.3.3 Simulation results

From the evaluated values of the extracted parameters, it is quite evident that with increasing InAs SML coverage, recombination lifetime increases, tunnel time decreases and more importantly their ratio τ_{rec}/τ_{tun} monotonically increases. The increase in thermal activation energy E_A with increasing SML coverage indicates progressively less probability of thermionic emission into GaAs barrier medium. But the overall effect, as manifested in a reduction in estimated photocarrier escape time with increasing SML coverage at different temperatures (5-250 K) (shown in Fig.7.5), implies that the tunnel assisted carrier transport through the lateral conductive channel becomes more efficient at higher SML coverage.

Enhanced lifetime for inter-band carrier recombination at higher InAs sub-monolayer coverage is essentially attributed to weaker electron-hole coupling in QD ground state owing to their larger spatial separation, as elaborately discussed previously in the Chapter-5 [1]. Increment of the rate of dot-to-dot tunneling with increasing SML coverage is a consequence of stronger overlap of inter-dot electronic wavefunction mediated by close intermediate separation (L_B), following the relation [5]

$$1/\tau_{tun} \propto \exp(-2L_b) \qquad (7.3.3.1)$$

This is supported by the progressively decreasing value of the average inter-dot separation L_B ~85 nm, 68 nm, 47 nm, and 39 nm for 0.4, 0.6, 0.7 and 0.8-ML coverage respectively measured from GISAXS results, as previously discussed in Chapter-5 and Chapter-6 [7]. The overall rise

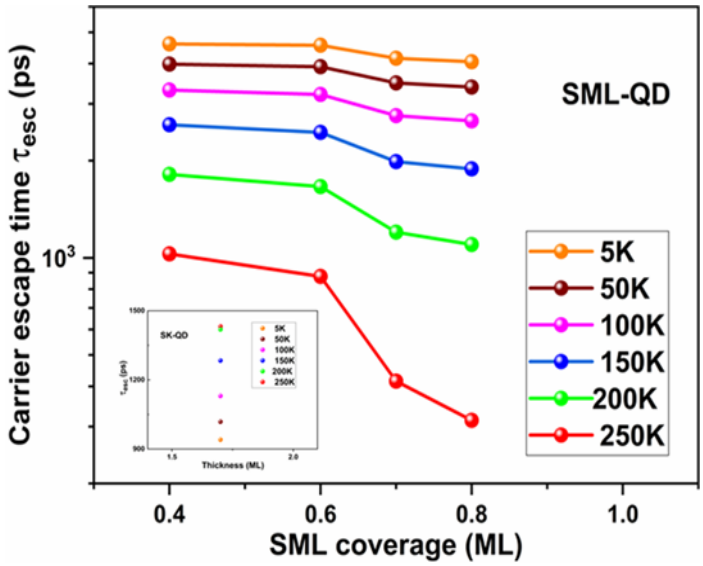

Fig.7.5 Evaluated photocarrier escape lifetime as a function of InAs SML coverage at different temperatures.

in τ_{rec}/τ_{tun} with increasing coverage fraction implies that the photocarriers transit through the lateral array of QDs by faster inter-dot tunneling before they could undergo inter-band recombination with the hole in valance band. One can also notice that the tunnel time (~1432 ps) corresponding to the SK-QD is much higher than that of SML-QD samples. This is a consequence of a larger average inter-dot separation of ~105 nm [7]. The fitting extracted thermal activation energy (E_A) of 35, 52, 110 and 133 meV for 0.4, 0.6, 0.7 and 0.8-ML coverage respectively reflect an increasing trend of activation energy with increasing SML coverage. The activation energies have been found close to the potential depth $\Delta E \sim E_{GaAs}$-E_{QD} of ~30, 40, 90 and 114 meV between GaAs (barrier) conduction band edge and QD's electronic ground state for respective SML coverage. Therefore, the photocarriers having enough thermal energy (~k_BT) to surmount this potential barrier, contribute to the overall detector's

photocurrent. The enhancement of the activation energy (or potential depth ~ E_{GaAs}-E_{QD}) with increasing SML coverage is attributed to lowering in QD electronic ground state energy with the reduction in quantum confinement effect [1, 8].

7.3.4 Explanation of temperature-dependent PC intensity

The relative temperature dependence of the measured PC for different SML coverage, as depicted in I_{ph} *-1/T* plots in Fig.7.3 can be described in terms of effective lateral carrier transport characterized by the fitting extracted parameters τ_{rec}/τ_{tun} and E_A. The temperature variation of PC intensity can be resolved into three distinct temperature regimes. In the low-temperature regime (T<100K), the PC is very small and almost independent of temperature. In the mid-temperature range (100<T<180K), the PC exhibited an increment with increasing temperature for all SML coverages. If the temperature is further increased (T>180K), the PC starts to saturate with temperature.

In the low-temperature regime (T<100K), the thermalization effect remains suppressed by the temperature-independent tunnel induced carrier transport competing with inter-band recombination. At lower SML coverage (0.4-0.6 ML), extracted $\tau_{rec}<\tau_{tun}$ essentially indicates a higher probability of recapturing of photo-generated carriers back to its ground state before they could escape the QD potential. This reduces the rate of free charge carrier population in the conduction channel leading to a drop in recorded photocurrent. On the other hand, inter-dot carrier tunneling faster than the rate of recombination ($\tau_{rec}>\tau_{tun}$) for higher SML coverage (0.7-0.8 ML) basically promotes a greater number of free electrons in the lateral transport channel before they could again be trapped in individual QD potential. This, in turn, enhances the conductivity of the channel and thus leads to a rise in PC intensity.

In the temperature-controlled region (100<T<180K), the thermally activated channel of photocarrier emission into the continuum GaAs barrier states outruns all other carrier relaxation

processes, which even gets boosted up with the increase in temperature. The monotonic rise in the PC signal with an increase in temperature is attributed to a greater number of thermally escaped free electrons in the conduction channel in between two top electrodes [3]. The variation in PC signal in this temperature regime could more elegantly be described in terms of characteristic thermal activation energy (E_A) which is a measure of thermal energy needed for the confined photocarrier to overcome the potential offset of ~ E_{GaAs}-E_{QD}. The relatively smaller value of activation energy for lower SML coverage, as listed in Table-7.1, indicates a higher photocurrent along with the steeper rate of increment with increasing temperature in the temperature-controlled regime.

The saturation of photocurrent at an even higher temperature (T>180K) for all coverages can be explained as a consequence of mutual competition between rate of photocarrier generation by excitonic dissociation and the rate of thermal assisted carrier transfer from QD ground state to the barrier continuum state. The photocarrier generation is mediated by electron-hole (e-h) pair separation by dissociating the QD excitonic bound state through near-infrared excitation. The rate of photogeneration is equivalent to the excitonic dissociation efficiency. The dissociation efficiency η_{ph} in quantum dot confined state is inherently related to the Coulombic attraction between e-h pair by the relation

$$\eta_{ph} \propto \exp(-E_c/kT) \qquad (7.3.4.1)$$

where k is the Boltzmann constant and E_c is the active Coulombic attraction energy between e-h pair modified by the effect of QD-size dependent carrier confinement [9]. For a quantum dot of average size R, the Coulomb energy between e-h pair is given by

$$E_c = 1.8e^2/4\pi\,\varepsilon_0\varepsilon_r R \qquad (7.3.4.2)$$

where e is the electronic charge, ε_0 is the free space permittivity and ε_r is the dielectric constant of InAs. Values of the average QD sizes corresponding to different InAs coverage have been

directly taken from the Raman measurements, as discussed in Chapter-5. The average QD sizes (R) are 1.5 nm, 1.7 nm, 2.1 nm and 2.45 nm for 0.4, 0.6, 0.7 and, 0.8 ML coverage respectively. The estimated Coulombic interaction energy (E_c) for different SML coverage is enlisted in Table-7.1 which clearly depicts a decreasing trend with increasing SML coverage owing to a greater degree of e-h spatial separation for larger QD size along the direction of confinement. The consequent dissociation efficiency (η_{ph}) is estimated and plotted as a function of SML coverage in Fig.7.6 which exhibits a clear increasing trend with increasing coverage fraction. Reduced Coulomb interaction owing to well-separated e-h pair with increasing SML coverage leads to a greater degree of excitonic dissociation. Both the rate of photocarrier generation and

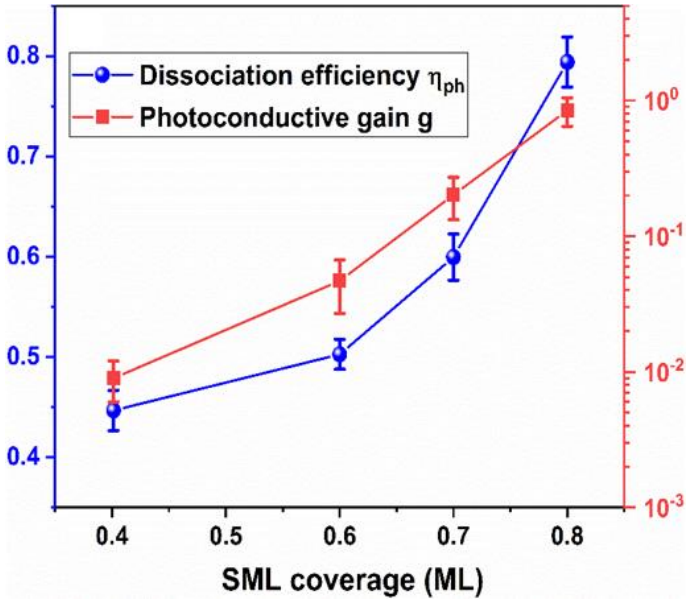

Fig.7.6 *Estimated photocarrier dissociation efficiency and photoconductive gain in arbitrary units for different SML coverage. Both of them were found to increase with coverage.*

their subsequent thermionic emission increases with increasing temperature which counterbalances each other, leading to saturation in the PC intensity. The individual rates are dictated by the corresponding Coulomb interaction energy E_c and thermal activation energy E_A. Their relative value E_A/E_c essentially determines the magnitude of recorded PC intensity. For lower InAs SML coverage (0.4-0.6 ML), extracted value of $E_A<E_c$, as listed in Table-7.1, clearly suggests thermal escape of most of the dissociated carriers into the conduction channel

in GaAs medium. Greater rate of promoting thermally excited photocarriers for conduction results in higher saturation PC intensity at comparatively lower coverage. On the other hand, for higher coverage (0.7-0.8 ML), the evaluated value of $E_A > E_c$ indicates the rate of carrier dissociation still exceeds the rate at which the thermally excited carrier escapes the confinement potential and contribute to overall PC. This leads to a reduction in saturation PC intensity as compared to the lower coverage samples [10].

Therefore, in a nutshell, the temperature variation of PC is determined by the ratio τ_{rec}/τ_{tun} at low temperature (T<100 K) where higher coverage sample associated with a higher value of τ_{rec}/τ_{tun} leads to greater photo-response. In the mid-temperature range (100 K<T<180 K), the PC increases with increasing temperature and the lower coverage sample with characteristically smaller thermal activation energy offers greater photocurrent at the same temperature. In the high-temperature region (T>180 K), the PC saturates for all coverage values depending upon the relative strength of carrier generation and thermionic emission.

7.3.5 Photoconductive gain and external quantum efficiency

The associated external quantum efficiency (EQE) have been estimated by using the relation, $EQE = Rhc/e\lambda$, where R is the measured responsivity, h is the Planck constant, c is the speed of light and λ is the wavelength of excitation [4]. The EQE values have been determined to be 4.1%, 9.7%, 17.3% and 23.8% under a reverse bias (V_B) of -2V for 0.4, 0.6, 0.7 and 0.8 ML coverage respectively. This clearly indicates a significant rise in overall photodetector gain with increasing SML coverage. EQE or alternatively, the overall gain is proportional to the product of two distinct gains in the form of carrier dissociation efficiency (η_{ph}) and photoconductive gain (g) of the system. Therefore, the variation of EQE with SML coverage is most likely to be qualitatively determined by studying the impact of varying InAs coverage upon the individual gains. Previously, we have discussed the increasing trend of excitonic dissociation efficiency with increasing SML coverage, as shown in Fig.7.6. The

photoconductive gain is a measure of the degree of free charge extraction from QD confined states into the conduction channel. The photoconductive gain (g) is approximately inversely proportional to the cross-section (p_c) of charged carrier re-capture back to the QD states related by the semi-empirical relation [6]

$$g \sim \frac{1-p_c}{p_c};\ \ where\ \ p_c = 1 - \exp(\tau_{rec}/\tau_{tun}) \qquad (7.3.5.1)$$

Evidently, lower the capture cross-section (p_c), higher is the photoconductive gain. The increasing ratio τ_{rec}/τ_{tun} with increasing SML coverage leads to progressively decreasing capture cross-section which in turn gives rise to enhancement in photoconductive gain, as depicted in Fig.7.6. Re-capture of dissociated carriers is mediated by inter-band recombination of QD's e-h pairs while transit of charge carriers through the detector's active region is attributed to inter-dot tunneling through the GaAs medium [7]. Increasingly greater rate of inter-dot tunneling ($1/\tau_{tun}$) than the rate of inter-band recombination ($1/\tau_{rec}$) helps to extract a greater number of charged carriers from QD confined states and maintain larger free charge population in the detector's active conduction channel. The increasing value of τ_{rec}/τ_{tun} with increasing SML coverage allows tunnel-assisted easier transport of the carriers before they could be trapped in QD states again [11-12]. This essentially attributes to enhancement in photoconductive gain with increasing InAs coverage. The extracted charge carriers, subjected to sufficient external surface electric field can be transported to the electrodes through the active region. With a greater number of such free charge carriers in the lateral conductive channel associated with higher photoconductive gain can easily be integrated into higher photocurrent response and fast speed charge transport through the conduction channel [13].

7.3.6 Bias dependent photo-response

The photoresponsivity for all SML coverages has been plotted in Fig.7.7 as a function of increasing reverse bias (V_B) applied on the electrodes, through PC measurement at T=80 K.

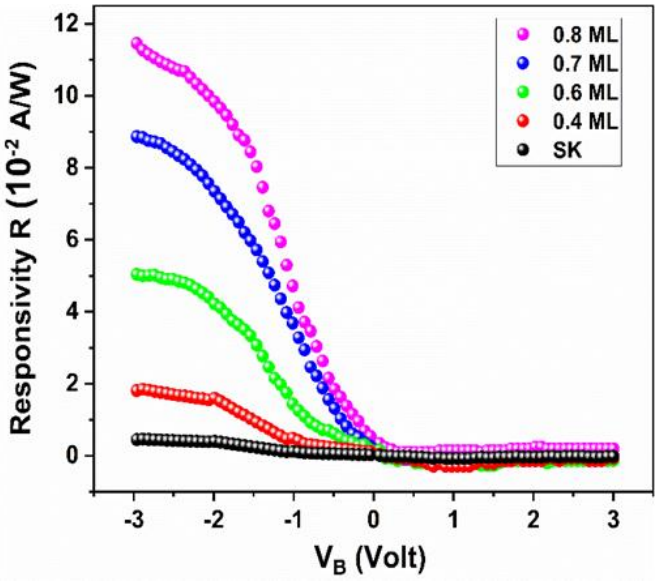

Fig.7.7 Variation of responsivity with an applied reverse bias for different SML coverage including reference SK QD sample.

But the rate of increment in the measured responsivity is progressively greater for higher SML coverage. Under -2V applied bias, six times larger responsivity (~95 mA/W) has been recorded for 0.8 ML coverage as compared to the 0.4 ML coverage sample. This is basically attributed to tunnel-induced carrier transport through the lateral conductive channel with a comparatively larger photoconductive gain. In comparison to the reference SK-QD sample, twenty times larger photoresponsivity is registered with 0.8 ML SML-QD PD, measured at 80K under -2V applied external bias. This is essentially attributed to tunnel-assisted carrier transport through the array of coupled SML-QDs with tunnel time of 350 ps, four times faster than the tunnel time of 1328 ps in SK-QD photodetector. Large tunnel time in the case of SK-QDs is boosted by unwanted thermal carrier relaxation into the wetting layer states [7].

This tunnel assisted fast carrier transport is also expected to improve the detector operational response speed along with a provision of controlling it by varying SML coverage [1]. This is discussed in the next sub-section.

7.3.7 Temporal photo-response as a function of InAs sub-monolayer coverage

The photocarrier response time is an important photodetector device parameter for fast-speed optoelectronic applications [14]. To quantitatively study the effect of varying InAs (SML) coverage upon the charge transport dynamics the corresponding transient photo-response has been recorded. The photodetectors, kept at 80 K under -2V reverse bias have been excited by a chopper modulated monochromatic light from Gemini source acting in the frequency range of 100 Hz to 800 Hz. The subsequent temporal photo-response has been measured by using a digital oscilloscope. The QD-PD samples have been excited by near-infrared radiation of specific wavelength associated with the maximum of spectral responsivity for respective SML coverage. The intensity for all the excitation radiation has been set at around 0.2 $mWcm^{-2}$. Detector photo-response to a square pulse of 400 Hz switching frequency is depicted in Fig.7.8 which clearly exhibits a certain amount of pulse distortion at the time of signal rise and decay.

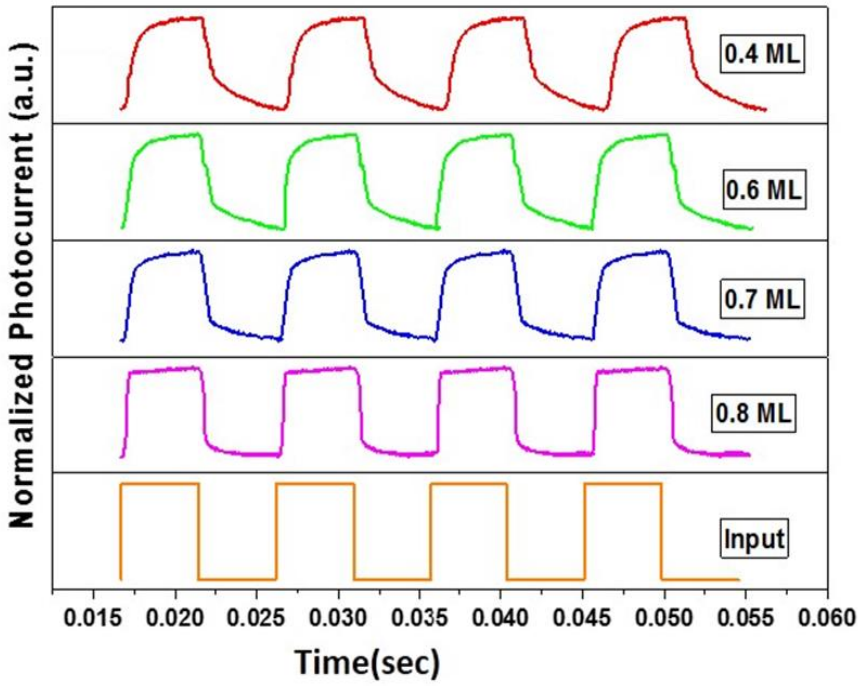

Fig.7.8 Transient photocurrent in response to a square signal oscillating at 400 Hz for different SML coverage measured at 80K under -2V bias. (b) The corresponding calculated relative balance for a different switching frequency of the input excitation signal.

The temporal variation in photocurrent exhibits a sharp rise in photo-signal in the presence of input pulse illumination, followed by a comparatively slower decay in the absence of signal illumination for all SML coverages (0.4-0.8 ML). The corresponding rise and decay times are extracted out by fitting the rise and decay of the temporal response signal separately, using multiexponential functionals, as depicted in Fig.7.9. The rise time (τ_r) has been determined by

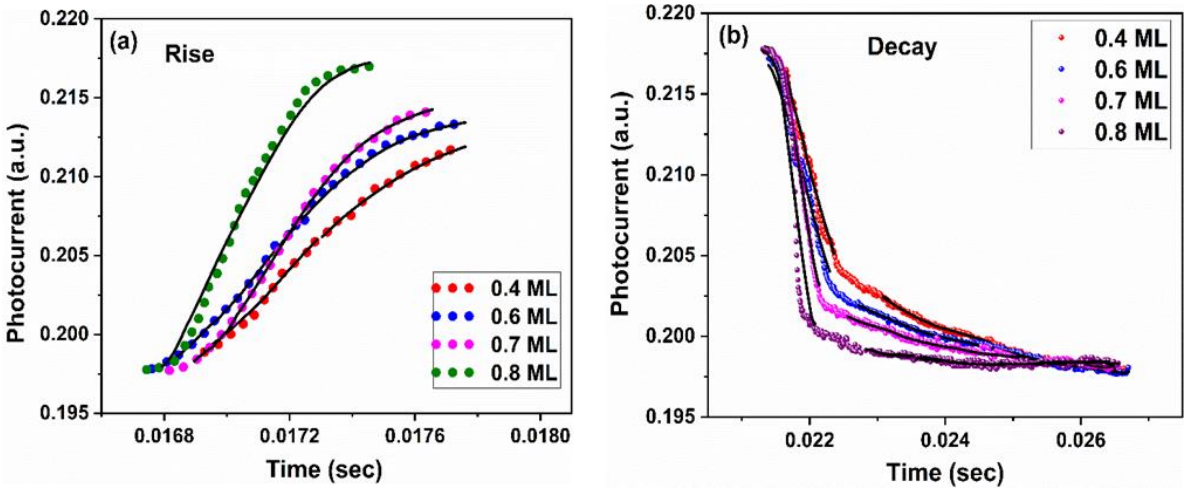

Fig.7.9 *(a) Rise and (b) decay of transient photocurrent (dots) with corresponding multiexponential fitting (solid lines).*

fitting the rise in PC intensity $I_{ph}(t)$ (shown in Fig.7.9 (a)) for different SML coverage by the exponential relation

$$I_{ph}(t) = Aexp(-t/\tau_r) \qquad (7.3.7.1)$$

Similarly, the decay response time is determined by fitting the decay in response to PC intensity $I_{ph}(t)$ (shown in Fig.7.9 (b)) by the bi-exponential fitting equation

$$I_{ph}(t) = Bexp(-t/\tau_{d1}) + Cexp(-t/\tau_{d2}) \qquad (7.3.7.2)$$

where τ_{d1} and τ_{d2} are the decay lifetimes corresponding to two different PC physical decay channels. A B and C are the corresponding proportionality constants. The extracted values of the rise and decay response time for different SML coverages are listed in Table-7.2. Evidently, both the response lifetimes have exhibited an apparent decreasing trend with increasing SML

coverage. In addition to that, the maximum transient PC has been recorded to be significantly greater for higher SML coverage. This is attributed to a greater number of extracted free charge carriers transported along high conductivity channels mediated by efficient inter-dot tunneling through the active medium [15]. This, in turn, increases collection efficiency as well as the rate of collection of charge carriers at the electrodes [16-17] which consequently accounts for the faster rise in response PC intensity. Almost thirteen times drop-in rise time as low as 100 μs have been achieved with 0.8 ML coverage InAs SML-QDs as compared to a rise time as high as 1260 μs found for the SK-QD sample. This is a manifestation of faster photo-response which makes SML QD a more superior active medium for fast speed photodetectors than conventional SK-QD. The extracted two decay lifetimes are related to two different carrier trap channels ending up to some interfacial defect states [18-19].

Table 7.2 ***Detector Response times***

SML Coverage (ML)	**Time response**		
	Rise time	**Decay time**	
	τ_r (μs)	**τ_{d1} (μs)**	**τ_{d2} (ms)**
0.4	366±28	580±32	3.6±0.25
0.6	253±14	445±37	2.7±0.33
0.7	182±21	317±35	2.2±0.38
0.8	100±19	220±41	1.8±0.20
SK	1210±32	1554±45	5.2±0.50

The InAs SML-QD based photodetector works with excellent reproducibility throughout a wide frequency range of 100 Hz to 1300 Hz. The resulting temporal photo-response has been

found to be fairly stable up to 30 reproducible cycles [20]. Moreover, the maximum operating pulse switching frequency for substantial detector response also increases with increasing SML coverage. The reproducibility of temporal photo-response and the higher cut-off of operating switching frequency is quantitatively represented by a detector parameter, called relative balance (R.B.), defined as

$$R.B. = \frac{I_{max} - I_{min}}{I_{max}} \qquad (7.3.7.3)$$

where I_{max} and I_{min} are the maximum and minimum transient PC intensity [21]. The evaluated values of relative balance are plotted with InAs SML coverage, as depicted in Fig.7.10.

Evidently, the R.B. value drops to 80% of its maximum at 600 Hz and for 0.4 ML and at 1.3 kHz for 0.8 ML coverage. This is an indication of more sustainable temporal photo-response

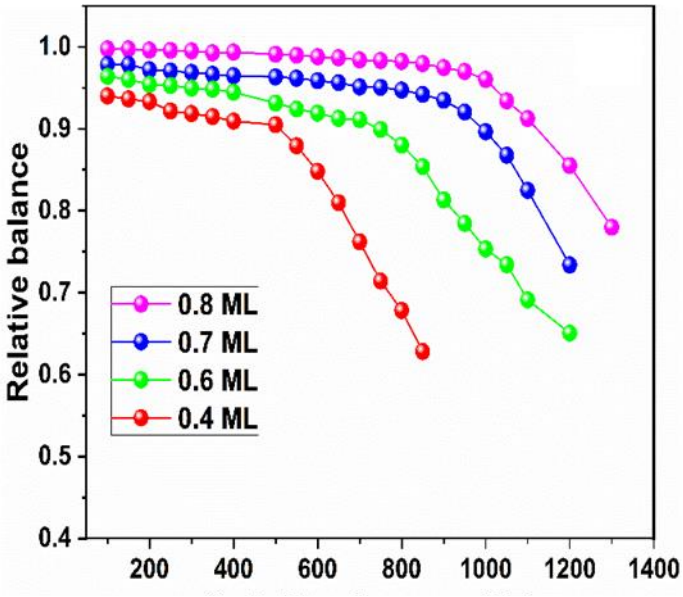

Fig.7.10 *The corresponding calculated relative balance for a different switching frequency of the input excitation signal.*

in the case of higher InAs SML coverage which keeps on following the input square pulse.

7.4 Dark current analysis

Dark current measurement is an important aspect of the detector's photodetection performance throughout the temperature range. High photocurrent to dark current ratio maintained up to

higher temperature is always preferred for practical efficient photodetector applications. The effect of confinement of injected carriers upon the dark current is analyzed over a wide range of temperatures with varying sub-monolayer coverage. The behavior of dark current, noise generation, and photodetection performance parameters with applied bias voltage and operating temperature are elaborately discussed in this section.

7.4.1 Effect of dark-carrier trapping at different sub-monolayer coverage

To quantitatively study the effect of varying InAs SML coverage upon the detector's dark current response, the respective dark current intensity (I_d) has been measured at 80 K under different applied bias (V_B) varying in the range of -4V to +4V for different SML coverages (0.4-0.8 ML), as graphically depicted in Fig.7.11 (a). The dark current characteristics for all coverages exhibit a substantial mismatch between the measured dark current of 10^{-10}A under reverse bias and 10^{-7}-10^{-8}A under forward bias. This apparently asymmetric behaviour of dark current for positive and negative bias is due to easier electron transport through the Schottky

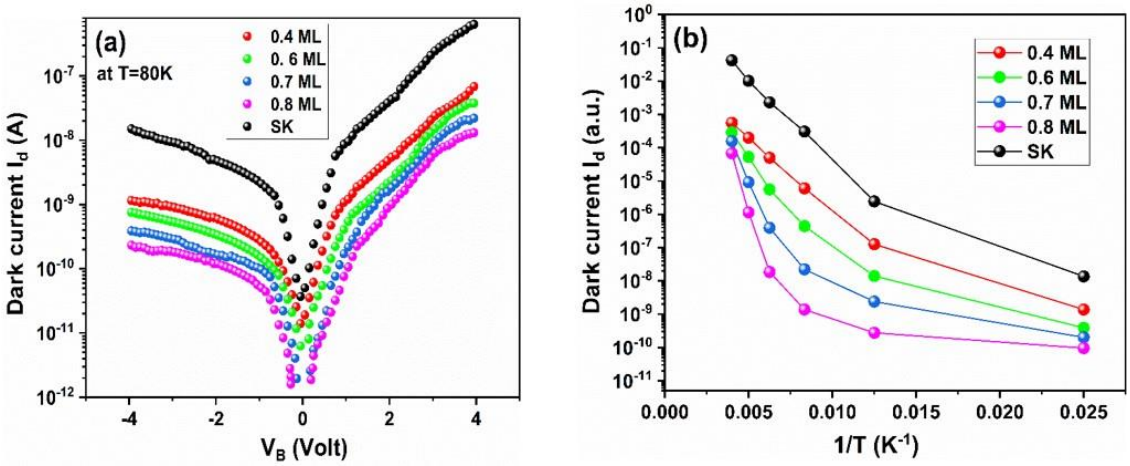

Fig.7.11 Variation of dark current with (a) applied bias in the range ±4V and (b) temperature for different SML coverage.

barrier junction under forward bias as compared to reverse bias [14]. The dark current is mainly mediated through thermionic re-emission of the captured injected electrons from QD confined states to the free carrier continuous barrier states capable of conducting current [22]. After the injection of free charge carriers through the emitter electrode into the active region consisting

of embedded QDs, the carriers could drift towards the electrodes over the detector surface or get trapped in quantum dot bound states [18]. The captured electrons in bound QD states undergo subsequent recombination into the valance band or thermally escape out of the QD confinement potential to the free barrier states. There is a certain relaxation time τ_c associated with the thermionic emission of the trapped electrons required to thermally escape the effective potential barrier (~E_{GaAs}-E_{QD}) before they are re-trapped back to the QD state by recombination with holes in valance band. The potential barrier height for the thermionic escape of dark carriers is equivalent to the corresponding thermal activation energy (E_A), as deduced from the fitting results [16]. The probability ($1/\tau_c$) for such thermionic emission, as proposed by Ryzhii et al, is expressed as [22]

$$1/\tau_c \propto \exp(-E_A/kT) \qquad (7.4.1.1)$$

Evidently, higher thermal activation energy leads to a lower rate of thermionic escape of the captured dark carriers into free GaAs barrier states. Therefore, the SML-QD samples with higher coverage associated with higher activation energy are more conducive to restrict or slow down the thermionic emission into GaAs barrier states which in turn reduces the field-induced flow of dark carriers through the conduction channel. As a consequence, ten times drop in dark current for 0.8 ML coverage has been recorded as compared to 0.4 ML coverage at 80 K under -2V applied reverse bias.

The dark carrier suppression also remains active throughout the whole operating temperature range (80-250K). The greater degree of dark current suppression at higher SML coverage is manifested by lowering of dark current from $5x10^{-4}$ A for 0.4 ML to $6x10^{-5}$ for 0.8 ML coverage under -2V applied bias recorded at near room temperature (~250 K), as depicted in Fig.7.11 (b). With increasing SML coverage, the progressively increasing density of QD trap centres for the injected dark carriers in the active medium also plays a decisive role in inhibiting dark

carrier extraction [8,23]. The discrete carrier states of the QDs, serves as trap centres for the injected charge carriers in the potential well. Once trapped by these potential wells, the carriers (dark) takes some time to escape the potential barrier thermionically to reach the barrier continuum state and then take part in current conduction. This leads to finite reduction in net charge flow and thus reduces the dark current. As the density of dots increases, a greater number of such carrier trap centres start to work that leads to more suppression of free dark carriers into the conduction channel and thus cumulatively reduces the overall dark current. One can also notice, two orders of magnitude lower dark current have been registered with SML-QDs, as compared to the measured dark current of ~10^{-4} A for reference SK-QD sample under the condition of V_B = -2 V and T=250K. This is the consequence of stronger confinement induced dark carrier trapping with a greater number of QD trap centres as compared to SK-QD based photodetector [24].

7.4.2 Dark noise current measurement and specific detectivity

7.4.2.1 Noise power density measurement

A SR-830 lock-in amplifier has been employed to measure the noise power density (*S*) throughout the operating temperature range of 40 K to 250 K [25]. The noise power density

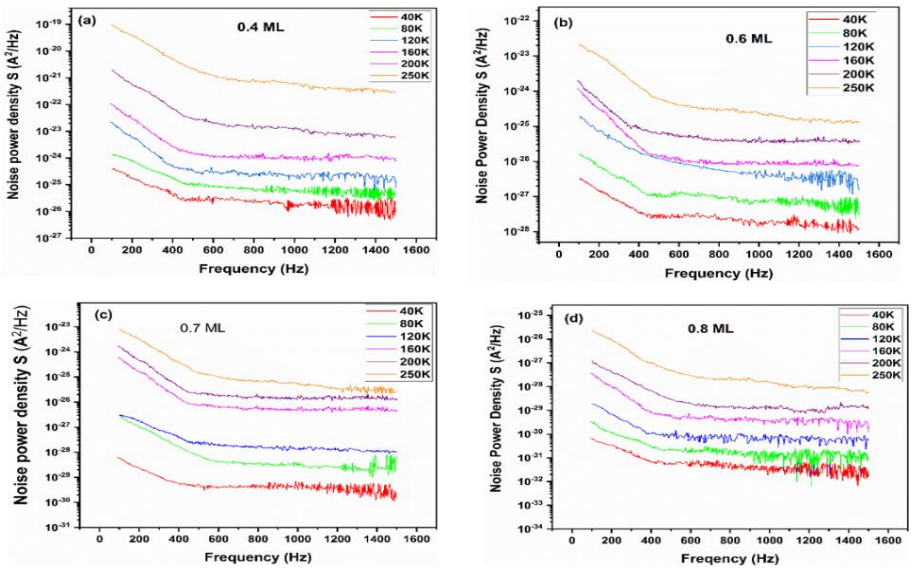

Fig.7.12 Variation of measured noise power density with frequency at different temperatures for different SML coverage.

normalized to the measurement bandwidth (B) is continuously plotted with frequency for all temperatures, as shown in Fig.7.12 (a)-(d).

7.4.2.2 Specific detectivity

Detectivity is an important figure of merit for QD-based PD which is a measure of photodetection performance. For efficient high-temperature photodetection, the detectivity needs to be high enough to distinguish the photo-signal from the system's dark noise current. The noise-limited specific detectivity D* has been determined by using the relation

$$D^* = RA^{1/2}/S^{1/2} \qquad (7.4.2.2.1)$$

where R is the measured responsivity, A is the effective area of the detector and *S* is the spectral density noise power measured per unit measurement bandwidth [26]. The specific detectivity corresponding to each of the SML coverage (0.4-0.8 ML) has been evaluated at a switching frequency of 400 Hz. The value of S has been directly taken from the Fig.7.11. The specific detectivity for all coverages, measured under the condition T=80K, V_B=-2V and f=400 Hz are evaluated which are enlisted in Table-7.3.

Table 7.3 ***Evaluated D* @ T=80K, V_B=-2V and f=400 Hz***

SML coverage (ML)	**Specific detectivity D* (10^{11} cmHz$^{1/2}$w^{-1})**
0.4	1.5
0.6	3.2
0.7	12.5
0.8	42
SK	0.08

The detectivity corresponding to each SML coverage at T=80 K has been estimated which are plotted with the applied reverse bias varying in the range from 0V to -4V, as shown in Fig.7.13 (a). The apparent increasing trend of the determined detectivity for all coverages up to an

intermediate applied bias of -2V is a clear signature of greater enhancement of electric field-assisted PC than the dark current with increasing applied bias at such low temperature of 80K [15]. The peak specific detectivity measured at T=80 K, V_B=-2V and f=400 Hz have been deduced to be $1.5x10^{11}$,$3.2x10^{11}$,$1.25x10^{12}$ and $4.2x10^{12}$ $cmHz^{1/2}w^{-1}$ for 0.4, 0.6, 0.7 and, 0.8 ML coverage respectively. Evidently, two orders of magnitude higher detectivity have been obtained as InAs SML coverage is increased from 0.4 ML to 0. ML. This is attributed to two co-existing factors: the tunnel assisted enhancement of PC and stronger confinement induced suppression of dark current with increasing InAs coverage. Almost three orders of magnitude higher specific detectivity D* has been achieved by employing SML-QDs in the active medium as compared to that of $8x10^{9}$ $cmHz^{1/2}w^{-1}$ for SK-QDs (reference sample). This has been attributed to the more efficient conduction of carriers integrated into larger photocurrent with minimum loss and simultaneous inhibition of dark carrier conduction in the presence of greater

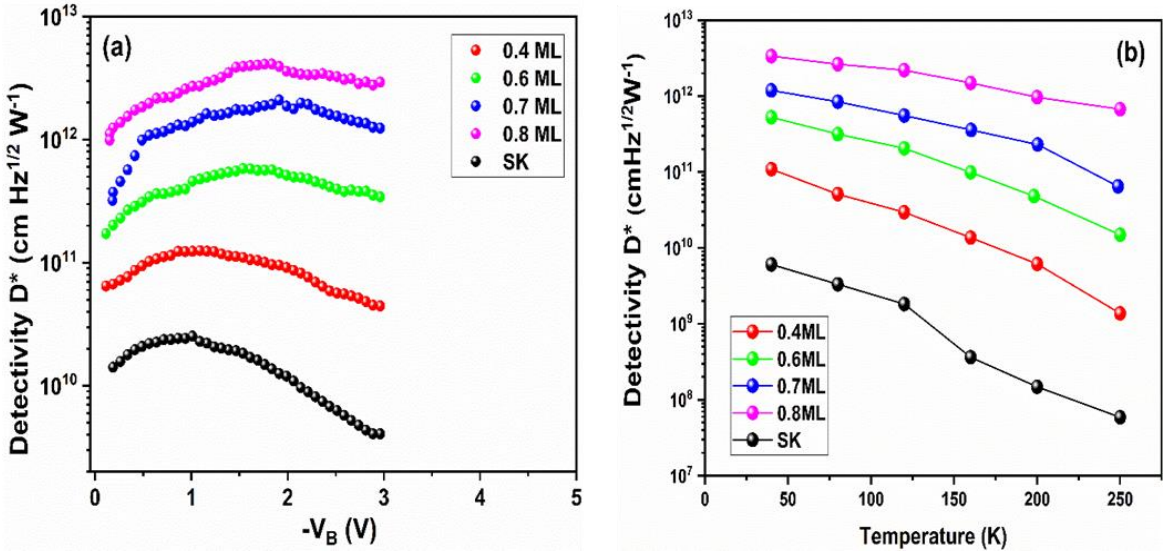

Fig.7.13 *Variation of measured detectivity at f=400 Hz with (a) applied reverse bias and (b) temperature for different coverage fraction including the reference SK QD sample.*

carrier trapping [8]. In conventional SK-QDs a substantial amount of thermal relaxation of photocarriers to the inherent dissipative wetting layer states highly degrades the PC gain [6]. The temperature variation of the maximum peak specific detectivity measured at -2V for all coverages are depicted in Fig.7.13 (b). It has been experimentally found that for all coverage

fractions (0.4-0.8 ML), the PC recorded at the lowest operating temperature (25K) under only background radiation remains greater than respective dark currents measured at higher temperatures up to T=250K under all applied bias in the range 0V to -2V. This indicates that by employing SML-QDs, the background-limited operating temperature rises up to 250K for all SML coverages which offer near-room temperature faithful photodetection in the NIR range [34-35]. Moreover, two times higher specific detectivity has been registered at T~250K with increasing the SML coverage from 0.4 ML to 0.8 ML. This suggests the higher coverage samples are more conducive to sustainable detectivity up to near-room temperature [19]. This is attributed to a progressive reduction of confinement-induced dark current with increasing SML coverage up to higher temperatures. The reference SK-QD sample has exhibited a detectivity of ~$8x10^7$ $cmHz^{1/2}w^{-1}$ (shown in Fig.7.13 (b)) at T=250K, V_B=-2V and f=400 Hz which is almost five orders of magnitude lower than that of ~ 10^{12} $cmHz^{1/2}w^{-1}$ measured for SML-QDs under the same condition. From this, it is quite apparent that SML-QD is much superior to conventional SK-QD for being employed in the active medium of photodetectors which potentially offers larger sustainable photodetection up to higher temperatures. The detectivity of this InAs SML-QD based NIR photodetector is potentially quite comparable with graphene-based QD photodetector, offering a detectivity ~10^{12} $cmHz^{1/2}w^{-1}$ at the temperature ~250 K [19].

7.5 Summary

In a nutshell, this work is mainly intended to study the feasibility of simultaneously tuning the external quantum efficiency, operational speed and signal detectivity of InAs/GaAs sub-monolayer QD-based near-infrared photodetector by controlling the InAs layer coverage fraction. This chapter is essentially devoted to providing physical insight into the operation of dark current reduced high-quantum gain fast speed InAs/GaAs sub-monolayer QDIP through quantitative investigation of carrier transport through coupled QD carrier states. Our

observations have led to the conclusion that variation of the SML coverage induces a variation in relative time scales of inter-band recombination and carrier tunneling that essentially governs the overall detector performance. The characteristic lifetimes are extracted from photocurrent simulation by using a kinematic model of photocarrier transport. Progressive rise in photoresponsivity at low temperature (≤100K) with increasing SML coverage can be characteristically described on the basis of the combined effect of increasing photocarrier dissociation efficiency and the probability of its subsequent extraction through the QD based active medium. With increasing coverage, enhanced carrier lifetime and activation of tunnel induced faster carrier transport through the lateral conduction channel with $\tau_{rec}/\tau_{tun} >1$, has promoted enhanced free charge carrier extraction. Fast-speed transit of more number dissociated photocarriers has given rise to progressively higher quantum gain as well as faster and robust high-frequency temporal response with increasing InAs SML coverage. Short response time potentially promotes sub-monolayer QDIP to be potentially active in response to external switching photo-signal up to higher operational frequency. At the same time, with increasing coverage, the increasing degree of trapping of injected carriers in the confined states of the quantum dot has led to effective inhibition of dark current. This has helped to significantly improve the detector's high-temperature performance and offered efficient photodetection up to near room temperature (~250K) with measured detectivity as high as ~$8x10^{11}$ $cmHz^{1/2}W^{-1}$. Therefore, by employing this methodology, fast response speed and high detectivity have been achieved despite the tradeoff between them. Through this study, we have shown the feasibility of tuning both the detectivity and detector response speed to significantly high values by controlling InAs sub-monolayer coverage in spite of the inherent tradeoff between them.

7.6 Bibliography

[1] S. Sato, S. Nozaki and H. Morisaki, J. Appl. Phys. **81** (1997) 1518.

[2] R. J. Kobliska, Phys. Rev. Lett. **29** (1972) 725.

[3] Y. Batra, D. Kabiraj and D. Kanjilal Solid State Commun. **143** (2007) 213.

[4] H. Campbell, P. M. Fauchet, Solid State Commun. **58** (1986) 739.

[5] Y. Saito, J. Cryst. Growth **47** (1979) 61.

[6] J. Jiang, K. Chen, X. Huang, Z. Li, D. Feng, Appl. Phys. Lett. **65** (1994) 1799.

[7] Dana, S. Agan, S. Tokay, A. Aydmh and G. Finstad, Phys. Status Solidi. **4** (2007) 288.

[8] J. S. Kasper, S. M. Richards, Acta Crystallogr. **17** (1964) 752.

[9] E. B. Gorokhov, V. A. Volodin and D. V. Marin, Semiconductors **39** (2005) 1168.

[10] J. Diao, K. Gal and M. L. Dunn, Nat Mater **2** (2003) 656.

[11] S. J. Kim, O. Quy,L. Chang, E. Stach, C. A. Handwerker and A. Wei, J. Mater. Chem **20** (2010**)** 331.

[12] G. Wilfried, H. van Sark, Patrick Frederix, Dave Van den Heuvel, Hans Gerritsen, Ageeth Bol, Joost van Lingen, Celso de Mello Donegá and A. Meijerink, J. Phys. Chem. B **105** (2001**)** 8281.

[13] S. Sato, S. Nozaki, H. Morisaki and M. Iwase, Appl. Phys. Lett. **66** (1995) 3176.

[14] G. Armatas and M. Kanatzidis, Nature (London, U. K.) **441** (2006) 1122.

[15] Y. Kanemitsu, H. Uto and Y. Masumoto, Y. Maeda, Appl. Phys. Lett. **61** (1992) 2187.

[16] G. Dukovic, F. Wang, D. Song, Matthew Y. Sfeir, Tony F. Heinz and Louis Brus, Nano. Lett. **5** (2005) 2314.

[17] X. Shi, S. Zheng, W. Gao, W. Wei, M. Chen, F. Deng, J. Nanopart. Res. **16** (2014) 2741.

[18] Steinhoff, J. H. Kim, F. Jahnke, M. Rosner, D. S. Kim, C. Lee, G. H. Han, M. S. Jeong, T. O. Wehling and C. Gies, Nano Lett. **15** (2015) 6841.

[19] S. Koch, W Kira, G. Khitrova and H. M. Gibbs, Nat. Mater. **5** (2006) 523.

[20] M. Zarachias and P. M. Fauchet, Appl. Phys. Lett.**71** (1997) 380.

[21] H. Adhikary, P. Mclntyre, S. Sun, P. Pianetta and C. Christopher, Appl. Phys. Lett. **87** (2005) 263109.

Chapter 8

Conclusion and future aspects

8.1 Conclusion

The objective of this thesis is the study of the structural and optical properties of quasi zero-dimensional semiconductor structures and investigate the feasibility of their implementation in light-emitting and photodetector devices. The whole thesis work is shaped into two major parts, i.e., growth and characterization of elemental Gr IV Ge nanocrystal and self-assembled sub-monolayer quantum dot of III-V compound of InAs/GaAs. The study includes investigation of optoelectronic properties of the low-dimensional structures as a function of adatom kinetics and effective layer coverage of growth which has been systematically correlated with active lattice strain and structural information.

Ge exists in two phases, namely simple cubic, and tetragonal (ST-12) structure. But in nature, Ge is mainly found in a normal cubic phase which has a very small indirect bandgap. On the other hand, the rare metastable tetragonal Ge phase has a direct bandgap of much higher energy which is more demanding for high gain light-emitting applications. But this novel phase can only be realized if the Ge crystallites are grown in sufficiently small size. As part of this thesis work, we have worked towards developing an ionized cluster beam deposition technique to grow this tetragonal phase in a substantial amount while suppressing the growth of the normal cubic phase through the formation of Ge nanocrystals. We have categorically shown a selective yield of co-existing cubic and tetragonal phases by controlling the kinetic energy of the beam of cooled Ge clusters in the deposition chamber. Through adequate structural and optical analysis, it has been observed that the relative abundance of the tetragonal phase can be significantly enhanced by decreasing the kinetic energy of the bombarding cluster beam. The film grown by using neutral Ge clusters corresponding to the lowest kinetic energy shows the highest relative yield of the tetragonal phase for a nanocrystallite size of 7 nm. The nanocrystallite size was found to decrease monotonically from 15 nm to 7 nm with decreasing beam acceleration potential from 2.5 kV to 0 kV. While decreasing the beam energy, below a

certain threshold value of NC's size, the normal cubical phase transforms itself into a more compressed high energy metastable tetragonal (ST-12) phase. The appearance of a broadened redshifted TO-like phonon peak at 275 cm^{-1} in the Raman spectra confirms the growth of Ge nanocrystallites. The monotonic redshift in phonon energy corresponding to the broadened Raman peak with decreasing cluster beam energy (2.5 KV-0 KV) suggests progressively stronger confinement-induced phonon interaction with grain boundaries inside Ge nano-crystallites. This is an indication of the emergence of another Ge phase coexisting with a normal diamond-like structure with a comparatively smaller crystallite size.

The results show the feasibility of tuning the emission energy and efficiency of visible photoluminescence (1.55-1.75 eV) at room temperature (RT) to high values by selectively increasing the relative proportion of tetragonal Ge phase by controlling the beam energy. This offers potentiality of Ge-NCs enriched in the tetragonal phase for RT visible light-emitting applications. We have further studied the provision for controlled photo-oxidation of the tetragonal rich Ge thin films. In this way, it has been possible to further tune the luminescence to green color (~550 nm) while decreasing the effective size of the NC cores under oxide (GeO_x) cover.

The next part of this work is molecular beam epitaxial growth of self-assembled InAs sub-monolayer quantum dots in GaAs matrix and their strain, structural and optical characterization. Photodetector application of these SML QDs has also been studied in detail. We have demonstrated the feasibility of spectral tuning of their excitonic photoemission in the near-IR region (1.4-1.5 eV) by controlling the InAs sub-monolayer coverage from 0.8 to 0.4 ML. Through systematic high-resolution x-ray diffraction, Raman scattering and low-temperature photoluminescence measurements, we have explicitly investigated the effect on spectral properties with varying InAs coverage, as a consequence of the different degree of strain and quantum size effect. The average QD heights for different InAs coverage are

extracted from the fitting of the associated Raman spectra by the Phonon confinement model (PCM). The average QD height reduces from 2.3 nm to 1.4 nm as the coverage is decreased from 0.8 ML to 0.4 ML. The x-ray diffraction measurement shows enhancement of in-plane compressive strain from 1.9 x 10^{-2} to 3.1 x 10^{-2} as a result of the reduction in SML coverage (0.8-0.4 ML). It also has been observed that the built-in compressive surface stress due to lattice misfit between InAs and GaAs, increasing from 54.5x10^{8} Pascal to 178x10^{8} Pascal with decreasing InAs sub-monolayer coverage (0.8 ML-0.4 ML) has controlled the quantum dot growth and played a leading role to determine their density and homogeneity in size distribution. The reduction of layer coverage from 0.8 ML to 0.4 ML causes a reduction in the dot density by almost one order of magnitude from 9x10^{10} cm^{-2} to 2x10^{10} cm^{-2}. The variation of InAs coverage fraction also significantly affects the in-plane spatial arrangement of the embedded SML-QDs. The grazing incidence SAXS measurement along different azimuthal directions shows that with decreasing InAs coverage, the average separation between the embedded QDs as well as the correlation length of the laterally coupled QDs seems to increase. The spectral blueshift from 1.4 eV to 1.5 eV with decreasing InAs coverage from 0.8 ML to 0.4 ML is attributed to the increasing degree of carrier confinement due to a stronger quantum size effect. The reduction of sub-monolayer coverage from 0.8 ML to 0.4 ML has also led to enhancement in exciton binding energy from 4.4 meV to 11.4 meV, which has caused stronger localization to the dissociated photo-carriers at lower InAs coverage. With increasing InAs coverage, the decreasing value of excitonic binding energy and average inter-dot separation (in-plane) initiate enhanced carrier wave function overlap and opens up easy pathways for escape in the form of inter-dot carrier tunneling.

We have further studied the dynamics of photo-generated carriers in correlated self-assembly of embedded InAs/GaAs sub-monolayer quantum dots from the temperature-dependent PL (TDPL) measurements as a function of InAs fractional coverage. It was found that the mutual

competition of excitonic recombination and quantum mechanical photo-carrier tunneling through the carrier states of the electronically coupled system seems to determine the shape and intensity of the TDPL spectra. The lifetimes related to different carrier relaxation channels have been deduced through fitting the respective TDPL spectra by dynamical carrier rate equation following the Localized state functional model. The excitonic recombination lifetimes are found to be 172 ps, 242 ps, 453 ps, and 1125 ps whereas the tunnel times are measured to be 1008 ps, 828 ps, 437 ps and 350 ps for 0.4, 0.6, 0.7 and, 0.8 ML coverage respectively. Evidently, the recombination lifetime increases whereas the tunneling lifetime decreases with increasing SML coverage. More importantly, with increasing SML coverage (0.4-0.8 ML) the ratio of characteristic lifetimes (Γ_r/Γ_t) of recombination and inter-dot tunneling has been found to progressively increase from 0.17 to 3.3 which has been found to hold the key to determine the temperature-dependent spectral properties as a function of InAs sub-monolayer coverage. The extracted Γ_r/Γ_t ratio (~0.17 and 0.3) of less than unity at lower SML coverage (0.4-0.6 ML) suggests that the confined carriers tend to recombine faster in respective QD ground states before transferring into the well-separated neighboring QDs. This gives rise to faster quenching of PL signal with increasing temperature at lower SML coverage (0.4-0.6 ML). On the other hand, at higher SML coverage (0.7-0.8 ML), the value of Γ_r/Γ_t (~1.1 and 3.3) greater than unity suggests that the probability of exciton recombination before carrier escape via inter-dot tunneling decreases monotonically which effectively consequences to extended carrier lifetime. This is attributed to the simultaneous reduction in the probability of recombination of less confined exciton system and provision of faster tunneling of comparatively loosely bound dissociated carriers through narrower intermediate GaAs barrier. This has offered substantial luminescence efficiency up to elevated temperature, greater temperature stability to the peak emission energy and more interestingly a decreasing trend of spectral linewidth with temperature (5-150 K) for higher SML coverage. Activation of non-dissipative photocarrier

escape with effectively enhanced carrier lifetime for higher SML coverage consequently gives rise to subsequently enhanced PL efficiency which sustains up to nearly room temperature (~285 K). This is manifested by progressively increasing the value of extracted thermal activation energy with increasing SML coverage. At higher coverage (0.7-0.8 ML), the anomalous reduction in PL linewidth with increasing temperature in the range of 5 K to 150 K is attributed to energy selective tunnel-assisted carrier transfer and preferential carrier population in some locally minimum QD ground states. On the other hand, at lower SML coverage (0.4-0.6 ML) more localized photocarriers in QD states undergo regular spectral broadening due to predominant temperature-induced carrier-phonon scattering. Moreover, the absence of any photocarrier loss into the wetting layer in SML-QD and observed tunnel-assisted fast photo-carrier transport with tunnel time as low as 350 ps has the potential to expedite the response speed of optoelectronic switching devices. In comparison to tunnel time of 1328 ps for conventional InAs/GaAs SK QDs, a four times faster inter-dot tunneling is observed in InAs/GaAs SML-QD system. Temperature independent carrier recombination and inter-dot transfer of photogenerated electrons in SML QDs offer more thermal stability than conventional SK QD which makes it more demanding for high-temperature optoelectronic applications.

The different degrees of photocarrier escape and energy relaxation in the coupled array of InAs/GaAs sub-monolayer quantum dots as a function of QD spatial correlation offers a further provision of engineering charge transport properties by controlling InAs coverage fraction. With this motivation, the feasibility of simultaneously tuning the dark current, external quantum efficiency and speed of photo-response of QDIP by controlling InAs sub-monolayer coverage has been investigated. A quantitative investigation of radiative recombination and carrier escape from QD confined states has been performed to get a physical insight of tuning of physical response parameters of InAs/GaAs SML-QDIP. The observations have led to the

conclusion that variation of the SML coverage provides a means for controlling the relative time scales of the inter-band recombination and carrier tunneling that can essentially govern the overall detector performance also. The quantum efficiency of photo-response of the SML-QD based photodetector has been found to be governed by the ratio of characteristic lifetimes of excitonic recombination and inter-dot tunneling escape. The ratio of lifetimes, as extracted from the steady-state charge transport simulation has exhibited an increasing trend with increasing SML coverage. This is in good agreement with the results deduced from the dynamical carrier relaxation simulation of temperature-dependent PL.

The photo-response related to inter-band absorption has undergone consistent spectral redshift with increasing SML coverage in the NIR region due to a reduction in inter-band transition energy. The measured photoresponsivity has exhibited a progressive rise with increasing SML coverage at a low temperature (≤100 K) limit. The peak responsivity measured at 80 K under -2 V applied bias has been found to increase by almost ten times as the sub-monolayer coverage is increased from 0.4 ML to 0.8 ML. This can be characteristically described on the basis of the combined effect of increasing photocarrier dissociation efficiency and the probability of its subsequent extraction through the QD confinement states into active conduction channels. With increasing coverage, increasing photo-dissociation efficiency and activation of inter-dot tunneling faster than excitonic recombination ($\Gamma_r > \Gamma_t$) has led to higher photoconductive gain and consequently promotes extraction of more free charge carriers into the electrodes through high conductivity channel. The external quantum efficiency (EQE) for 0.4, 0.6, 0.7 and, 0.8 ML coverage are measured to be 4.1%, 9.7%, 17.3% and 23.8% respectively. The enhanced EQE is attributed to increasing photoconductive gain and carrier dissociation efficiency with increasing SML coverage. The progressively increasing charge carrier collection efficiency with increasing InAs SML coverage leads to enhancement in peak responsivity. The recorded peak responsivities are 1.9 mA/W, 5 mA/W, 7.8 mA/W and 9.5 mA/W for 0.4 ML, 0.6 ML,

0.7 ML and 0.8 ML coverage. The measurements show that in comparison to reference InAs/GaAs SK QD photodetector, the responsivity of 0.8 ML QD photodetector measured under similar conditions has increased by twenty times. The inter-dot carrier tunneling with lower characteristic lifetime also offers efficient transport of dissociated free photocarriers through the detector's active medium which consequences to shorter response time. From transient photo-response of the QD photodetector, the response time has been measured to be 366 μs, 253 μs, 182 μs, 100 μs for 0.4 ML, 0.6 ML, 0.7 ML, and 0.8 ML coverage. The relatively shorter detector response time at higher sub-monolayer coverage pushes up the operational switching frequency from ~ 600 Hz to 1.3 kHz. This offers a more robust temporal response up to higher operational frequency (few kHz) in response to an external switching photo-signal. At the same time, with increasing coverage, the increasing degree of trapping of injected carriers in the confined states of the quantum dot has led to a greater reduction of dark current. Higher thermal activation energy representing the potential offset between QD and barrier layer reduces the thermionic emission of the trapped injected carriers from the QD bound state. This essentially attributes to the reduction of dark current. The dark current at near room temperature (~250K) under -2V applied bias is recorded to decrease by ten times from $5x10^{-4}$ A to $6x10^{-5}$ A as the coverage is increased from 0.4 ML for 0.8 ML. This has helped to significantly improve the detector's high-temperature performance and pushed up the operating temperature for potential photodetection up to 250K with measured detectivity as high as ~$8x10^{11}$ $cmHz^{1/2}W^{-1}$. The peak specific detectivity increases by twenty-eight times from 1.5 $x10^{11}$ to 42 $x10^{11}$ as the coverage is increased from 0.4 ML to 0.8 ML. Notably, two orders of magnitude lower dark current have been recorded for SML-QDs, as compared to the measured dark current of ~10^{-4} A for reference SK-QD sample under the condition of V_B = -2 V and T=250 K. This is a consequence of stronger confinement induced dark carrier trapping with a greater number of QD trap centres as compared to SK-QD based photodetector.

From a device performance standpoint, in spite of inherent tradeoff, we have shown the feasibility of tuning both the detector response speed and detectivity to significantly higher values by controlling InAs sub-monolayer coverage. This is attributed to the two-fold effect of laterally coupled SML QDs offering enhanced quantum dot carrier trapping leading to reduced dark current and increased photocurrent promoted by tunnel assisted faster free carrier transport.

8.2 Possible extension of this work and future outlook

Some possible extension and future aspects of the thesis work are as follows

8.2.1 Study photo-carrier dynamics in coupled QD system under transverse E-field

We have studied photocarrier dynamics and the consequences on TDPL and electro-transport properties of InAs/GaAs SML-QDs as a function of InAs sub-monolayer coverage without the presence of any transverse electric field. This work can be generalized to theoretical modelling of investigating photo-carrier relaxation dynamics in SML-QDs and other assemblies of strongly coupled nanostructures in the presence of a transverse electric field. Presently, I am working on developing a theoretical model to explicitly study field-dependent optoelectronic properties under strong carrier localization.

8.2.2 Enhanced carrier lifetime by introducing SML-QD superlattice minibands in IBSC

In my thesis, we have worked towards controlling the relative rate of tunneling to carrier recombination to tune light emission and photodetector response properties by varying SML coverage. The same methodology can be exploited to tune the product of open-circuit voltage (V_{oc}) and short circuit current (I_{sc}) in SML-QD based intermediate bandgap solar cell (IBSC). Strongly coupled SML QD superlattice can serve the role of a highly efficient intermediate

miniband in intermediate bandgap solar cell (IBSC). The spatial separation of electron-hole pair due to the internal electric field in solar cells enhances the carrier lifetime which is the key to improve the inter-subband transition strength and consequently to increase the two-step photocurrent (I_{sc}). But this has an inherent trade-off with V_{oc} which decreases with enhanced carrier lifetime. SML-QD can come handy in this situation which provides extended carrier recombination lifetime due to stronger quantum confinement, as well as promotes tunnel induced photo-carrier transport that can compensate V_{oc} and thus maintains high power efficiency.

8.2.3 Mid-infrared photonics in SML-QD quantum cascade and (DWELL) structure

InAs/GaAs SML-QDs can be integrated into the quantum cascade and a dot-in-well (DWELL) structure which can serve as a novel active material for mid-infrared photodetector. These devices enjoy the advantage of zero-bias operation, lower dark current, high operating temperature and small power dissipation which has attracted immense interest for possible applications in “lab on a chip” technologies for chemical sensing and free-space communication. Now, for better performance of such devices, the strength of inter-subband transition needs to be high which may be feasible by trapping the carriers for long by inducing some trap states. In that sense, the recombination dynamics and carrier lifetime measurements can be a good probe where my expertise on theoretical modelling of photo-carrier dynamics may be suitable.

8.2.4 Controlling photo-carrier relaxation dynamics in 2-D material

The idea of tuning relative lifetime of carrier recombination to tunneling in electronically coupled self-assembly of QDs can be employed to describe the photocarrier dynamics in advanced two-dimensional optoelectronic materials, like graphene and newly introduced

transition metal dichalcogenides (TMDs), like MoS_2 and WSe_2. By systematically following the relative strength of excitonic recombination and carrier escape, it may possible to tune the EQE, the stability and quality of the corresponding photo conversion devices through variation of feasible physical parameters.

8.2.5 Type-II SML-QD structure for photovoltaic application

There is an increasing interest in type-II structures like colloidal ZnTe/ZnSe QDs, due to their unique tuneable optoelectronic properties with band alignment with large band offset and improved quantum confinement effects. Recently, a slightly modified system made out of type-II ZnCdTe/ZnCdSe sub-monolayer QDs has emerged as one of the best candidates for efficient intermediate band solar cells due to its high carrier lifetime. I have a future interest in solar cell design by employing the strain compensated SML-QDs and analyze the combined photo-transport and gain dynamics which is still very much open to being explored. From theoretical interest, the investigation of the Aharanov–Bohm effect can be feasible by controlling the degree of carrier localization inside the QDs.

Suman_Mukherjee_PHYS05201404008

By Suman Mukherjee

WORD COUNT	49169	TIME SUBMITTED	25-FEB-2020 11:13AM
		PAPER ID	55862401

Growth and characterization of semiconductor quantum dots for optoelectronic device applications

By

SUMAN MUKHERJEE

Enrolment No- PHYS05201404008

Saha Institute of Nuclear Physics, Kolkata

A thesis submitted to the

Board of Studies in Physical Sciences

In partial fulfilment of requirements

for the Degree of

DOCTOR OF PHILOSOPHY

of

HOMI BHABHA NATIONAL INSTITUTE

February, 2020

Suman_Mukherjee_PHYS05201404008

ORIGINALITY REPORT

6%

SIMILARITY INDEX

PRIMARY SOURCES

1	aip.scitation.org Internet	289 words — 1%
2	www.imsc.res.in Internet	287 words — 1%
3	ir.semi.ac.cn Internet	108 words — < 1%
4	www.physik.tu-berlin.de Internet	98 words — < 1%
5	discovery.ucl.ac.uk Internet	95 words — < 1%
6	link.springer.com Internet	86 words — < 1%
7	www.nature.com Internet	76 words — < 1%
8	authors.aip.org Internet	68 words — < 1%
9	depositonce.tu-berlin.de Internet	63 words — < 1%
10	www.osapublishing.org Internet	60 words — < 1%
11	arxiv.org Internet	59 words — < 1%

12	www.solid.ipb.ac.rs Internet	57 words — < 1%
13	b-ok.cc Internet	52 words — < 1%
14	ir.nctu.edu.tw Internet	51 words — < 1%
15	eprints.ucm.es Internet	46 words — < 1%
16	dspace.rri.res.in Internet	45 words — < 1%
17	jpsj.ipap.jp Internet	45 words — < 1%
18	epdf.tips Internet	45 words — < 1%
19	aoip.osa.org Internet	37 words — < 1%
20	www.docstoc.com Internet	36 words — < 1%
21	etd.lib.metu.edu.tr Internet	36 words — < 1%
22	topics.aip.org Internet	36 words — < 1%
23	journals.tubitak.gov.tr Internet	32 words — < 1%
24	www.jove.com Internet	31 words — < 1%
25	hdl.handle.net Internet	30 words — < 1%

26	content.aip.org Internet	30 words — < 1%
27	comp.uark.edu Internet	30 words — < 1%
28	journals.ioffe.ru Internet	29 words — < 1%
29	archive.org Internet	29 words — < 1%
30	nparc.cisti-icist.nrc-cnrc.gc.ca Internet	28 words — < 1%
31	liu.diva-portal.org Internet	28 words — < 1%
32	www.ejournal.unam.mx Internet	28 words — < 1%
33	matprop.ru Internet	26 words — < 1%
34	www.boisestate.edu Internet	25 words — < 1%
35	pubs.rsc.org Internet	25 words — < 1%
36	www.openreadings.eu Internet	24 words — < 1%
37	pubman.mpdl.mpg.de Internet	21 words — < 1%
38	eprints.whiterose.ac.uk Internet	21 words — < 1%
39	newton.phy-astr.gsu.edu Internet	21 words — < 1%

40	epub.uni-regensburg.de Internet	20 words — < 1%
41	eprints.lib.hokudai.ac.jp Internet	19 words — < 1%
42	www.scribd.com Internet	19 words — < 1%
43	www.woe13.lamia.infm.it Internet	19 words — < 1%
44	spotidoc.com Internet	19 words — < 1%
45	trepo.tuni.fi Internet	19 words — < 1%
46	www3.uji.es Internet	19 words — < 1%
47	dragon.chemie.uni-hamburg.de Internet	19 words — < 1%
48	www.cise.columbia.edu Internet	18 words — < 1%
49	ge2004.polito.it Internet	18 words — < 1%
50	www.mdpi.com Internet	17 words — < 1%
51	www.imem.cnr.it Internet	17 words — < 1%
52	fisica.unipv.it Internet	17 words — < 1%
53	www.dtic.mil Internet	

		17 words — < 1%
54	wrap.warwick.ac.uk Internet	17 words — < 1%
55	jjap.ipap.jp Internet	17 words — < 1%
56	www.itc.nl Internet	17 words — < 1%
57	scholarworks.gsu.edu Internet	16 words — < 1%
58	ir.library.osaka-u.ac.jp Internet	16 words — < 1%
59	emas-web.net Internet	16 words — < 1%
60	pdfs.semanticscholar.org Internet	16 words — < 1%
61	proxy.osapublishing.org Internet	16 words — < 1%
62	repository.ntu.edu.sg Internet	16 words — < 1%
63	www.mseg.udel.edu Internet	15 words — < 1%
64	prr.hec.gov.pk Internet	15 words — < 1%
65	etheses.whiterose.ac.uk Internet	15 words — < 1%
66	www.iupac.org Internet	15 words — < 1%

67	d-nb.info Internet	15 words — < 1%
68	osaptesting.osa.org Internet	14 words — < 1%
69	portal.research.lu.se Internet	14 words — < 1%
70	ddd.uab.cat Internet	14 words — < 1%
71	www.intechopen.com Internet	14 words — < 1%
72	orbit.dtu.dk Internet	14 words — < 1%
73	www.ideals.illinois.edu Internet	14 words — < 1%
74	mrs.org Internet	14 words — < 1%

EXCLUDE QUOTES	ON	EXCLUDE MATCHES	OFF
EXCLUDE BIBLIOGRAPHY	ON		

Thesis Highlight

Name of the Student: Suman Mukherjee

Name of the CI: Saha Institute of Nuclear Physics

Enrolment No.: PHYS05201404008 of August 1, 2014

Thesis Title: Growth and characterization of semiconductor nanostructures for optoelectronic device applications

Discipline: Physical Sciences. Sub-Area of Discipline: Semiconductor Material Science

Date of viva voce: 14th July, 2020

The light emission and charge transport performance of 0-D quantum dot (QD)-based optoelectronic devices depends on the rate of decay of free photoexcited carrier population and the timescales of their recombination and transport. Apparently tuning of the temperature dependent light emission and field-induced photoconduction seems possible by controlling the above carrier lifetimes through variation of carrier localization throughout the coupled QD-assembly. There is a provision of achieving this by varying QD size and their intermediate separation respectively through variation of QD layer coverage (average layer thickness), keeping it below one complete monolayer (sub-monolayer). We have investigated the photo-carrier relaxation dynamics through the combined study of structural and temperature-dependent optical properties of MBE-grown GaAs-hosted self-assembled InAs/GaAs sub-monolayer (SML) QD heterostructure as a function of SML coverage. The related photogeneration and their transport have been studied through their IR photodetector optoelectronic characterization.

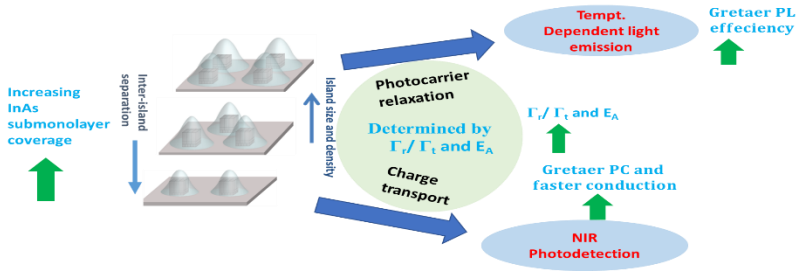

Figure 1 *Temperature dependent PL and transport study of carrier relaxation in self-assembled InAs/GaAs sub-monolayer quantum dot as a function of InAs fractional monolayer coverage.*

We have demonstrated the feasibility of spectrally tuning the sharp and intense excitonic PL in the near-IR region (~1.4-1.5 eV) by controlling InAs SML coverage (0.8-0.4 ML) as a consequence of strain-controlled quantum size (QD height~2.3-1.4 nm) effect. It has been observed that the simulation extracted thermal activation energy (E_A) and the relative rate of mutually competing excitonic recombination and inter-dot tunnelling (Γ_r/Γ_t) essentially hold the key to determine the shape of the temperature-dependent photoluminescence (PL), quantum efficiency and photocurrent (PC) spectra as a function of InAs SML coverage. The carrier lifetimes have been tuned through controlling the exciton binding energy and spatial de-localization of dissociated photocarriers achieved by varying QD size and morphology through variation of submonolayer coverage. The optical and photocarrier relaxation properties have been correlated to the size and morphology of the in-plane QD distribution. The progressively increasing value of Γ_r/Γ_t with increasing coverage indicates faster photocarrier transport by inter-dot tunnelling before they could recombine which offers substantial high temperature (~285 K) PLQY. Simultaneous tuning of temperature-dependent external quantum efficiency, response speed and trap hindered dark current performance have been possible by controlling InAs SML coverage (varying E_A and Γ_r/Γ_t).